Operational witnesses of non-classicality via Bell inequalities and contextuality

by

Sanchit Srivastava

A thesis
presented to the University of Waterloo
in fulfillment of the
thesis requirement for the degree of
Doctor of Philosophy
in
Physics (Quantum Information)

Waterloo, Ontario, Canada, 2026

© Sanchit Srivastava 2026

Examining Committee Membership

The following served on the Examining Committee for this thesis. The decision of the Examining Committee is by majority vote.

External Examiner:	Nicole Yunger Halpern Professor, Dept. of Physics, University of Maryland
Supervisor(s):	Shohini Ghose Professor, Dept. of Physics & Computer Sci., Wilfrid Laurier University Robert Mann Professor Emeritus, Dept. of Physics, University of Waterloo
Internal Member:	Alan Jamison Assistant Professor, Dept. of Physics, University of Waterloo
Internal-External Member:	Eduardo Martin-Martinez Professor, Dept. of Applied Math, University of Waterloo
Other Member(s):	Lucien Hardy Professor, Dept. Physics, University of Waterloo

Author's Declaration

This thesis consists of material all of which I authored or co-authored: see Statement of Contributions included in this thesis. This is a true copy of the thesis, including any required final revisions, as accepted by my examiners.

I understand that my thesis may be made electronically available to the public.

Statement of Contributions

This thesis is primarily based on the following articles and preprints.

1. Sanchit Srivastava and Shohini Ghose, "Multipartite entanglement versus nonlocality for two families of N-qubit states," Physical Review Research **7**, 033289 (2025).

2. Sanchit Srivastava and Shohini Ghose, "Contextuality and Chaos," arXiv:2503.13886 (2025).

3. Caroline Lima, María Rosa Preciado-Rivas, and Sanchit Srivastava, "Contextuality from quantum field vacua using qutrit Unruh–DeWitt detectors," Physical Review D **113**, 065025 (2026).

Chapter 3 is based on [1]. Sanchit Srivastava led the research and drafted the majority of the manuscript under the supervision of Prof. Shohini Ghose.

Chapter 4 is based on [2]. Sanchit Srivastava led the research and drafted the manuscript under the supervision of Prof. Shohini Ghose.

Chapter 5 is based on [3]. Sanchit Srivastava contributed equally with Caroline Lima and María Rosa Preciado-Rivas to the research and drafting of the manuscript. In particular, Sanchit's contributions were in the theoretical parts concerning contextuality and Wigner negativity, and developing the numerical simulations. The manuscript was drafted with equal contributions from the co-authors.

Chapter 6 is based on an ongoing project with collaborators Amolak Kalra, Selman Ipek, Cihan Okay and Shohini Ghose. The project was led primarily by Sanchit Srivastava. The parts included in the thesis were developed in majority by Sanchit, with minor technical contributions from Amolak Kalra. Selman Ipek and Cihan Okay initiated the project, Prof. Shohini Ghose has played a supervisory role in the development of the results.

Abstract

This thesis investigates operational signatures of non-classicality in quantum systems, examining the relationship between Bell inequalities, contextuality tests, and discrete Wigner negativity across four case studies. The first analyzes multipartite entanglement and genuine multipartite nonlocality in multiqubit systems, deriving analytical expressions for Svetlichny inequality violations for generalized Greenberger–Horne–Zeilinger (GHZ) and maximal-slice states; the results indicate that the entanglement–nonlocality relationship depends on state structure rather than scalar entanglement measures alone. The second uses an optimized Bell inequality as a contextuality witness for the spin-1 quantum kicked top, revealing correlations between violation strength and the regular-versus-chaotic structure of the classical phase space. The third examines two qutrit Unruh–DeWitt detectors coupled to the Minkowski vacuum, showing that an initially noncontextual product state can develop contextual correlations through vacuum-mediated interactions, with contextuality onset coinciding with discrete Wigner negativity. The fourth constructs logical Bell inequalities for odd prime dimensions that connect single-qudit Wigner negativity to inequality violation. Each of these tests constrains a different class of classical model: locally causal hidden variables, noncontextual hidden variables, or positive Wigner representations. A recurring theme is that a violation of such an inequality certifies a property of the observed measurement statistics, rather than directly quantifying an underlying quantum resource.

Acknowledgements

I am deeply grateful to my supervisors, Prof. Shohini Ghose and Prof. Robert Mann, for their guidance and unwavering support throughout this journey. I would especially like to thank Prof. Ghose for keeping me focused and motivated towards a goal while allowing me to explore various topics. I would also like to thank the members of my advising committee, Prof. Alan Jamison and Prof. Eduardo Martin-Martinez, whose feedback and advice helped direct the progress of my research.

I would like to thank my collaborators: Caroline Lima, María Rosa Preciado-Rivas, Amolak Kalra, Selman Ipek, and Cihan Okay, for the stimulating discussions that shaped much of this work.

I am grateful to the administrative staff at the Department of Physics and at the Institute for Quantum Computing for their assistance in navigating the practical aspects of graduate life.

To my colleagues who guided me along the way— Jack, Erickson, Amit, Shlok, Arsalan, Pulkit, Avantika, Forouzan, Everett, Sayan, Dinesh—thank you for the countless discussions, advice, and encouragement. These have been some of the most important takeaways from this PhD.

To my friends here at Waterloo— Amit, Yash, Kishore, Devashish, Khushmeet, Sonell, Sourabh, Faisal, Punit, (and many more), thank you for the laughter, the late nights, and the companionship that made this city feel like home. To my friends not here at Waterloo, thank you for your continued support, friendship and encouragement despite the distance. You were the ones I turned to when the going got tough. My intramural soccer team provided a welcome escape and reminded me that there is life beyond research. I am grateful to the Maths Graduate soccer team for adopting me as one of their own.

I owe an immeasurable debt to my family for their love and support over all these years. Ma, Papa, Di, and everyone else, thank you for all the encouragement and the comfort when I needed it.

Finally, to Ren: none of this would have been possible without you, and I will never be able to fully express how much your love and support means to me. Thank you for everything.

Dedication

This thesis is dedicated to my parents.

Table of Contents

Examining Committee Membership ii

Author's Declaration iii

Statement of Contributions iv

Abstract v

Acknowledgements vi

Dedication vii

List of Figures xiii

List of Tables xv

1 Introduction 1

2 Background 5

2.1 Correlations and Bell nonlocality 5

2.1.1 Bell inequalities 6

2.1.2 Genuine multipartite nonlocality and hybrid-local models 7

2.1.3 Multipartite entanglement and the n-tangle 8

2.2 Compatible Measurements and Inequality Tests . . . 9
2.2.1 The Kochen–Specker theorem and contextuality . . . 9
2.2.2 Measurement scenarios, contexts, and empirical models . . . 10
2.2.3 The KCBS inequality . . . 11
2.3 Contextual Fraction . . . 13
2.3.1 Computation via linear programming . . . 14
2.4 Discrete Wigner . . . 15
2.4.1 Quasiprobabilities and the meaning of negativity . . . 15
2.4.2 Gross discrete Wigner function (odd dimension) . . . 16

3 Multipartite Entanglement versus Genuine Multipartite Nonlocality 19
3.1 State Families and Parametrization . . . 21
3.1.1 Generalized GHZ (GGHZ) states . . . 21
3.1.2 Maximal slice states . . . 21
3.2 Svetlichny Inequality for N-Qubit Systems . . . 22
3.3 Main Results . . . 23
3.3.1 Maximum Svetlichny values for arbitrary N . . . 24
3.3.2 GGHZ states . . . 25
3.3.3 Maximal slice states . . . 26
3.3.4 Comparative summary . . . 27
3.4 Discussion . . . 27

4 Non-Classicality as a Dynamical Signature of Chaos: The Quantum Kicked Top 29
4.1 The Kicked Top Model . . . 30
4.1.1 Hamiltonian, Floquet step, and classical limit . . . 30
4.2 The KCBS Inequality as a Contextuality Witness . . . 32
4.2.1 KCBS inequality for spin-1 systems . . . 32

4.3 Numerical Results: Global and Local Contextuality Signatures 33
4.3.1 Global signature: KCBS-violation fraction versus κ 33
4.3.2 Local signature: phase-space-resolved contextuality 33
4.4 Discussion: Interpretation and Limitations 39

5 Contextuality from the Quantum Vacuum **42**
5.1 Physical Setup 43
5.1.1 Qutrit detectors 44
5.1.2 Detector-field interaction 45
5.2 Contextuality and Wigner-Negativity Diagnostics 48
5.2.1 Two-qutrit Heisenberg–Weyl measurement scenario 48
5.3 Results: Contextuality Induced by Vacuum Interactions 50
5.3.1 Energy-gap dependence 51
5.3.2 Switching-duration dependence 58
5.3.3 Scaling with coupling strength 58
5.4 Discussion: Mechanism and Parameter Dependence 58

6 Logical Bell Inequalities for Witnessing Marginal Wigner Negativity **63**
6.1 Introduction and Motivation 63
6.2 Heisenberg–Weyl Group 64
6.3 Measurement Contexts for Two Qudits 66
6.3.1 Single-Qudit Measurement Settings M 67
6.4 Logical Bell Inequalities and the Marginal Witness 68
6.4.1 Framework and Construction 68
6.4.2 The Marginal Witness 69
6.4.3 Main Theorem 70
6.5 Proof of the Main Result 71
6.5.1 Step 1: Constructing Logical Formulae for Contexts 71

6.5.2 Step 2: Characterizing Global Value Assignments 73
6.5.3 Step 3: Proving Joint Unsatisfiability 74
6.5.4 Step 4: Deriving the Inequality and Identifying the Witness 75
6.6 Quantitative Bound: Contextual Fraction 77
6.7 Generalizations 78
6.7.1 Witnessing Single-Qudit Wigner Negativity with n Qudits 78
6.7.2 Witnessing k-Qudit Marginal Wigner Negativity 80
6.8 Discussion 81

7 Conclusion and Outlook **83**

References **86**

APPENDICES **98**

A Supplementary Material: Derivations for Chapter 3 **99**
A.1 Derivation for GGHZ states 99
A.1.1 Bloch parametrization and the F/G decomposition 100
A.1.2 Maximizing the "classical" branch $|F_N^{\pm}|$ 101
A.1.3 Maximizing the "GHZ interference" branch $|G_N^{\pm}|$ 102
A.1.4 Global maximum over all measurements for general α 102
A.2 Derivation for maximal slice states 106
A.2.1 Rewriting $S_N^{\pm}$ by isolating the last two parties 106
A.2.2 Orthogonal directions for party $N-1$ 106
A.2.3 Reducing to a sum of square roots 106
A.2.4 Bounding the correlators on the maximal slice state 107
A.2.5 Phase choices, saturation, and the final maximum 108

B Supplementary Material for Chapter 5 **109**

B.1 Heisenberg–Weyl internal dynamics 109

B.1.1 Additional local coherence integral 109

B.1.2 Two-detector state for HW dynamics 110

B.1.3 Reduced single-detector state for HW dynamics 110

B.1.4 Wigner-negativity conditions 110

B.2 Closed-form integrals for the detector state 111

C Supplementary Material for Chapter 6 **112**

C.1 Two-Qudit Contexts: Explicit Enumeration (Optional) 112

C.1.1 Separable (product) contexts 113

C.1.2 Entangled contexts 113

C.1.3 Total number of maximal contexts 113

C.2 Coordinate Form of the Inconsistency Argument 114

List of Figures

2.1 KCBS exclusivity graph: vertices are projectors and edges connect orthogonal (hence mutually exclusive) pairs. Any deterministic noncontextual assignment may label a vertex with 1 only if its neighbours are labelled 0. The highlighted vertices show a largest allowed choice (two non-adjacent 1's), which yields the noncontextual bound $\sum_i \langle \Pi_i \rangle \leq 2$. 13

4.1 Global contextuality signature for the kicked top. For each κ, we sample 1000 Haar-uniform initial coherent states and evolve each for $T = 100$ Floquet steps. The plotted quantity is the fraction of initial conditions exhibiting at least one KCBS violation during evolution. Two localized dips near $\kappa \approx 2$ and $\kappa \approx \pi$ coincide with classical bifurcations where a fixed point and a period-4 orbit lose stability [75]. 34

4.2 Classical–quantum phase-space comparison at $\kappa = 0.1$ 36

4.3 Classical–quantum phase-space comparison at $\kappa = 2.5$ 37

4.4 Classical–quantum phase-space comparison at $\kappa = 0.1$ (mean-based) 38

4.5 Classical–quantum phase-space comparison at $\kappa = 2.5$ (mean-based) 38

5.1 Contextual fraction normalized by λ^2 for large detectors ($R/T = 1$) as a function of ΩT. Different curves correspond to different detector separations satisfying the spacelike criterion. 52

5.2 Contextual fraction normalized by λ^2 for small detectors ($R/T = 0.1$) approaching the pointlike limit. 53

5.3 Wigner negativity (sum-negativity) normalized by λ^2 for large detectors ($R/T = 1$). 54

5.4 Wigner negativity (sum-negativity) normalized by λ^2 for small detectors ($R/T = 0.1$). 55

5.5 Contextual fraction normalized by λ^2 for small detectors ($R/T = 0.1$) as a function of ΩT obtained by varying the switching duration T (with other parameters fixed as in the corresponding numerical setup). 56

5.6 Wigner sum-negativity normalized by λ^2 for the reduced single-detector state for the same small-detector switching-variation setup as Figure 5.5. . 57

5.7 Comparison of Wigner sum-negativity (normalized by λ^2) produced by SU(2) and Heisenberg–Weyl internal detector dynamics, illustrating the enhanced coherence generation in the HW model. 61

List of Tables

3.1 Comparison of GGHZ and maximal slice families: entanglement versus non-locality 27

"All we have to decide is what to do with the time that is given us."

— Gandalf, in J.R.R. Tolkien's *The Fellowship of the Ring*

Chapter 1

Introduction

What makes quantum mechanics fundamentally different from classical physics? The distinction between quantum and classical mechanics is a foundational problem in physics. Historically, this boundary has been explored through interpretational debates concerning measurement, collapse, and nonlocality, beginning with the EPR paradox [47] and thought experiments such as Schrödinger's cat [111]. Complementing these conceptual investigations is an operational inquiry: given a specific preparation-and-measurement scenario and observed statistics, can the data be reproduced by a defined class of "classical" models [125, 110, 138]? This perspective, grounded in the no-go theorems of Bell [22, 21, 38] and Kochen–Specker [73], is central to quantum information science, providing the basis for certification tasks and establishing boundaries for efficient classical simulation [92, 87].

The term "non-classicality" does not refer to a single, monolithic property. Different experimental scenarios impose different constraints on what a classical model may assume, and a state may exhibit one form of non-classicality without exhibiting another. Bell scenarios test whether correlations between spacelike-separated measurements can arise from locally causal hidden variables; Bell nonlocality requires entanglement, but entangled states need not always violate Bell inequalities [127]. Contextuality tests ask whether outcomes of compatible measurements on a single system can be assigned values independent of the measurement context; here the notion of spatial separation is not a necessary condition. Phase-space representations ask whether a state admits a description as a probability distribution over phase space; Wigner-function negativity [128, 130] indicates that it cannot. Since both contextuality and Wigner negativity signal failure of classical probabilistic descriptions, one might expect them to coincide, but they need not: a state can be Wigner-negative yet satisfy all contextuality inequalities for a given set of measurements [115]. In odd prime dimensions, however, a precise equivalence holds: contextuality with respect

to Heisenberg–Weyl measurements (the generalization of Pauli measurements to higher-dimensional systems) is equivalent to negativity of the discrete Wigner function [67, 42]. This connection, which plays a central role in Chapters 5 and 6, also underlies efficient classical simulation: when all states remain Wigner-nonnegative, stabilizer-like subtheories admit efficient simulation [59, 122, 123].

Non-classicality also depends on the available measurements. Some states exhibit interference yet remain easy to simulate if operations are restricted to specific subtheories, like stabilizer or Gaussian mechanics [57, 1, 85]. Conversely, systems that appear classical under coarse-grained observation can reveal non-classical features when probed with finer witnesses [74, 114, 60].

The investigations presented in Chapters 3–6 explore distinct domains—multipartite nonlocality, dynamical signatures of chaos, detector–field interactions, and phase-space representations—using this perspective. The objective is not to propose a universal measure of "quantumness," but to compare what distinct witnesses certify against specific classical models: locally causal hidden-variable models, noncontextual hidden-variable models, and positive discrete Wigner representations. A recurring theme is that operational witnesses make claims about observed data, not directly about underlying states. Violating a Bell inequality certifies that no locally causal model can reproduce the correlations, but does not directly certify how much entanglement is present; the relationship between witness violations and resource measures is often nonlinear or family-dependent. Part of this thesis is devoted to understanding such relationships in specific scenarios.

Chapter 3 examines the relationship between multipartite entanglement, quantified by the n-tangle [129], a measure that generalizes the squared concurrence to N-qubit systems, and genuine multipartite nonlocality witnessed by optimized Svetlichny-type inequalities [117], which exclude hybrid models in which a strict subset of parties shares nonlocal resources. Entanglement and nonlocality are not the same resource: Werner showed that some entangled states admit local hidden-variable models [127], and the multipartite setting introduces further subtleties. A state may be nonlocal across some bipartition without exhibiting irreducibly N-party correlations; genuine multipartite nonlocality (GMN) requires ruling out all such "hybrid" explanations in which a subset of parties shares nonlocal resources while remaining locally correlated with the rest [118, 15]. The question addressed in this chapter is whether, and how, the entanglement content of a state determines its capacity to exhibit GMN. In some families, GMN is "activated" only above a finite entanglement threshold; in others, any nonzero entanglement suffices. We derive analytical expressions for the maximal violation of the Svetlichny inequality for two families of states for arbitrary number of qubits N. For the generalized GHZ family (with even $N > 2$), a violation requires the n-tangle to exceed $1/2$ regardless of N, with the optimized violation

exhibiting non-monotonic behavior. The maximal-slice family, a one-parameter subset of symmetric states that interpolates between the W state and the GHZ state, behaves differently: any non-zero n-tangle is sufficient for violation, which increases monotonically. These results illustrate that the relationship between entanglement and nonlocality depends sensitively on the structure of the state, not just on a scalar entanglement measure, and shed light on the qualitatively different nonlocal nature of these multiqubit states.

Chapter 4 investigates the spin-1 quantum kicked top [62, 36, 61] utilizing an optimized Bell inequality violation as a state-dependent contextuality witness. Quantum chaos presents a conceptual challenge: the trajectory-based definition of classical chaos, in which nearby initial conditions diverge exponentially in phase space, does not translate directly to quantum mechanics. Unitary evolution preserves state overlaps, and the Heisenberg uncertainty principle prevents arbitrary localization in phase space. Characterizing "quantum chaos" therefore requires indirect diagnostics that correlate with the regular-versus-chaotic structure of the classical phase portrait. Established examples include random-matrix spectral statistics [25] and out-of-time-ordered correlators [79, 84]. Here we ask whether contextuality can serve as a complementary diagnostic: although contextuality is defined by the measurement statistics of a state rather than by a dynamical quantity, evolving an initially non-contextual state under a chaotic Hamiltonian can generate contextuality, and the degree to which it does so may reflect the underlying classical phase-space structure. The kicked top is well suited to this question: by tuning a single parameter (the kick strength κ), the classical dynamics transitions from regular motion organized around fixed points to a "chaotic sea" where trajectories explore the phase space erratically. In the quantum model, spin-coherent states provide the natural semiclassical probes, and the chosen Bell inequality offers a state-dependent contextuality test native to spin-1 systems. Numerical analysis reveals correlations between these violations and the classical mixed phase space structure, showing regular and chaotic regions, as the kick strength κ varies, utilizing a heuristic statistic to mitigate periodic orbit artifacts.

Chapter 5 analyzes two qutrit Unruh–DeWitt detectors coupled to a massless scalar field in the Minkowski vacuum [120, 44, 121, 105, 102, 82]. The quantum vacuum, though it contains no particles, is not featureless: correlation functions encode nontrivial structure across spacetime. This structure can be accessed operationally by coupling localized "detector" systems to the field for a finite time. Entanglement harvesting is a well-known example: two detectors that never interact directly can become entangled solely through their local couplings to the vacuum [105, 102]. This chapter extends the harvesting perspective to contextuality. An Unruh–DeWitt detector is a localized quantum system (here, a qutrit) that couples to the field amplitude along its worldline. Starting from a product state of two such detectors, we ask whether vacuum-mediated interactions can induce con-

textual correlations in the joint detector state. The contextual fraction [3], which quantifies the minimum fraction of the observed measurement statistics that cannot be reproduced by any noncontextual hidden-variable model, serves as the quantitative diagnostic, evaluated in the Heisenberg–Weyl measurement scenario. The analysis demonstrates that the reduced two-detector state, initially a noncontextual product, can develop a non-zero contextual fraction post-interaction. The onset of contextuality coincides with the emergence of discrete Wigner negativity in the local detector states.

Chapter 6 examines the relationship between contextuality and Wigner negativity in odd prime dimensions. Contextuality is tested through inequalities that constrain measurement statistics; Wigner negativity is read off from a phase-space representation. For systems of two or more qudits, these two notions are known to coincide: contextuality with respect to generalized Pauli measurements occurs exactly when the discrete Wigner function is negative somewhere [67, 42]. The single-qudit case is more subtle. A single qudit can have a negative Wigner function, yet its measurements alone do not provide enough structure for a contextuality test. We construct a family of logical Bell inequalities [5] that bridge this gap. A second qudit is introduced as an auxiliary system to supply the necessary measurement structure, but the resulting inequality depends only on single-qudit statistics. The main result is an exact equivalence: the inequality is violated if and only if the Wigner function of the single-qudit marginal is negative at the corresponding phase-space point. This provides a direct operational link between two distinct notions of non-classicality.

The remainder of the thesis is organized as follows. Chapter 2 introduces the technical background and fixes notation for Bell and contextuality scenarios, the contextual fraction, and discrete Wigner representations. Chapters 3–6 present the four case studies described above. Chapter 7 synthesizes the results and discusses limitations and open directions. Appendices collect derivations and supplementary material.

Chapter 2

Background

The chapters that follow use a common set of operational definitions and mathematical tools. These include models for correlations in multipartite experiments, compatibility constraints for single-system tests, and phase-space representations of finite-dimensional quantum states. This chapter collects the required definitions and conventions. Our aim is to fix notation and introduce the witnesses and quantifiers used throughout the thesis.

The chapter is organized around three ingredients.

- **Multipartite correlation models** (Section 2.1): Bell scenarios, local and hybrid-local decompositions, and the inequality formalisms used to witness nonlocality.
- **Compatibility and contextuality** (Section 2.2): Measurement scenarios and compatibility, together with inequality tests used as a contextuality witnesses.
- **Phase-space quasiprobabilities** (Section 2.4): Discrete Wigner representations in odd dimension and the role of negativity as an obstruction to a classical probabilistic model.

2.1 Correlations and Bell nonlocality

Bell's theorem [22] shows that quantum theory predicts correlations that cannot be reproduced by any local hidden-variable model. A Bell scenario involves two or more spatially separated parties, each capable of choosing among several measurement settings and obtaining one of several outcomes [29]. In the bipartite case, Alice chooses a measurement

setting x from a set $\mathcal{X}$ and obtains outcome a from a set $\mathcal{A}$; Bob independently chooses setting $y \in \mathcal{Y}$ and obtains outcome $b \in \mathcal{B}$. The experiment is characterized by the conditional probability distribution $p(a, b \mid x, y)$, describing the joint statistics of outcomes given the measurement choices.

The question at the heart of Bell's theorem is whether these correlations can be explained by a local hidden-variable (LHV) model. Such a model posits the existence of a hidden variable λ, distributed according to some probability distribution $p(\lambda)$, that determines the outcomes through local response functions. Formally, $p(a, b \mid x, y)$ admits an LHV decomposition if and only if

$$p(a, b \mid x, y) = \sum_{\lambda} p(\lambda)\, p(a \mid x, \lambda)\, p(b \mid y, \lambda), \tag{2.1}$$

where $p(a \mid x, \lambda)$ and $p(b \mid y, \lambda)$ are local response functions depending only on the local measurement choice and the shared hidden variable. The factorization in Eq. (2.1) captures the physical assumption of *locality*: once the hidden variable is specified, Alice's outcome depends only on her measurement choice, and likewise for Bob.

Correlations that admit such a decomposition are called *local* or *Bell-local*. The set of all local correlations forms a convex polytope, the *local polytope*, whose vertices correspond to deterministic local strategies. Correlations lying outside this polytope are *nonlocal* and cannot be explained by any LHV model.

2.1.1 Bell inequalities

Bell inequalities are linear constraints satisfied by all local correlations. Geometrically, they correspond to the facets of the local polytope: any correlation satisfying all Bell inequalities lies inside the polytope, while any violation certifies nonlocality [29].

A widely studied Bell inequality is the Clauser–Horne–Shimony–Holt (CHSH) inequality [38], which applies to the scenario with two parties where each party has two binary-outcome measurements. Let Alice's observables be A_0 and A_1, and Bob's be B_0 and B_1, each taking values ± 1. The CHSH inequality states

$$S := \langle A_0 B_0 \rangle + \langle A_0 B_1 \rangle + \langle A_1 B_0 \rangle - \langle A_1 B_1 \rangle \leq 2, \tag{2.2}$$

where $\langle A_x B_y \rangle = \sum_{a,b} a \cdot b \cdot p(a, b \mid x, y)$ denotes the correlation function. Any LHV model satisfies $|S| \leq 2$.

Quantum theory predicts settings (states and measurement choices) for which the CHSH expression satisfies $|S| > 2$, exceeding the LHV bound. For the maximally entangled two-qubit state $|\Phi^+\rangle = (|00\rangle + |11\rangle)/\sqrt{2}$ and appropriately chosen measurement directions, the CHSH value reaches $S = 2\sqrt{2} \approx 2.83$, the Tsirelson bound [37]. This violation demonstrates that quantum correlations are genuinely nonlocal in Bell's sense. A comprehensive review of Bell nonlocality, its operational consequences, and generalizations to more complex scenarios is given by Brunner *et al.* [29]. This thesis builds particularly on multipartite generalizations, discussed in the following subsections.

2.1.2 Genuine multipartite nonlocality and hybrid-local models

In multipartite scenarios, the notion of nonlocality requires refinement. A correlation can violate a Bell inequality while still admitting a hybrid explanation, in which some subset of parties shares nonlocal resources internally but remains locally correlated with the rest. Such correlations are nonlocal across at least one cut, but they do not certify that the nonlocality is irreducibly shared among *all* parties.

This motivates genuine N-party nonlocality: correlations that cannot be written as a convex mixture of models that are local with respect to some bipartition. Operationally, the corresponding witnesses are Bell inequalities whose classical bound is taken over all such bipartition-local (hybrid-local) models. The tripartite case admits a clean and widely used formulation. Svetlichny [118] introduced an inequality whose violation certifies that the nonlocality is irreducibly three-partite: no hybrid model in which the parties are split into two groups, with arbitrary shared nonlocal resources permitted within each group, can reproduce the observed correlations.

Concretely, a tripartite correlation $p(a, b, c \mid x, y, z)$ is *Svetlichny-local* (or admits a hybrid-local model) if it can be written as a convex mixture over bipartitions:

$$p(a, b, c \mid x, y, z) = \sum_{\kappa \in \{AB|C,\, AC|B,\, BC|A\}} q_\kappa \, p_\kappa(a, b, c \mid x, y, z), \tag{2.3}$$

where $q_\kappa \geq 0$ with $\sum_\kappa q_\kappa = 1$, and each p_κ factors according to the corresponding bipartition. For example, for the bipartition $AB|C$:

$$p_{AB|C}(a, b, c \mid x, y, z) = \sum_\lambda p(\lambda)\, p_{AB}(a, b \mid x, y, \lambda)\, p_C(c \mid z, \lambda), \tag{2.4}$$

where $p_{AB}(a, b \mid x, y, \lambda)$ can be an arbitrary (possibly nonlocal) bipartite correlation shared between Alice and Bob, but the correlation with Charlie factorizes. This formulation

imposes locality only across the bipartition; within the two-party group the conditional distribution p_{AB} may be taken as general (and in particular need not itself admit an LHV model). Generalizations to N parties exist [40], and we use *Svetlichny-type* as a generic label for Bell inequalities that rule out all such bipartition-local models.

2.1.3 Multipartite entanglement and the n-tangle

For a small number of qubits, a useful way to characterize multipartite entanglement measures is via the monogamy of bipartite entanglement. The *concurrence* $C(\rho)$, introduced by Wootters [131], is a measure of bipartite entanglement for two-qubit states that ranges from 0 (separable) to 1 (maximally entangled). For three qubits A, B, C, Coffman, Kundu, and Wootters introduced the *tangle* $\tau := C^2$ (the square of the concurrence) and showed that it obeys a trade-off relation [39]. For a pure state $|\psi\rangle_{ABC}$, let $\rho_A := \mathrm{Tr}_{BC}(|\psi\rangle\langle\psi|)$. The entanglement between A and the pair BC is quantified by

$$\tau_{A|BC} := 4 \det(\rho_A), \tag{2.5}$$

while the bipartite tangles τ_{AB} and τ_{AC} are the squared concurrences of the reduced two-qubit states, $\tau_{AB} := C(\rho_{AB})^2$ and $\tau_{AC} := C(\rho_{AC})^2$. The CKW monogamy inequality states that

$$\tau_{A|BC} \geq \tau_{AB} + \tau_{AC}. \tag{2.6}$$

The difference

$$\tau_{ABC} := \tau_{A|BC} - \tau_{AB} - \tau_{AC} \tag{2.7}$$

is nonnegative and (for pure states) independent of which qubit is singled out; it is called the residual entanglement or *3-tangle* and captures genuinely tripartite entanglement [39]. Wong and Christensen introduced the *n-tangle* as a natural generalization of this construction to systems of even n qubits [129]. For a pure state $|\psi\rangle$ of n qubits with n even, define the spin-flipped state

$$|\tilde{\psi}\rangle := \sigma_y^{\otimes n} |\psi^*\rangle, \tag{2.8}$$

where σ_y is the Pauli-Y matrix and $|\psi^*\rangle$ denotes the complex conjugate of $|\psi\rangle$ in the computational basis. The n-tangle is then defined as

$$\tau_n(\psi) := \left| \langle \psi \mid \tilde{\psi} \rangle \right|^2. \tag{2.9}$$

This quantity is invariant under local unitaries and vanishes for fully separable pure states. In the multipartite setting the notion of an "entanglement monotone" is more delicate than in the bipartite case; the n-tangle is often used as a convenient closed-form indicator of multipartite entanglement for even-n families.

2.2 Compatible Measurements and Inequality Tests

A second family of operational non-classicality tests concerns compatible measurements on a single system. Here the notion of classicality is noncontextuality: the assumption that outcomes are determined by underlying variables and do not depend on which other compatible measurements are jointly implemented.

2.2.1 The Kochen–Specker theorem and contextuality

The Kochen–Specker theorem [73] establishes that quantum mechanics is incompatible with noncontextual hidden-variable models; see also Bell's formulation and discussion in [21]. Unlike Bell's theorem, which concerns spacelike-separated measurements, the Kochen–Specker theorem concerns the impossibility of assigning predetermined, context-independent values to observables in a way that is consistent across overlapping contexts of compatible (e.g., commuting projective) measurements. A comprehensive modern review of Kochen–Specker contextuality, including its various formulations and applications, is given by Budroni *et al.* [31].

Kochen–Specker contextuality is easiest to state for sharp (projective) measurements. In this setting, a *context* is a set of mutually compatible projectors that can be measured together, often taken to be a complete projective measurement $\{\Pi_k\}$ with $\sum_k \Pi_k = \mathbb{I}$. If we imagine an underlying hidden state that predetermines the outcomes, then each projector is assigned a value $v(\Pi) \in \{0, 1\}$, constrained by the measurement relations within each context: in a complete projective measurement exactly one outcome occurs, so one demands $\sum_k v(\Pi_k) = 1$. Noncontextuality adds the key requirement that $v(\Pi)$ depends only on the projector Π itself, not on which other compatible projectors it is grouped with.

Theorem 2.1 (Kochen–Specker theorem [73, 21])**.** *For every Hilbert space dimension $d \geq 3$, there exist a finite set of projectors $\mathcal{P}$ on $\mathbb{C}^d$ and a family of contexts $\mathcal{C}$ (each $C \in \mathcal{C}$ is a set of mutually orthogonal projectors in $\mathcal{P}$ with $\sum_{\Pi \in C} \Pi = \mathbb{I}$) such that there is no function $v : \mathcal{P} \to \{0, 1\}$ satisfying*

$$\sum_{\Pi \in C} v(\Pi) = 1 \quad \textit{for all } C \in \mathcal{C}. \tag{2.10}$$

Equivalently, one cannot assign predetermined, context-independent outcomes to all projectors while respecting the quantum measurement constraints in every context.

Theorem 2.1 shows that in Hilbert spaces of dimension $d \geq 3$ there exist finite sets of projectors with overlapping contexts for which *no* such noncontextual value assignment is possible. Intuitively, the same projector can appear in multiple contexts, and the requirement that it carry a single, context-independent value can force mutually incompatible constraints when one tries to satisfy all contexts at once. The original construction used 117 rays in dimension 3 [73], and many smaller proofs are known; an accessible set of constructions is due to Peres [98]. One can demonstrate contextuality either in a state-dependent way (for particular prepared states) or in a state-independent way (for all states on a given Hilbert space) [31]. The Klyachko-Can-Binicioglu-Shumovsky (KCBS) inequality (Section 2.2.3) is the canonical state-dependent example. At the opposite extreme, Yu and Oh gave a state-independent proof for a qutrit using only 13 rays [135], and Cabello, Kleinmann, and Portillo proved that 13 is minimal for state-independent contextuality [32].

Ideal Kochen–Specker contradictions assume exact compatibility relations and exact outcome constraints within each context (e.g., exclusivity and completeness for projective measurements). In realistic experiments these conditions hold only approximately, so contextuality is typically tested via *noncontextuality inequalities*: noise-robust linear bounds on observable statistics satisfied by all noncontextual models but violated by quantum predictions. This perspective also supports operational notions of noncontextuality that do not assume deterministic value assignments a priori [114, 76].

2.2.2 Measurement scenarios, contexts, and empirical models

We adopt the language of *measurement scenarios* used in modern approaches to contextuality [4, 114]. The point of this formalism is to separate two kinds of information: which measurements are available, and which subsets of them are compatible (that is, can be jointly implemented). Concretely, a measurement scenario is a triple $(X, \mathcal{C}, O)$:

- X is a finite set of measurements (observables).
- $\mathcal{C}$ is a collection of subsets $C \subseteq X$ called *contexts*, where each context represents a set of measurements that can be performed together (e.g., mutually commuting projectors).
- O is the outcome set for each measurement (for example $\{0, 1\}$ for projectors, or $\{\pm 1\}$ for dichotomic observables).

An *empirical model* for such a scenario is then a family of probability distributions $\{p_C\}_{C \in \mathcal{C}}$, one for each context C. Each p_C is a joint distribution over the outcomes of

the measurements in C; operationally, it is the table of observed frequencies obtained by repeatedly implementing the compatible joint measurement specified by C. Since a given measurement can appear in more than one context, these context-by-context distributions are required to agree on overlaps. The standard consistency condition is *no-disturbance* (or *marginal compatibility*): for any two contexts $C, C' \in \mathcal{C}$, the marginals of p_C and $p_{C'}$ on $C \cap C'$ must coincide. In plain terms, if a measurement A can be jointly performed with B and also jointly performed with C, then the statistics of A alone should not depend on whether it was paired with B or with C.

Noncontextuality is the hypothesis that there exists an underlying description in which every measurement in X has a preassigned outcome, and this assigned outcome does not depend on which other compatible measurements happen to be implemented alongside it. Such a preassignment is a *global assignment*, i.e. a function $s : X \to O$. Writing O^X for the set of all global assignments and $s|_C$ for the restriction of s to a context C, an empirical model is *noncontextual* if it can be obtained by first sampling a global assignment s from a probability distribution μ over O^X, and then reporting the outcomes prescribed by s on the chosen context. Equivalently, there exists a distribution μ over O^X such that, for every context C and every joint outcome $o_C \in O^C$,

$$p_C(o_C) = \sum_{s \in O^X} \mu(s)\, \mathbf{1}[s|_C = o_C], \tag{2.11}$$

where $s|_C$ denotes the restriction of assignment s to the measurements in context C, and $\mathbf{1}[\cdot]$ is the indicator function. This is directly analogous to an LHV decomposition: the hidden variable is the global assignment s, and the observed joint outcome statistics are the corresponding marginals. The set of empirical models admitting such a decomposition is convex; its extreme points are the deterministic assignments $s : X \to O$, and their convex hull is the *noncontextual polytope*. Empirical models inside this polytope are noncontextual, while models outside it are contextual. Moreover, the facet-defining inequalities of the polytope are precisely the *noncontextuality inequalities* used as noise-robust witnesses in experiments and applications [4, 26].

2.2.3 The KCBS inequality

The Klyachko–Can–Binicioglu–Shumovsky (KCBS) inequality [72] is a paradigmatic example of a state-dependent noncontextuality inequality for a three-dimensional quantum system (qutrit or spin-1). It involves five measurements arranged in a cycle of pairwise

compatibility, forming the simplest non-trivial contextuality scenario beyond Bell-type setups. This pentagon structure is naturally expressed in graph-theoretic formulations of contextuality and exclusivity [33].

The scenario consists of five rank-1 projectors $\{\Pi_i\}_{i=1}^5$ constructed such that adjacent projectors (in the cyclic ordering) are orthogonal:

$$\Pi_i \Pi_{i+1} = 0 \quad \text{for } i = 1, 2, \ldots, 5 \text{ (indices mod 5)}. \tag{2.12}$$

Orthogonality ensures that adjacent projectors commute and can be measured jointly, defining five two-element contexts: $\{(\Pi_1, \Pi_2), (\Pi_2, \Pi_3), (\Pi_3, \Pi_4), (\Pi_4, \Pi_5), (\Pi_5, \Pi_1)\}$. Non-adjacent projectors, however, are not orthogonal and cannot be measured together.

In any noncontextual hidden-variable model, each projector must be assigned a definite value in $\{0, 1\}$ (corresponding to "true" or "false"). The exclusivity constraints from orthogonality imply that in each context, at most one projector can be assigned value 1. One way to see the resulting global constraint is to represent the orthogonality relations as a pentagon graph. The vertices represent the projectors $\Pi_1, \ldots, \Pi_5$ and two vertices are connected when the corresponding projectors are orthogonal. Now a deterministic assignment $v(\Pi_i) \in \{0, 1\}$ can mark a vertex with "1" only if none of its neighbours are marked (because adjacent projectors are exclusive). On a 5-cycle this immediately limits how many 1's one can place: once one chooses one vertex, its two neighbours must be 0, and among the remaining two vertices at most one more can be 1. Hence any noncontextual model can have at most two projectors simultaneously assigned value 1. Figure 2.1 visualizes the maximal pattern. Averaging over the hidden-variable distribution yields the KCBS inequality:

$$\sum_{i=1}^{5} \langle \Pi_i \rangle \leq 2. \tag{2.13}$$

Quantum mechanics predicts violations of this bound. In quantum theory the expectations $\langle \Pi_i \rangle = \mathrm{Tr}(\rho \Pi_i)$ come from a single state ρ and projectors obeying Eq. (2.12), rather than from convex mixtures of deterministic 0/1 assignments. For the standard symmetric KCBS choice in $d = 3$ (five vectors equally spaced on a cone, with adjacent ones orthogonal), one can take ρ to be the pure state aligned with the cone axis. In that case

$$K := \sum_{i=1}^{5} \Pi_i. \tag{2.14}$$

and $\sum_i \langle \Pi_i \rangle = \mathrm{Tr}(\rho K) = \sqrt{5}$. Equivalently, $\sqrt{5}$ is the largest eigenvalue of K for this

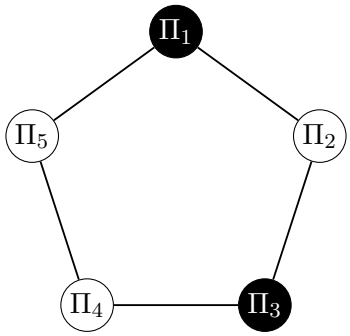


Figure 2.1: KCBS exclusivity graph: vertices are projectors and edges connect orthogonal (hence mutually exclusive) pairs. Any deterministic noncontextual assignment may label a vertex with 1 only if its neighbours are labelled 0. The highlighted vertices show a largest allowed choice (two non-adjacent 1's), which yields the noncontextual bound $\sum_i \langle \Pi_i \rangle \leq 2$.

construction. Hence, with these particular measurements and this state,

$$\sum_{i=1}^{5} \langle \Pi_i \rangle_{\max} = \sqrt{5} \approx 2.236, \tag{2.15}$$

thereby demonstrating contextuality. This violation is state-dependent: not all qutrit states violate the inequality.

2.3 Contextual Fraction

While inequality violations and Kochen–Specker-type contradictions witness contextuality, they are not ideal for quantifying the amount of contextuality in a scenario. They do not by themselves answer a more basic "how much?" question. The *contextual fraction* (CF) of Abramsky, Barbosa, and Mansfield [3] addresses this by turning a table of observable statistics into a single number in $[0, 1]$. Intuitively, CF asks: what is the largest fraction of the observed behavior that can still be explained by a noncontextual model? The remainder is the irreducibly contextual part.

An empirical model e for a scenario $(X, \mathcal{C}, O)$ is the collection of context-wise distributions $\{p_C\}_{C \in \mathcal{C}}$ satisfying no-disturbance (Section 2.2.2). Such an e is *noncontextual* precisely when it arises from mixing global value assignments (Eq. (2.11)). Geometrically, the noncontextual empirical models form a convex polytope inside the set of compatible models.

The contextual fraction is defined by the best convex decomposition of e into a noncontextual part plus "whatever is left." Concretely, consider decompositions

$$e = \lambda\, e^{\mathrm{NC}} + (1-\lambda)\, e', \tag{2.16}$$

where e^{NC} is noncontextual, e' is any valid empirical model, and $\lambda \in [0,1]$ is the weight of the noncontextual component. The *noncontextual fraction* is the largest such weight,

$$\mathrm{NCF}(e) := \max\{\lambda : e = \lambda\, e^{\mathrm{NC}} + (1-\lambda)\, e' \text{ for some } e^{\mathrm{NC}}, e'\}. \tag{2.17}$$

The *contextual fraction* is the complementary weight,

$$\mathrm{CF}(e) := 1 - \mathrm{NCF}(e). \tag{2.18}$$

In this form, CF has an immediate meaning. If $\mathrm{CF}(e) = 0$, the data admit a fully noncontextual explanation. If $\mathrm{CF}(e) = \varepsilon$, then at most a fraction $1-\varepsilon$ of the observed statistics can be accounted for by any noncontextual model; the remaining fraction is unavoidable if one insists on reproducing e. At the extreme $\mathrm{CF}(e) = 1$, no noncontextual part can be "peeled off." This idea mirrors the "local fraction" (or "local content") used in Bell nonlocality, where one asks how much of a correlation can be written as a convex mixture of local and arbitrary nonsignalling components [48]. The contextual fraction is the contextuality analogue: the noncontextual polytope plays the role of the local polytope, and the no-disturbance set plays the role of the nonsignalling set.

2.3.1 Computation via linear programming

The definition of $\mathrm{NCF}(e)$ is an optimization over a convex polytope, so it can be computed by linear programming. The LP formulation is also conceptually useful: it makes explicit that CF is a best fit of the observed data by mixing deterministic global assignments.

Let $S := O^X$ denote the set of all global value assignments (functions assigning an outcome to each measurement). Each assignment $s \in S$ defines a deterministic noncontextual model. Introduce nonnegative weights $\{w_s\}_{s\in S}$ for each global assignment. One searches for the largest total weight that can be assigned to these deterministic behaviors while staying componentwise below the observed probabilities:

$$\begin{aligned} \text{maximize} \quad & \sum_{s\in S} w_s \\ \text{subject to} \quad & \sum_{s\in S : s|_C = o_C} w_s \le p_C(o_C) \quad \text{for all } C \in \mathcal{C},\ o_C \in O^C, \\ & w_s \ge 0 \quad \text{for all } s \in S. \end{aligned} \tag{2.19}$$

The optimal value is $\mathrm{NCF}(e)$, and hence $\mathrm{CF}(e) = 1 - \mathrm{NCF}(e)$. From an operational standpoint, the constraints say that the candidate noncontextual explanation must fit inside the observed table of probabilities: for each context and outcome event, it cannot assign more weight to that event than the experiment actually exhibits. The dual of this LP yields an optimal noncontextuality inequality witness for the empirical model [3].

The number of variables in the LP is $|S| = |O|^{|X|}$, which grows exponentially in the number of measurements. In general there is no avoiding this worst-case scaling, but in scenarios with additional algebraic structure one can often reduce the effective number of deterministic assignments that must be considered.

2.4 Phase-Space Representations and the Discrete Wigner Function

Phase-space representations provide a useful classical-analogue language for finite-dimensional quantum systems. Instead of describing a state by a density operator ρ, one represents it by a real-valued function on a discrete phase space, in close analogy with classical statistical mechanics. The price for this analogy is that one cannot, in general, retain the full classical probability calculus for all quantum states and measurements. In Wigner-type representations this departure is often visible directly as negativity of the state function; by contrast, in other phase-space representations the state function can be everywhere nonnegative (for example, the Husimi Q function), but the classical analogy still fails in how measurement probabilities are computed: the corresponding measurement kernels (or response functions) are not those of an ordinary classical coarse-graining [34, 49]. In the following subsections we review quasiprobability representations with a focus on the discrete Wigner function and the interpretation of Wigner negativity.

2.4.1 Quasiprobabilities and the meaning of negativity

A quasiprobability representation associates to each quantum state ρ a real-valued function W_ρ on a phase space Ω. Typically one requires (i) affinity and informational completeness, so that ρ can be reconstructed from W_ρ, and (ii) that the probabilities of a specified family of measurements are obtained from W_ρ by linear functionals, in analogy with classical coarse-graining [49, 50, 51]. The original Wigner function was introduced in the continuous-variable setting [128], and many finite-dimensional analogues have since been developed.

Two general points carry over to the discrete setting. First, phase-space representations are not unique: different choices correspond to different operator frames (and hence different "phase-point" conventions) [49, 50, 51]. Second, one should not expect W_ρ to define a genuine probability distribution for all quantum states. Under mild and physically natural assumptions on how states and measurements are represented, one cannot obtain a quasiprobability representation that is nonnegative for all quantum states; some states must exhibit negativity (or, equivalently, the representation must depart from the standard rules of classical probability) [115, 50, 51, 49].

Wigner negativity indicates that W_ρ cannot be interpreted as a classical hidden-variable distribution over phase-space points that reproduces the relevant measurement statistics by ordinary marginalization [115, 49]. Conversely, if $W_\rho(\alpha) \geq 0$ for all α, then W_ρ can serve as a genuine probability distribution, and one may hope to build a classical simulation by sampling phase-space points according to W_ρ. This idea becomes powerful when applied to a restricted subtheory (a subset of states and operations) for which Wigner positivity is preserved throughout the computation; in odd-dimensional stabilizer quantum mechanics, exactly this situation arises and underlies several efficient classical simulation results [59, 85, 122].

2.4.2 Gross discrete Wigner function (odd dimension)

We now specialize to the discrete Wigner representation used throughout the thesis. Among the various finite-dimensional constructions, the formulation of Gross [59] is particularly convenient in odd local dimension because it is covariant under Heisenberg–Weyl translations and it admits a sharp characterization of Wigner-positive pure states (the discrete Hudson theorem [59]). Wootters' construction [130] provides an earlier formulation in prime dimension, and related finite-field approaches emphasize the underlying affine-geometry structure [55, 132].

Fix an odd dimension d and write $\mathbb{Z}_d$ for integers modulo d. The single-qudit discrete phase space is

$$\Omega := \mathbb{Z}_d \times \mathbb{Z}_d, \tag{2.20}$$

whose elements $\alpha \in \Omega$ label phase-space points.

Gross' construction assigns to each point $\alpha \in \Omega$ a Hermitian *phase-point operator* A_α.

We will not need an explicit formula for A_α here. The key property is covariance under Clifford operations. If U is a Clifford unitary, it acts on phase space by an affine

symplectic transformation S_U, and the phase-point operators transform covariantly in the same convention [59]:

$$UA_\alpha U^\dagger = A_{S_U(\alpha)}. \tag{2.21}$$

We give an explicit construction in Chapter 6 (Eq. (6.28)).

The family $\{A_\alpha\}_{\alpha\in\Omega}$ forms an orthogonal operator basis, normalized so that each A_α has unit trace. For later use it is helpful to record the standard identities [59, 130]:

$$\mathrm{Tr}(A_\alpha) = 1, \qquad \mathrm{Tr}(A_\alpha A_\beta) = d\,\delta_{\alpha\beta}, \qquad \sum_{\alpha\in\Omega} A_\alpha = d\,\mathbb{I}. \tag{2.22}$$

Different phase conventions for the Heisenberg–Weyl group lead to notationally different but equivalent Wigner functions; the positivity/negativity questions considered below do not depend on these choices.

Given a density operator ρ, its (Gross) discrete Wigner function is the real function $W_\rho : \Omega \to \mathbb{R}$ defined by

$$W_\rho(\alpha) := \frac{1}{d}\,\mathrm{Tr}(\rho A_\alpha). \tag{2.23}$$

The normalization is immediate from Eq. (2.22):

$$\sum_{\alpha\in\Omega} W_\rho(\alpha) = 1. \tag{2.24}$$

Since $\{A_\alpha\}$ is a basis, the map $\rho \mapsto W_\rho$ is informationally complete and one has the reconstruction formula

$$\rho = \sum_{\alpha\in\Omega} W_\rho(\alpha)\, A_\alpha. \tag{2.25}$$

In odd prime (and more generally prime-power) dimensions, the finite geometry of Ω can be organized into families of parallel affine lines ("striations"). In the standard discrete Wigner constructions, each striation corresponds to a rank-1 projective measurement in a stabilizer (Pauli) basis, and each outcome corresponds to one line in that striation. The Born probability of that outcome is obtained by summing $W_\rho(\alpha)$ over the points α on the associated line [132, 130, 59]. This is the discrete analogue of recovering position or momentum marginals from the continuous-variable Wigner function.

The same geometry also yields an explicit link between phase-point operators and stabilizer projectors, which we use directly in Chapter 6.

For the purposes of this thesis, the central qualitative feature is:

$$\exists \alpha \in \Omega \text{ with } W_\rho(\alpha) < 0 \quad \Longrightarrow \quad \rho \text{ is Wigner-negative.} \tag{2.26}$$

Wigner negativity obstructs interpreting W_ρ as an ordinary probability distribution on phase space.

For odd local dimension, Wigner positivity has a simple characterization on *pure* states. Gross' discrete Hudson theorem [59] states that a pure state has a nonnegative discrete Wigner function if and only if it is a stabilizer state. For mixed states, the picture is more nuanced. The convex hull of pure stabilizer states (the *stabilizer polytope*) is contained in the set of Wigner-positive states, but the inclusion is strict for $d \geq 3$ [59]. Thus Wigner negativity is a simple sufficient certificate of non-stabilizer character, while Wigner positivity alone does not imply that a state is a stabilizer mixture.

The discrete Wigner representation is often discussed alongside the stabilizer formalism. In odd prime (and more generally odd prime-power) dimensions, Clifford unitaries act as affine symplectic transformations on phase space and preserve Wigner positivity in the Gross representation [59]. As a result, stabilizer computations that remain Wigner-positive throughout admit efficient classical simulation by sampling from W_ρ and updating phase-space points under the corresponding affine maps [122]. More generally, quasiprobability simulation algorithms incur overheads controlled by suitable measures of negativity (such as ℓ_1-type norms), which motivates treating Wigner negativity as a resource in stabilizer-based models [95, 123].

Contextuality provides a complementary and, in some settings, equivalent perspective. Spekkens showed that negativity in quasiprobability representations and contextuality can be viewed as two sides of the same non-classicality obstruction [115]. For multi-qudit systems of odd local dimension and Pauli measurement scenarios, Delfosse *et al.* proved an explicit equivalence between noncontextuality and Wigner positivity [42]; the single-qudit marginal version developed in Chapter 6 is one application of this correspondence.

Chapter 3

Multipartite Entanglement versus Genuine Multipartite Nonlocality

Multipartite entanglement is a useful experimental resource across platforms, but its operational meaning becomes increasingly subtle as the number of parties grows. A key motivation is device-independent: if one wants to certify that an experiment truly exhibits non-classical correlations *without* trusting a detailed model of the devices, a Bell test provides an operational benchmark. However, even in the bipartite setting, Bell nonlocality and entanglement do not coincide. Not every entangled mixed state violates a Bell inequality [29], and the strength of Bell violation is not a monotone of standard entanglement measures. In particular, there are entangled states admitting local hidden-variable models for all projective measurements [127]. For multiqubit pure states the relation is even more subtle, and entanglement and nonlocality can be inequivalent for any number of parties [137, 13].

In multipartite systems this mismatch is more pronounced, because the key question is not just whether the correlations are nonlocal, but whether they are irreducibly N-partite. Since Svetlichny's original proposal [118], the standard picture is that a correlation can be nonlocal while still admitting a hybrid decomposition, in which a subset of parties shares nonlocal resources and the remainder is only locally correlated. Ruling out all such hybrid models is what is meant by *genuine multipartite nonlocality* (GMN). For the 2-settings/2-outcomes scenario considered here, GMN is typically witnessed via violations of Svetlichny-type inequalities and their N-party generalizations (see Section 2.1.2 and Refs. [40, 15]).

Understanding when GMN is present matters both conceptually and pragmatically.

Conceptually, it distinguishes "global" non-classicality from correlations that could be reproduced by wiring together smaller nonlocal subsystems. Operationally, it sets a device-independent standard for tasks that aim to harness *irreducible* multipartite resources. Examples include device-independent cryptography and multiuser key agreement [7, 106, 65], device-independent randomness certification [100], and scalable probes of many-body correlations [52]. They also underpin network primitives such as quantum communication between many parties and device-independent secret sharing [109, 89], and connect closely to self-testing and device-independent entanglement certification and quantification [23, 91, 30, 90, 16]. Related multipartite notions appear in steering [63] and in approaches to indefinite causal order and multipartite noncausality [41, 2, 20].

A central quantitative question is therefore how entanglement in a given state family translates into Svetlichny-type violations. For three qubits, this question has a relatively complete answer for important families. For the three-qubit generalized GHZ family, states of the form $\cos\alpha\,|000\rangle + \sin\alpha\,|111\rangle$, the Svetlichny inequality is violated only when the three-tangle exceeds $1/2$ [54]. For larger N, however, it has been unclear whether such threshold behavior persists and how it scales with N.

Multipartite entanglement has many inequivalent structures. Even restricting to pure states, different SLOCC classes (such as GHZ and W) exhibit distinct correlation geometries and can behave differently under the same set of Bell tests [46, 6]. Thus, beyond scalar comparisons of "amount of entanglement," one must ask to what extent GMN is controlled by the distribution of coherence and entanglement across parties.

This chapter provides an analytical characterization of this relationship within a clean and widely studied Bell scenario [117]. We quantify genuine multipartite entanglement using the n-tangle [129] and GMN using Svetlichny-type inequalities. We compare two paradigmatic GHZ-class families: generalized GHZ (GGHZ) states and maximal slice states. Both are analytically tractable while still capturing qualitatively different entanglement structures. We find a clear contrast: for GGHZ states, a Svetlichny violation appears only above a finite, N-independent threshold. For maximal slice states, any nonzero n-tangle can be witnessed as GMN, and the optimized violation grows monotonically with entanglement. Overall, these results show that in multipartite settings, non-classical correlations depend strongly on the state structure: entanglement measures capture inseparability, but irreducible N-party nonlocality depends on how coherence is distributed across the Hilbert space, not just on a single scalar monotone.

3.1 State Families and Parametrization

We study two families of pure N-qubit states, each parameterized by a single continuous angle allowing interpolation between product states and maximally entangled states. Both state families are well-defined for arbitrary $N > 2$.

3.1.1 Generalized GHZ (GGHZ) states

The generalized GHZ family is defined as

$$|\psi_g(\alpha)\rangle = \cos\alpha|0\rangle^{\otimes N} + \sin\alpha|1\rangle^{\otimes N}, \tag{3.1}$$

where $\alpha \in [0, \pi/2]$. This family interpolates between the product state $|0\rangle^{\otimes N}$ (at $\alpha = 0$) and the symmetric Greenberger–Horne–Zeilinger state $|\mathrm{GHZ}\rangle = (|0\rangle^{\otimes N} + |1\rangle^{\otimes N})/\sqrt{2}$ (at $\alpha = \pi/4$), then continues to the opposite product state $|1\rangle^{\otimes N}$ (at $\alpha = \pi/2$).

The n-tangle for this family has the closed-form expression

$$\tau_n(\psi_g) = \sin^2(2\alpha). \tag{3.2}$$

The tangle vanishes at the product-state limits $\alpha = 0, \pi/2$ and reaches its maximum value $\tau_n = 1$ at the symmetric superposition $\alpha = \pi/4$. For even N, the functional form is symmetric around $\alpha = \pi/4$.

3.1.2 Maximal slice states

The maximal slice family is defined as

$$|\psi_s(\alpha)\rangle = \frac{1}{\sqrt{2}}\left[|0\rangle^{\otimes N} + |1\rangle^{\otimes(N-1)}\left(\cos\alpha|0\rangle + \sin\alpha|1\rangle\right)\right], \tag{3.3}$$

with $\alpha \in [0, \pi/2]$.

The maximal slice family differs from GGHZ in the entanglement distribution: the last qubit interpolates from $|0\rangle$ to $|1\rangle$ while maintaining a coherent superposition with the all-zeros string. The terminology "maximal slice" originates from the geometric structure of three-qubit entanglement [35]. For three qubits, the space of genuinely entangled pure states (modulo local unitaries) can be parametrized by five real parameters [6]. The "maximal slice" is a two-dimensional submanifold of this space that interpolates between

product states and the GHZ state, while maintaining a specific asymmetric entanglement structure. For general N, we use the natural extension of this construction, preserving the defining feature: one qubit carries a variable superposition while the others remain in a fixed configuration.

For this family the n-tangle evaluates to

$$\tau_n(\psi_s) = \sin^2(\alpha). \tag{3.4}$$

This matches the three-qubit maximal-slice family, for which the three-tangle takes the same form [54, 8]. Like the GGHZ family in Eq. (3.2), this expression depends only on the interpolation parameter α (for the even-N case).

3.2 Svetlichny Inequality for N-Qubit Systems

To quantify genuine multipartite nonlocality, we use Svetlichny-type inequalities for N qubits. The conceptual framework was reviewed in Section 2.1.2; here we specify the concrete form used in the numerical and analytical analysis.

For N qubits, the Svetlichny operator generalizes the two-qubit CHSH operator to witnessing genuine N-partite nonlocality. Each party i measures one of two dichotomic observables A_i^0 or A_i^1. The joint measurement outcomes are combined into correlation functions of the form

$$\langle A_1^{x_1} \otimes A_2^{x_2} \otimes \cdots \otimes A_N^{x_N} \rangle, \tag{3.5}$$

where $x_i \in \{0, 1\}$ selects which observable party i measures.

Following the standard construction (see, e.g., [40]; we use the same conventions as [117]), the N-qubit Svetlichny operator is

$$S_N^{\pm} := \sum_{\mathbf{x}\in\{0,1\}^N} \nu^{\pm}(\mathbf{x}) \, (A_1^{x_1} \otimes \cdots \otimes A_N^{x_N}) \,, \tag{3.6}$$

with coefficients defined by the Hamming weight $w(\mathbf{x})$ as

$$\nu^{\pm}(\mathbf{x}) := (-1)^{w(\mathbf{x})(w(\mathbf{x})\pm 1)/2}. \tag{3.7}$$

In any Svetlichny-local (hybrid) model,

$$\left|\langle S_N^{\pm} \rangle\right| \leq S_N^{\mathrm{SL}} := 2^{N-1}. \tag{3.8}$$

See also Ref. [112] for related Bell-type inequalities capturing partial separability.

For the analytical results in Sections 3.3.2 and 3.3.3, we consider the *largest* Svetlichny value attainable from a given state when each party is free to choose their two local observables $\{A_i^0, A_i^1\}$. Equivalently, we compare the Svetlichny-local bound to

$$S^{\pm}_{N,\max}(\psi) := \max_{\{A_i^0, A_i^1\}} \left|\langle S^{\pm}_N \rangle_\psi\right|, \tag{3.9}$$

the maximum of $\left|\langle S^{\pm}_N \rangle\right|$ over all local projective measurement directions. This optimization is nontrivial because Eq. (3.6) contains 2^N correlators whose contributions can cancel or add, depending on how the local measurement phases are chosen. For the GHZ-class families considered here the maximum can be obtained in closed form, and there exist explicit measurement settings that attain it. For instance, for GHZ-class states the optimal measurements can be chosen in the equatorial (XY) plane [86, 40], where suitable relative azimuthal angles align the interference contributions across the Svetlichny sum.

The maximum quantum value of $\left|\langle S^{\pm}_N \rangle\right|$ equals $\sqrt{2}\,2^{N-1}$ for the maximally entangled N-qubit GHZ state (both even and odd N). For other state families, the maximum depends on both the state structure and the measurement choices, and determining it is challenging in general [19, 134]: one must optimize over $4N$ continuous measurement angles (two Bloch-sphere angles for each of the two settings at each party), while each evaluation of $\langle S^{\pm}_N \rangle$ combines 2^N correlators, so the raw cost of evaluating the objective scales as $\mathcal{O}(2^N)$.

For the remainder of this chapter, we work directly with the unnormalized expectation value $\langle S^{\pm}_N \rangle$. In particular, genuine multipartite nonlocality is certified whenever

$$\left|\langle S^{\pm}_N \rangle\right| > 2^{N-1}. \tag{3.10}$$

3.3 Main Results: Thresholds and Monotonicity

We now present the central analytical results for the measurement-optimized Svetlichny values of the two state families. For each family we obtain a closed-form expression for the optimum $S^{\pm}_{N,\max}$ as a function of the state parameter α, valid for any number of qubits $N > 2$. These formulas provide direct, device-independent benchmarks for genuine multipartite nonlocality in the standard two-settings/two-outcomes Bell scenario. For even N we can additionally express the optima in terms of the n-tangle, which allows a comparison between multipartite entanglement and Svetlichny-type violations within each family.

3.3.1 Maximum Svetlichny values for arbitrary N

We begin by stating $S^{\pm}_{N,\max}(\alpha)$ for arbitrary $N > 2$. The measurement optimizations are derived in Appendix A (see in particular Sections A.1 and A.2). Here we only quote the final closed-form results.

GGHZ family (all $N > 2$)

For generalized GHZ states $|\psi_g(\alpha)\rangle$ in Eq. (3.1), the maximum Svetlichny value over all local projective measurements can be obtained analytically. We present the resulting piecewise expressions here; the full maximization is given in Section A.1 of Appendix A.

For *odd* $N > 2$ one obtains

$$S^{\pm}_{N,\max}(\psi_g) = \begin{cases} 2^{\frac{N+1}{2}} \left|\cos(2\alpha)\right|, & \left|\tan(2\alpha)\right| \leq 2^{1-\frac{N}{2}}, \\ \sqrt{2}\, 2^{N-1} \left|\sin(2\alpha)\right|, & \left|\tan(2\alpha)\right| \geq 2^{1-\frac{N}{2}}. \end{cases} \tag{3.11}$$

For *even* $N > 2$ one obtains

$$S^{\pm}_{N,\max}(\psi_g) = \begin{cases} 2^{\frac{N}{2}}, & \left|\sin(2\alpha)\right| \leq 2^{\frac{1-N}{2}}, \\ \sqrt{2}\, 2^{N-1} \left|\sin(2\alpha)\right|, & \left|\sin(2\alpha)\right| \geq 2^{\frac{1-N}{2}}. \end{cases} \tag{3.12}$$

Equation (3.12) is the starting point for the entanglement-threshold discussion below; rewriting it in terms of τ_n yields Eq. (3.14).

Maximal slice family (all $N > 2$)

For maximal slice states $|\psi_s(\alpha)\rangle$ in Eq. (3.3), the measurement optimization can also be carried out in closed form. We quote the final expression here and defer the derivation to Section A.2 of Appendix A. For both even and odd $N > 2$ one finds [117]:

$$S^{\pm}_{N,\max}(\psi_s) = 2^{N-1} \sqrt{1 + \sin^2 \alpha}. \tag{3.13}$$

This immediately implies Svetlichny violation for any $\alpha \neq 0$.

3.3.2 GGHZ states: Threshold independent of N

We now connect the general nonlocality result for GGHZ states to entanglement for even N. For even $N > 2$, Eq. (3.12) gives a closed-form expression for the maximum expectation value of the Svetlichny operator over all local projective measurements. Writing the result in terms of the n-tangle $\tau \equiv \tau_n(\psi_g) = \sin^2(2\alpha)$, one obtains

$$S^{\pm}_{N,\max}(\psi_g) = \begin{cases} 2^{\frac{N}{2}}, & \tau \leq 2^{1-N}, \\ 2^{N-1}\sqrt{2\,\tau}, & \tau \geq 2^{1-N}. \end{cases} \tag{3.14}$$

In the second branch the maximal value grows as $\sqrt{\tau}$, while in the first branch it is constant and equals the best value attainable by a product state. The critical threshold corresponds to the point at which the maximal value in Eq. (3.14) crosses the Svetlichny-local bound 2^{N-1}.

Because the violation condition is $2^{N-1}\sqrt{2\tau} > 2^{N-1}$, the Svetlichny inequality is violated iff $\tau > 1/2$.

Theorem 3.1 (GGHZ entanglement threshold)**.** *For the generalized GHZ family $|\psi_g(\alpha)\rangle$ with even $N > 2$, the Svetlichny inequality is* not violated *whenever the n-tangle satisfies*

$$\tau_n(\psi_g) \leq \frac{1}{2}. \tag{3.15}$$

This threshold is independent of N.

This result has immediate operational consequences:

- **Universality:** The critical threshold $\tau_n^{\text{crit}} = 1/2$ holds for *any even number of qubits* (even $N > 2$).
- **Robustness:** States with $\tau_n < 1/2$ cannot be certified as genuinely multipartite nonlocal by Svetlichny violations, even though they are genuinely multipartite entangled for $\tau_n > 0$.
- **Piecewise response:** For fixed even N, $S^{\pm}_{N,\max}$ is flat at small τ_n (product-like branch) and then grows as $\sqrt{\tau_n}$; as a function of α it increases up to $\alpha = \pi/4$ and decreases symmetrically.

3.3.3 Maximal slice states: Monotonic violation for any nonzero entanglement

The maximal slice family exhibits qualitatively different behavior. Unlike GGHZ states, maximal slice states do not exhibit a threshold: any nonzero entanglement suffices for Svetlichny violation, provided the measurement settings are appropriately optimized.

The measurement settings that maximize the Svetlichny value for maximal slice states differ from those that maximize the value for GGHZ states. In particular, the last party requires a different choice of measurement angles to attain the optimum.

Optimizing over all local measurement angles yields the maximum Svetlichny value for maximal slice states. For arbitrary $N > 2$ this is Eq. (3.13); for even $N > 2$, rewriting $\sin^2 \alpha$ as $\tau_n(\psi_s)$ gives:

$$S^{\pm}_{N,\max}(\psi_s) = 2^{N-1}\sqrt{1 + \tau_n(\psi_s)}. \tag{3.16}$$

Comparing with the Svetlichny-local bound 2^{N-1}, violation occurs iff $\tau_n(\psi_s) > 0$.

Theorem 3.2 (Maximal slice monotonic violation)**.** *For the maximal slice family $|\psi_s(\alpha)\rangle$ with even $N > 2$, there exists a choice of local measurement settings such that:*

1. *The Svetlichny inequality is violated whenever $\tau_n(\psi_s) > 0$.*
2. *The violation $S^{\pm}_{N,\max}(\psi_s) - 2^{N-1}$ increases* monotonically *with $\tau_n(\psi_s)$.*
3. *The functional form of $S^{\pm}_{N,\max}(\psi_s)$ in terms of $\tau_n(\psi_s)$ is identical to the three-qubit case previously derived in Refs. [54, 8], and is independent of N.*

This contrasts with the GGHZ case:

- **No threshold:** Any nonzero entanglement can be converted into genuine multipartite nonlocality for maximal slice states.
- **Monotonicity:** More entanglement always implies stronger Svetlichny violation.
- **Dimension-independence:** The violation does not "dilute" as N increases; the relationship between τ_n and violation remains constant.

The absence of a forbidden region below a critical threshold is a qualitative difference from the GGHZ family.

3.3.4 Comparative summary

The table below summarizes the contrasting behavior of the two families.

Table 3.1: Comparison of GGHZ and maximal slice families: entanglement versus nonlocality

Property	**GGHZ**	**Maximal slice**
General-N optimum $S^{\pm}_{N,\max}(\alpha)$	Eqs. (3.11), (3.12)	Eq. (3.13)
Critical τ_n threshold (even $N > 2$)	$1/2$	0
Monotonicity of $S^{\pm}_{N,\max}$ vs τ_n	Non-monotonic (piecewise)	Monotonic
N-dependence of $S^{\pm}_{N,\max}$ at fixed τ_n	Scales with N	Scales with N
Entanglement distribution	Symmetric	Asymmetric
Coherence structure	Global interference	Localized interference

3.4 Discussion

In this chapter, we have shown a closed-form characterization of the measurement-optimized Svetlichny violation attainable from two paradigmatic extensions of GHZ-class families, for arbitrary qubit number $N > 2$. These general-N maxima provide a device-independent benchmark for genuine multipartite nonlocality that is valid for both even and odd N. For even N, we additionally express the optima in terms of the n-tangle, yielding an explicit link between entanglement and Svetlichny-type violations for these families of states. Taken together they show that the two families exhibit genuinely different nonlocality behavior under the same Bell test, despite having simple one-parameter entanglement descriptions.

For the GGHZ family, the optimized Svetlichny value is piecewise (Eq. (3.14)). At small τ_n, the global maximum is attained by the same measurement strategy that is optimal for product states, giving a constant value $2^{N/2}$. Only once the "GHZ-interference" branch dominates does the optimum scale as $2^{N-1}\sqrt{2\tau_n}$. As a consequence, GMN can be certified only when the tangle exceeds a universal activation threshold,

$$\tau_n(\psi_g) > \frac{1}{2}, \tag{3.17}$$

independent of the even qubit number $N > 2$ (Theorem 3.1). Operationally, this identifies a broad region of genuinely multipartite entangled GGHZ states that remain Svetlichny-local. In other words, within this family the Svetlichny test is a "threshold" witness: it does not respond continuously to small increases of τ_n starting from zero.

For the maximal slice family, by contrast, the measurement optimization yields a single closed form (Eq. (3.16)),

$$S^{\pm}_{N,\max}(\psi_s) = 2^{N-1}\sqrt{1+\tau_n(\psi_s)}. \tag{3.18}$$

Here the Svetlichny-local bound is exceeded for any nonzero tangle, and the violation increases monotonically with τ_n (Theorem 3.2). Thus, for maximal slice states the Svetlichny inequality functions as a sensitive probe of genuine multipartite entanglement: once the state departs from biseparability, the same departure can immediately be converted into a GMN certificate by suitable local measurement choices.

The contrast between the families can be traced to the coherence structure that the Svetlichny operator is able to amplify. In GGHZ states, the only coherent components are $|0\rangle^{\otimes N}$ and $|1\rangle^{\otimes N}$. Svetlichny violation relies on interference between these two macroscopically distinct strings under equatorial measurements. When τ_n is small, this interference term is too weak to dominate the product-like branch of the optimization, leaving the correlations compatible with a hybrid (Svetlichny-local) model even though the state is not biseparable. Maximal slice states, on the other hand, approach the GHZ point through an asymmetric region of state space in which one qubit carries the variable superposition. This asymmetry enlarges the set of measurement phases that can be chosen to align the contributing correlators in the Svetlichny sum. As a result, even a small but nonzero τ_n can be made to contribute constructively across the 2^N terms, producing a violation immediately. This provides an intuitive explanation for why the maximal slice relationship mirrors the familiar two-qubit pure-state behavior (entanglement $\Rightarrow$ CHSH violation) while the GGHZ family does not.

These analytic benchmarks are useful in two complementary ways. They quantify the minimum entanglement cost for device-independent tasks that require GMN when one is constrained to GHZ-class resources: within the GGHZ family, no amount of optimization over local projective measurements can bypass the universal threshold $\tau_n = 1/2$. They also identify maximal-slice-type states as favorable candidates in noise-limited settings, since any departure from biseparability can in principle be turned into a Svetlichny violation. More broadly, related measures of multipartite nonlocality can be used to formalize stronger nonlocal resources beyond Svetlichny-type violations [14].

Chapter 4

Non-Classicality as a Dynamical Signature of Chaos: The Quantum Kicked Top

Chaos arises in deterministic dynamical systems when nonlinear evolution produces effectively unpredictable behavior. In classical mechanics it is associated with nonlinear stretching-and-folding of phase space. Quantum mechanics complicates this picture, motivating the search for quantum observables whose behavior tracks the regular-versus-chaotic structure of an underlying classical limit [61]. Well-established examples include random-matrix spectral statistics [25], stability diagnostics based on fidelity/Loschmidt echoes [97, 69, 56], entanglement growth (in composite or encoded descriptions) [17, 88], and operator scrambling diagnosed by out-of-time-ordered correlators [79, 84, 107].

Classical chaos is diagnosed by sensitivity to initial conditions. Infinitesimally close trajectories separate exponentially,

$$\delta x(t) \sim \delta x(0)\, e^{\lambda t}, \tag{4.1}$$

with rate set by the largest Lyapunov exponent $\lambda > 0$. This trajectory-based view does not transfer directly to quantum dynamics [61]. Unitary evolution preserves state overlaps,

$$|\langle \psi_1(t)|\psi_2(t)\rangle| = |\langle \psi_1(0)|\psi_2(0)\rangle|, \tag{4.2}$$

so proximity of pure states is not amplified in time. In addition, the uncertainty principle prevents arbitrarily sharp phase-space localization, so the notion of a trajectory is only

approximate. These obstructions motivate the search for intrinsically quantum signatures that correlate with regular-versus-chaotic motion in the classical limit. Our focus is on testing a specific, experimentally interpretable witness of non-classicality as a chaos-correlated marker.

Our model system is the *quantum kicked top* (Section 4.1). It is a standard testbed because a single parameter, the kick strength κ, tunes the associated classical map (on the unit sphere) from mostly regular motion to predominantly chaotic motion [62, 61]. To compare quantum behavior to the classical phase portrait we initialize the dynamics in spin coherent states, the minimum-uncertainty states most naturally associated with classical phase-space points [103, 12, 96, 61].

The contextuality witness used here is the KCBS inequality (reviewed in Section 2.2.3) introduced by Klyachko *et al.* [72]. KCBS is state-dependent and native to spin-1 (qutrit) systems. It is well matched to the kicked-top setting because spin-1 coherent states satisfy the KCBS bound, while sufficiently delocalized superpositions can violate it. This aligns the contextuality notion of "classical" (noncontextual) with the semiclassical notion of "classical" (coherent and localized). As κ increases, the nonlinear twist tends to drive the evolving state away from the coherent-state manifold, so we test whether stronger classical chaoticity correlates with an increased tendency to generate KCBS violations.

4.1 The Kicked Top Model

The kicked top is a paradigmatic model of quantum chaos, introduced by Haake, Kuś, and Scharf [62] (see also the textbook treatment in Ref. [61]). It describes a spin-j angular momentum vector subject to periodic "kicks" that twist the spin about one axis, interspersed with free precession about another axis. The model has a well-defined classical limit as $j \to \infty$ and exhibits a transition from regular to chaotic dynamics controlled by a single parameter.

4.1.1 Hamiltonian, Floquet step, and classical limit

The kicked top Hamiltonian is

$$H = \frac{\hbar p}{\tau} J_y + \frac{\hbar \kappa}{2j} J_z^2 \sum_{n=-\infty}^{\infty} \delta(t - n\tau), \tag{4.3}$$

where $\mathbf{J}^2 = j(j+1)\hbar^2$ and the parameters have clear dynamical roles. The precession angle per period is set by p, while κ controls the strength of the nonlinear "twist" and serves as the chaoticity parameter. Over one period the evolution factorises into a rotation and a kick,

$$U = U_{\text{kick}} U_{\text{prec}} = \exp\left(-\frac{i\kappa J_z^2}{2j}\right) \exp\left(ipJ_y\right), \tag{4.4}$$

which defines the stroboscopic dynamics.

In the classical limit $j \to \infty$, the rescaled angular-momentum components $(X, Y, Z) := (J_x/j, J_y/j, J_z/j)$ define a classical point on the unit sphere, $X^2+Y^2+Z^2 = 1$. Writing the stroboscopic dynamics as a map $(X_n, Y_n, Z_n) \mapsto (X_{n+1}, Y_{n+1}, Z_{n+1})$, the classical kicked-top map for the commonly used choice $p = 0.5$ is

$$\begin{aligned} X_{n+1} &= Z_n \cos(\kappa X_n) + Y_n \sin(\kappa X_n), \\ Y_{n+1} &= Y_n \cos(\kappa X_n) - Z_n \sin(\kappa X_n), \\ Z_{n+1} &= -X_n. \end{aligned} \tag{4.5}$$

The corresponding classical map exhibits the familiar progression from regular to chaotic dynamics as κ is increased. For small κ the motion is organised around fixed points and invariant curves. For intermediate κ a mixed phase space appears with regular islands embedded in a chaotic sea. For sufficiently large κ the chaotic sea covers most of the sphere. At $p = 0.5$, this progression is structured by a sequence of bifurcations, including destabilization of a primary fixed point at $\kappa = 2$ and a prominent period-4 orbit at $\kappa = \pi$ [75]. The classical portrait (see Figs. 4.2 and 4.3, left panels) also contains specific organising structures that will reappear in the quantum signatures, notably the fixed points at $(X, Y, Z) = (0, \pm 1, 0)$ and a prominent period-4 orbit [62, 61].

For finite j, the kicked top evolves in the $(2j+1)$-dimensional Hilbert space. To make contact with the classical map we initialise the system in spin coherent states, which are minimum-uncertainty states localised around a point (θ, ϕ) on the sphere,

$$|\theta, \phi\rangle = R(\theta, \phi)|j, j\rangle, \tag{4.6}$$

with $R(\theta, \phi) = e^{-i\phi J_z/\hbar} e^{-i\theta J_y/\hbar}$. For background on spin coherent states and their phase-space interpretation, see Refs. [103, 12, 96]. Starting from $|\psi_0\rangle = |\theta_0, \phi_0\rangle$, we evolve stroboscopically,

$$|\psi_n\rangle = U^n |\psi_0\rangle, \tag{4.7}$$

and at each step quantify contextuality by the optimised KCBS value $S_*(\rho_n)$ and the associated normalised violation $\beta'(n)$ defined in Eq. (4.10).

4.2 The KCBS Inequality as a Contextuality Witness

4.2.1 KCBS inequality for spin-1 systems

The KCBS scenario is a 5-cycle of pairwise compatible rank-1 projectors, with the noncontextual bound and quantum maximum given in Eqs. (2.13) and (2.15). In this chapter we implement KCBS on a spin-1 Hilbert space using projectors onto the spin-0 eigenstates along five directions $\{\mathbf{n}_i\}_{i=1}^5$ whose adjacent pairs are orthogonal (equivalently, whose projectors satisfy the cyclic exclusivity constraint of Eq. (2.12)).

For a spin-1 system, we define the relevant rank-1 projectors as

$$\Pi_{\mathbf{n}}^0 = |\mathbf{n}, 0\rangle\langle\mathbf{n}, 0|, \tag{4.8}$$

where $|\mathbf{n}, 0\rangle$ is the eigenstate of $\mathbf{n} \cdot \mathbf{J}$ with eigenvalue 0.

For numerical evaluation, we treat the KCBS value as an optimized contextuality witness. Specifically, for each state ρ we maximize the KCBS expression (Eq. (2.13)) over all rank-1 projector sets satisfying the KCBS 5-cycle exclusivity constraints (see Ref. [72]):

$$S_*(\rho) := \max_{\{\Pi_i^0\}_{i=1}^5} \sum_{i=1}^5 \mathrm{Tr}[\Pi_i^0 \, \rho], \tag{4.9}$$

subject to the cyclic orthogonality constraints of Eq. (2.12). Importantly, the noncontextual bound and quantum maximum depend only on this compatibility/exclusivity graph, not on the particular coordinate realization [33].

To facilitate comparison across different states and parameters, we define the normalized optimized KCBS violation

$$\beta'(\rho) := \max\left(0, \frac{S_*(\rho) - 2}{\sqrt{5} - 2}\right), \tag{4.10}$$

so that $\beta'(\rho) \in [0, 1]$. Here $\beta'(\rho) = 0$ indicates no KCBS violation, while $\beta'(\rho) = 1$ corresponds to the quantum maximum. Along a trajectory we write $\beta'(t) := \beta'(\rho_t)$ for the KCBS time series.

4.3 Numerical Results: Global and Local Contextuality Signatures

4.3.1 Global signature: KCBS-violation fraction versus κ

To test whether stronger kicks, which produce more classical chaos, also produce more contextuality when averaged over initial conditions, we sample 1000 initial spin coherent states from the Haar-uniform measure on the sphere and evolve each for $T = 100$ Floquet steps. At each step we compute the optimized, normalized KCBS violation $\beta'(\rho_t)$ (Eq. (4.10)). An initial condition is declared contextual if $\beta'(\rho_t) > 0$ for at least one time step; the *KCBS-violation fraction* is the proportion of sampled initial conditions satisfying this criterion. Because the measure accumulates over many kicks, it is insensitive to where on the sphere any single trajectory begins.

Figure 4.1 plots this violation fraction against κ. The curve rises monotonically from near zero in the integrable regime ($\kappa \lesssim 1$) to a plateau in the predominantly chaotic regime ($\kappa \gtrsim 4$). The plateau reflects finite-size saturation: in the three-dimensional $j = 1$ Hilbert space with a finite observation window, eventually most initial conditions pass through at least one contextual state. The monotonic increase confirms that, in aggregate, stronger nonlinear kicks drive a larger fraction of initially classical coherent states into KCBS-violating regimes.

Notably, the curve exhibits two localized dips near $\kappa \approx 2.1$ and $\kappa \approx \pi$. These dips coincide with bifurcation points of the classical map at $p = 0.5$: at $\kappa = 2.1$ the fixed point $(X, Y, Z) = (0, 1, 0)$ loses stability, and at $\kappa = \pi$ a prominent period-4 orbit destabilizes [75, 62, 61]. That classical bifurcations leave visible imprints in the quantum contextuality curve is noteworthy. A plausible explanation is that bifurcations mark transitions in the dominant dynamical behavior [77, 94]. Near these parameter values, a significant fraction of initial conditions shifts from confinement near a stable orbit to escape into the chaotic sea. During this transitional regime, the typical trajectory may spend less time in strongly contextual states, temporarily reducing the violation fraction before chaos fully takes hold. More broadly, the sensitivity of quantum statistics to classical periodic-orbit structure is consistent with scarring and related phenomena [64, 75, 10].

4.3.2 Local signature: phase-space-resolved contextuality

The global signature established that chaotic dynamics generates more contextuality when averaged over many initial conditions, but it does not reveal *where* on the sphere chaos

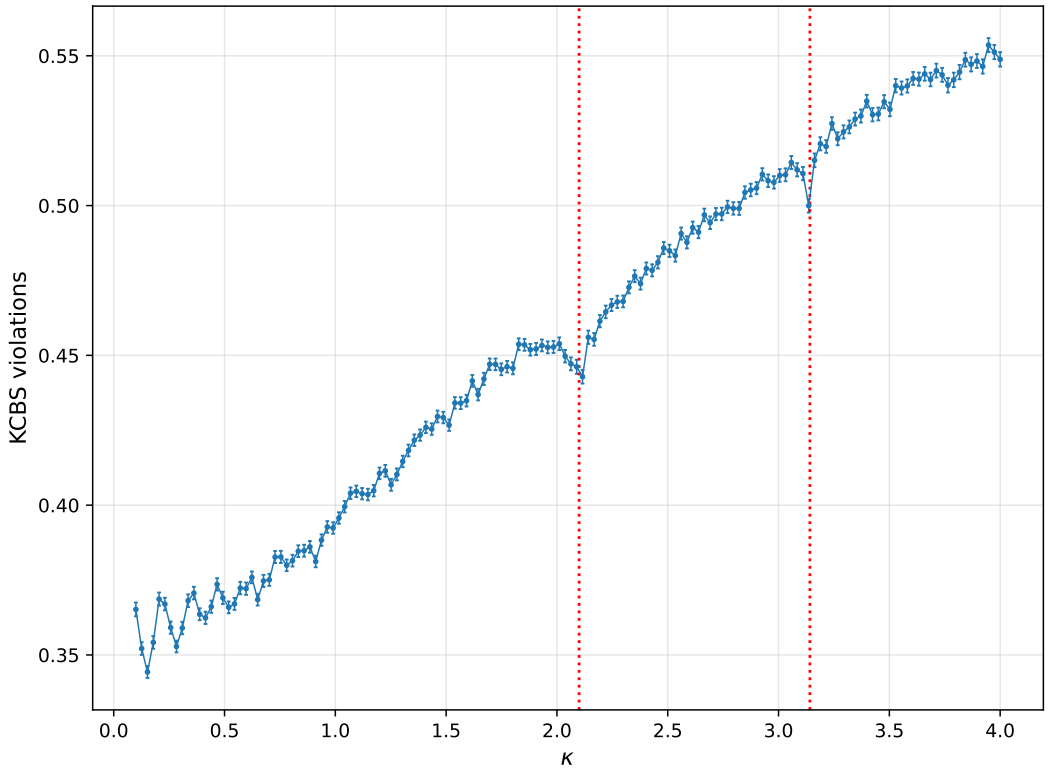


Figure 4.1: Global contextuality signature for the kicked top. For each κ, we sample 1000 Haar-uniform initial coherent states and evolve each for $T = 100$ Floquet steps. The plotted quantity is the fraction of initial conditions exhibiting at least one KCBS violation during evolution. Two localized dips near $\kappa \approx 2$ and $\kappa \approx \pi$ coincide with classical bifurcations where a fixed point and a period-4 orbit lose stability [75].

resides. A local diagnostic should assign each initial coherent state a scalar score that is large in chaotic regions and small in regular islands, thereby recovering the phase-space structure from quantum data alone.

A natural starting point is to use a contextuality-based statistic for each trajectory, mirroring the global approach. However, the time-averaged KCBS violation $\langle \beta'(t) \rangle_t$ fails as a local chaos diagnostic. The problem is that the nonlinear kick can generate contextuality even when the classical orbit does not explore phase space. In particular, coherent states initialized near unstable fixed points remain classically stationary, yet the kick's state-dependent phases rapidly deform them away from the coherent manifold, producing large time-averaged contextuality without any classical chaos. (Section 4.4 discusses this instability-versus-chaos distinction in detail.)

We use the standard deviation of the KCBS violation over time

$$\sigma_K := \mathrm{std}_t\big(\beta'(t)\big). \tag{4.11}$$

This quantity is large when the state repeatedly enters and exits KCBS-violating regimes: a signature of dynamics that samples diverse regions of state space. The standard deviation is preferable to the mean because fixed-point trajectories tend to saturate at a roughly constant value and thus exhibit lower fluctuations. Using σ_K therefore partially mitigates fixed-point artifacts while retaining sensitivity to contextuality.

Two additional corrections are needed to obtain a reliable local diagnostic. The first addresses fixed points directly by weighting the contextuality fluctuations by an independent measure of exploration. A well-established probe is the *survival probability* $R(t) := |\langle \psi_0 | \psi_t \rangle|^2$, which quantifies the overlap between the initial and evolved states [97, 56]. For a state initialized at a fixed point, $R(t) \approx 1$ at all times; for a state in a chaotic region, the evolved state spreads across many basis states and $R(t)$ decays to fluctuate around a small value. We define

$$R_{\mathrm{decay}} := 1 - \langle R(t) \rangle_t, \tag{4.12}$$

which is near zero at fixed points and near unity under chaotic exploration. This quantity is closely related to the fidelity and Loschmidt echo diagnostics used in quantum chaos studies [69, 56, 68, 53].

The second correction addresses a subtlety in small Hilbert spaces. In the $j = 1$ system, even regular (periodic) classical orbits can produce contextuality fluctuations if the quantum state traverses both contextual and noncontextual regions along the orbit. However, such fluctuations typically follow a simple repeating pattern matching the classical period. To distinguish these from the irregular fluctuations of chaotic dynamics, we introduce a

temporal regularity score $\mathrm{reg}_{\mathrm{temp}} \in [0,1]$ that detects short-period repetitions in the sequence of contextuality changes $d_t := |\beta'(t+1) - \beta'(t)|$. The factor $(1 - \mathrm{reg}_{\mathrm{temp}})$ penalizes trajectories with obvious periodic structure.

Combining these three factors yields the hybrid measure

$$K^{(\sigma)}_{\mathrm{hybrid}} := R_{\mathrm{decay}}\, \sigma_K \left(1 - \mathrm{reg}_{\mathrm{temp}}\right). \tag{4.13}$$

The product is large only when all three conditions are satisfied: the state explores phase space (large R_{decay}), exhibits substantial contextuality fluctuations (large σ_K), and does so without obvious periodicity (small $\mathrm{reg}_{\mathrm{temp}}$). Because each factor lies between zero and one, so does $K^{(\sigma)}_{\mathrm{hybrid}}$; values near unity indicate strong chaotic signatures, while values near zero indicate regular or fixed-point behavior.

To generate phase-space maps, we sample 10,000 approximately uniformly distributed initial coherent states (θ, ϕ) on the sphere, evolve each for $T = 100$ Floquet steps, and evaluate $K^{(\sigma)}_{\mathrm{hybrid}}(\theta, \phi)$. For this measure to be a useful signature of chaos, its contour plot should be low and uniform in the integrable regime and should reproduce the regular-island versus chaotic-sea partition when the classical portrait is mixed.

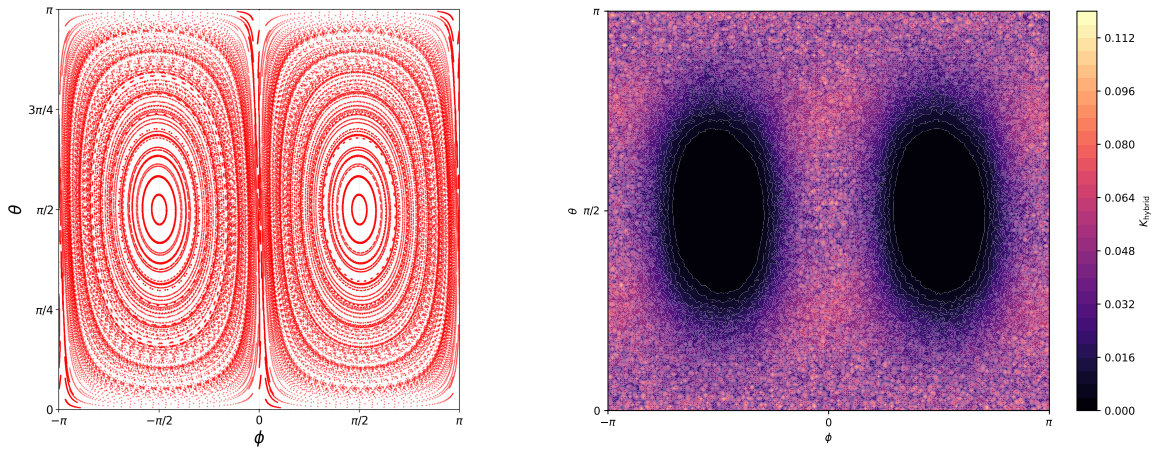


Figure 4.2: Phase-space comparison at $\kappa = 0.1$ (mostly regular). Left: classical stroboscopic portrait. Right: $K^{(\sigma)}_{\mathrm{hybrid}}$ contour.

Figures 4.2 and 4.3 show the contour plots of $K^{(\sigma)}_{\mathrm{hybrid}}$ at two representative kick strengths. At $\kappa = 0.1$ (Fig. 4.2), where classical motion is mostly regular, $K^{(\sigma)}_{\mathrm{hybrid}}$ is uniformly low across the sphere, consistent with confined trajectories that neither explore nor generate

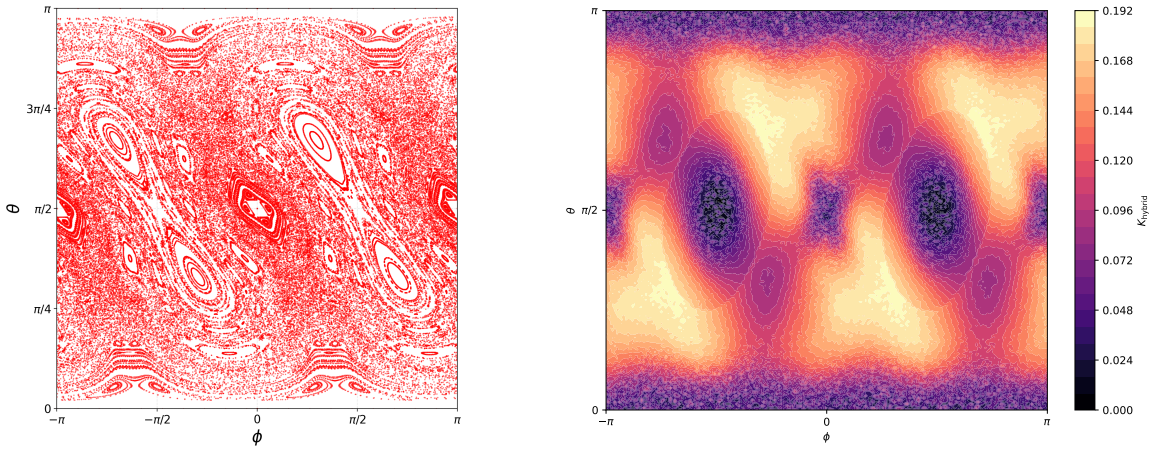


Figure 4.3: Phase-space comparison at $\kappa = 2.5$ (mixed regime). Left: classical portrait with regular islands embedded in a chaotic sea. Right: $K^{(\sigma)}_{\text{hybrid}}$ contour, suppressing fixed-point artifacts and highlighting the chaotic sea.

sustained contextuality fluctuations. At $\kappa = 2.5$ (Fig. 4.3), the classical portrait shows regular islands embedded in a chaotic sea, and the $K^{(\sigma)}_{\text{hybrid}}$ contour mirrors this division: elevated values track the chaotic sea while low values coincide with regular islands.

Since the temporal regularity score already encodes fluctuation structure explicitly, the role originally played by σ_K—distinguishing fixed-point saturation from genuine exploration—is largely absorbed by the $(1 - \text{reg}_{\text{temp}})$ factor. The contextuality component of the metric can therefore be replaced by the time-averaged KCBS violation,

$$\mu_K := \langle \beta'(t) \rangle_t, \tag{4.14}$$

which directly quantifies the typical magnitude of contextuality along a trajectory. The resulting mean-based hybrid measure is

$$K^{(\mu)}_{\text{hybrid}} := R_{\text{decay}}\, \mu_K \left(1 - \text{reg}_{\text{temp}}\right). \tag{4.15}$$

This formulation cleanly separates the three physical ingredients: exploration (R_{decay}), contextuality strength (μ_K), and temporal irregularity ($1 - \text{reg}_{\text{temp}}$), with each factor encoding a distinct aspect of the dynamics.

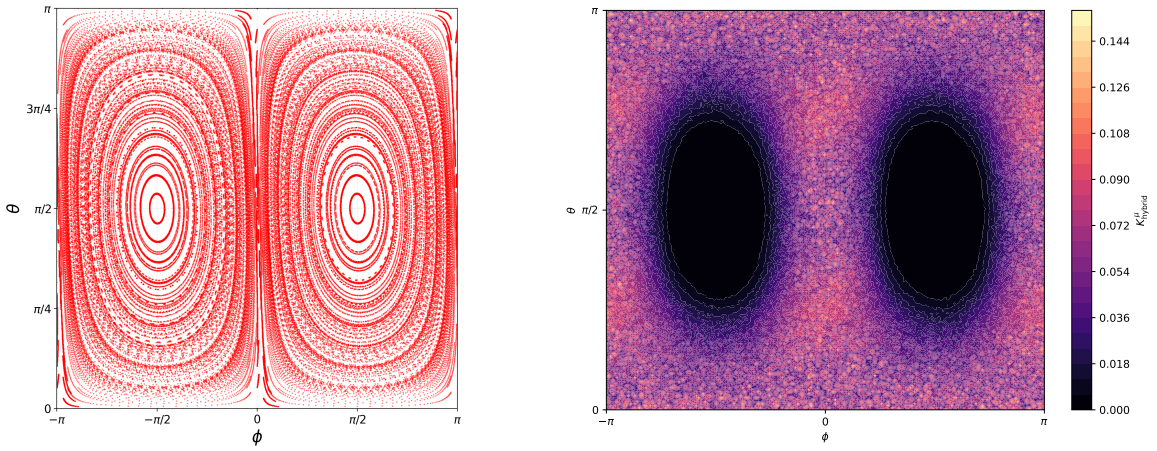


Figure 4.4: Phase-space comparison at $\kappa = 0.1$ (mostly regular). Left: classical stroboscopic portrait. Right: $K^{(\mu)}_{\text{hybrid}}$ contour.

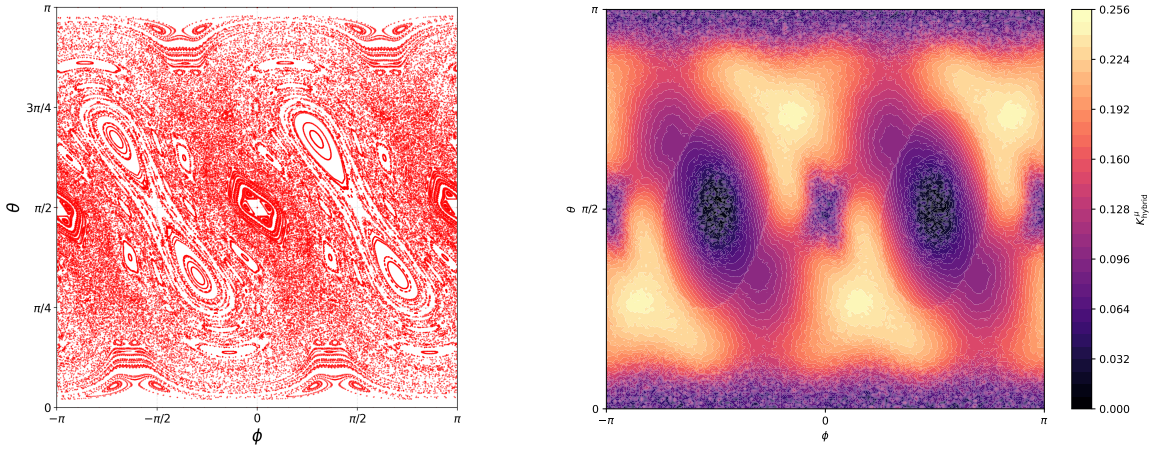


Figure 4.5: Phase-space comparison at $\kappa = 2.5$ (mixed regime). Left: classical portrait with regular islands embedded in a chaotic sea. Right: $K^{(\mu)}_{\text{hybrid}}$ contour, suppressing fixed-point artifacts and highlighting the chaotic sea.

Figures 4.4 and 4.5 show the corresponding contour plots for $K^{(\mu)}_{\text{hybrid}}$. The spatial structure closely tracks that of $K^{(\sigma)}_{\text{hybrid}}$, with comparable value ranges in both the regular and mixed regimes. The regular-island versus chaotic-sea partition is reproduced with equal fidelity, confirming that the temporal regularity factor is the primary mechanism suppressing fixed-point artifacts.

4.4 Discussion: Interpretation and Limitations

The numerical results establish an empirical correlation between KCBS violations and the chaotic-versus-regular structure of the kicked-top classical limit.

Classically regular dynamics confines trajectories to invariant curves or low-period orbits, while chaotic dynamics explores extended regions of the sphere. When the quantum dynamics is initialized in a spin coherent state, regular classical motion tends to preserve approximate phase-space localization (as seen, e.g., in Husimi representations), whereas chaotic motion rapidly produces a delocalized superposition with interference between distinct phase-space components [61, 103, 12, 96]. It is therefore natural that a state-dependent contextuality witness such as KCBS becomes easier to violate once the state departs significantly from the coherent-state manifold and develops strong interference structure.

This mechanism, however, is not identical to classical chaos, and the distinction is important for interpreting local signatures. A large time-averaged KCBS value answers the question "how nonclassical does the unitary make this state?"—not the classical question "does the corresponding point explore a chaotic region?" Classically, a fixed point does not move under the stroboscopic map; the only distinction is whether it is stable or unstable under linearized perturbations. Quantum mechanically, "no classical motion" does not imply "no state change": even at a fixed point the nonlinear kick applies state-dependent phases that can rapidly deform a coherent state and generate sizeable KCBS violations. Plotting raw time-averaged contextuality as a phase-space portrait would therefore show artificial hotspots at unstable periodic points—false positives for chaos. Local instability refers to sensitivity diagnosed by the linearized map (a Lyapunov-type notion), which can be present at unstable periodic orbits even without extended exploration. Chaos in the sense relevant for phase portraits refers to mixing and exploration through large regions of phase space. To obtain a state-resolved measure that aligns with the latter notion, the hybrid statistic K_{hybrid} (in either variant) retains contextuality as the non-classicality ingredient but weights it by an independent exploration proxy (return-probability decay,

closely related to fidelity/Loschmidt-echo measures [97, 69, 56, 68, 53]) and penalizes simple low-period temporal structure.

The local signature K_{hybrid} combines a KCBS-derived statistic with return-probability decay and temporal regularity; in principle, replacing the contextuality component with another state-resolved non-classicality measure that vanishes for coherent states would yield similarly structured phase-space contours. What motivates the choice of KCBS specifically?

First, entanglement-based measures, widely used in composite systems, require imposing an artificial bipartite structure on the spin-1 Hilbert space—for instance, encoding the qutrit into two qubits with a discarded subspace. The KCBS inequality, by contrast, is native to a single three-level system: no embedding, partial trace, or auxiliary subsystem is required.

Second, there is a conceptual alignment between KCBS and the measurement constraints that distinguish quantum from classical descriptions of the kicked top. Diagnosing classical chaos requires tracking stroboscopic trajectories on the unit sphere, which means recording the rescaled spin components $(X, Y, Z) = (J_x/j, J_y/j, J_z/j)$ simultaneously at each time step. Quantum mechanics forbids this: the angular-momentum components do not commute ($[J_x, J_y] = i\hbar J_z$ and cyclic permutations) so no joint measurement of all three exists. The KCBS inequality is constructed precisely around this constraint. It involves only *pairwise* compatible observables—projectors onto spin-0 eigenstates along directions whose adjacent pairs are orthogonal—and asks whether the resulting statistics admit a noncontextual (and hence classical) explanation in which each observable possesses a definite value independent of which compatible partner is measured alongside it. A KCBS violation therefore certifies that no such simultaneous-value assignment exists, directly probing the incompatibility structure that makes classical phase-space trajectories inaccessible. In this sense, KCBS is not merely a convenient witness but one whose logical structure mirrors the measurement obstruction separating quantum dynamics from its classical limit.

Spectral statistics probe the Floquet spectrum globally (Poisson versus Wigner–Dyson level spacings) [25, 61], while Loschmidt echoes and related fidelity measures quantify sensitivity to perturbations and typically exhibit distinct decay regimes that can be analyzed in the kicked-top model itself [97, 56, 53]. Operator scrambling diagnostics, such as out-of-time-ordered correlators, probe the growth of noncommutativity under Heisenberg evolution and can exhibit exponential growth even at small effective system size in kicked-top realizations [84, 99, 9]. By contrast, the KCBS-based approach is explicitly state-resolved and measurement-statistical: it asks whether the evolving state admits a noncontextual explanation for a specific family of compatible measurements. That state-resolved character is what makes the contextuality contours naturally suited to comparisons against

classical phase portraits.

The Kicked-top dynamics and KCBS-style measurements are accessible in platforms that support collective spin control. The kicked top has been realized in cold-atom ensembles (notably cesium) where coherent states can be prepared and phase-space structure reconstructed [36]. KCBS violations have been demonstrated in several platforms, including photonic and solid-state settings [72, 78, 70, 45]. For small effective spins, the same Floquet step can be compiled and implemented digitally, where contextuality statistics can be estimated from repeated preparations and measurements [11, 113].

The present results are obtained in the minimal $j = 1$ setting. This choice makes the KCBS inequality operationally transparent, but it also compresses the available timescales and phase-space resolution: the Hilbert space is only three-dimensional, recurrences are fast, and fine classical structures are not resolvable by coherent-state localization. Moreover, at special parameter values the kicked top's Floquet unitary becomes exactly periodic, returning every state to itself after finitely many kicks regardless of dimension; such exact recurrences obscure quantum–classical correspondence [10].

Finally, the hybrid measure K_{hybrid} is a heuristic construction. It does not constitute a theorem-level correspondence with classical indicators such as Lyapunov exponents. Establishing robustness across parameter space and clarifying which classical invariants (if any) control the resulting contextuality statistics remain open directions.

Chapter 5

Contextuality from the Quantum Vacuum

In quantum field theory the vacuum is the lowest-energy state of the field, but it is not featureless. Even without particles, vacuum correlation functions encode nontrivial structure across spacetime. This structure can be accessed operationally by coupling a localized quantum system to the field for a finite time and then measuring the system. The Unruh–DeWitt detector model [120, 44] provides a standard framework for studying which properties of a quantum field can be imprinted onto localized degrees of freedom. Because any realistic coupling must be switched on and off and spatially localized, the details of switching and smearing have qualitative consequences [116, 108].

Entanglement harvesting illustrates this concretely. Two detectors that never interact directly can become entangled solely through local couplings to a field in its vacuum state. When the interactions are effectively spacelike separated, the resulting correlations cannot be attributed to signalling [121, 105, 102, 119]. This observation has motivated a broader "harvesting" perspective in relativistic quantum information: the field acts as a mediator that can imprint vacuum correlations onto the operational degrees of freedom of localized systems. Other resources studied in this operational approach include mutual information [102], discord [28, 83], nonlocal coherence [126], and steering [133]. Recent work has extended this program to quasiprobability negativity and "magic" [93].

In this chapter we study contextuality as a resource that can be induced in probe systems through vacuum interactions. We test whether purely local detector–field interactions can drive an initially noncontextual pair of detectors into a regime where their accessible measurement statistics become contextual. Contextuality is quantified using the contextual

fraction [3] in a two-qutrit Heisenberg–Weyl measurement scenario. For Heisenberg–Weyl measurements on odd-dimensional systems, contextuality coincides with discrete Wigner-function negativity [59, 67, 122, 42, 115]; see Chapter 6 (Theorem 6.2) for a detailed derivation of this equivalence. This provides a direct conceptual bridge: in the qutrit setting, a contextuality test in the Heisenberg–Weyl scenario simultaneously witnesses the same non-stabilizer (Wigner-negative) resource quantified as "magic" in Ref. [93].

We present numerical evidence that localized interactions with the Minkowski vacuum can produce detector outputs whose Heisenberg–Weyl measurement statistics are contextual. Concretely, we model two initially uncorrelated qutrit Unruh–DeWitt detectors coupled locally to a massless scalar field with Gaussian switching and finite spatial smearing. After tracing out the field, we compute the contextual fraction of the induced two-detector empirical model and track the reduced single-detector state in the discrete Wigner representation. In the parameter regimes explored, contextuality in the bipartite Heisenberg–Weyl statistics turns on precisely when the single-detector Wigner function becomes negative. This provides a dynamical illustration of the contextuality–Wigner correspondence. The use of two qutrits ensures that any violation is genuinely state-dependent in this scenario: for two-qubit systems, the Heisenberg–Weyl measurement scenario yields state-independent contextuality and thus cannot distinguish between states [87, 104]. Any observed contextuality in the qutrit case is therefore created by the interaction rather than built in kinematically. Related analyses of vacuum-induced contextuality have appeared recently; see Ref. [80].

5.1 Physical Setup

The Unruh–DeWitt (UDW) detector model provides a framework for studying the interaction of localized systems with quantum fields [120, 44]. Originally introduced to analyze the Unruh effect, the model has become a standard tool in relativistic quantum information for studying entanglement harvesting, communication through quantum fields, and related phenomena.

We consider a massless real scalar quantum field $\hat{\phi}(x)$ in $(1+3)$-dimensional flat spacetime.[1] The field admits a plane-wave mode expansion

$$\hat{\phi}(x) = \int \frac{d^3\mathbf{k}}{\sqrt{2(2\pi)^3|\mathbf{k}|}} \left(\hat{a}_{\mathbf{k}} e^{-i|\mathbf{k}|t+i\mathbf{k}\cdot\mathbf{x}} + \text{h.c.}\right), \tag{5.1}$$

[1] The generalization to $(1+n)$-dimensional globally hyperbolic curved spacetimes is standard.

where $x = (t, \mathbf{x})$ is a spacetime event and the ladder operators satisfy the canonical commutation relations $[\hat{a}_{\mathbf{k}}, \hat{a}^{\dagger}_{\mathbf{k}'}] = \delta^{(3)}(\mathbf{k} - \mathbf{k}')$. The vacuum state $|0\rangle$ is defined by $\hat{a}_{\mathbf{k}}|0\rangle = 0$ for all $\mathbf{k}$. Throughout this chapter we adopt the mostly-plus signature convention and use units where $c = \hbar = 1$.

The two-point correlation function of the field in the vacuum state is the Wightman function [24]:

$$W(x, x') = \langle 0|\hat{\phi}(x)\hat{\phi}(x')|0\rangle = \int \frac{d^3\mathbf{k}}{2(2\pi)^3|\mathbf{k}|} e^{-i|\mathbf{k}|(t-t')+i\mathbf{k}\cdot(\mathbf{x}-\mathbf{x}')}. \tag{5.2}$$

This function encodes the vacuum correlations that are operationally accessible to localized detectors.

5.1.1 Qutrit detectors

We model each detector as a qutrit—a three-level quantum system with Hilbert space spanned by $\{|0\rangle, |1\rangle, |2\rangle\}$. The free Hamiltonian for detector $i \in \{a, b\}$ is

$$H_{D,i} = \Omega_{i,0}|0\rangle\langle 0|_i + \Omega_{i,1}|1\rangle\langle 1|_i + \Omega_{i,2}|2\rangle\langle 2|_i, \tag{5.3}$$

where $\Omega_{i,j}$ are the energy levels. For simplicity, we take the detectors to be identical and comoving with respect to the quantization frame.

Unlike qubits, whose internal dynamics are fixed, qutrits admit richer internal dynamics (for instance, with or without superselection rules). In this work, we consider two choices of internal dynamics, as prescribed in Ref. [81]:

SU(2) qutrit. The energy levels are equally spaced: $\Omega_0 = 0$, $\Omega_1 = \Omega$, $\Omega_2 = 2\Omega$, where $\Omega > 0$ is the energy gap. The observable coupling to the field is

$$O_{\mathrm{SU}(2)} = |0\rangle\langle 1| + |1\rangle\langle 2| + \mathrm{h.c.} \tag{5.4}$$

This corresponds to the spin-1 representation of SU(2), with a superselection rule forbidding direct transitions between $|0\rangle$ and $|2\rangle$.

Heisenberg–Weyl qutrit. The excited states are degenerate: $\Omega_0 = 0$, $\Omega_1 = \Omega_2 = \Omega$. The coupling observable is

$$O_{\mathrm{HW}} = |0\rangle\langle 1| + |0\rangle\langle 2| + |1\rangle\langle 2| + \mathrm{h.c.} \tag{5.5}$$

This model has no superselection rules and permits transitions between all pairs of levels. In contrast to the SU(2) case, the absence of the superselection rule allows direct $|0\rangle \leftrightarrow |2\rangle$ transitions, and the degeneracy of the excited states ensures that $|1\rangle$ and $|2\rangle$ have equal transition probabilities. As discussed in Section 5.4, these features typically yield a larger contextual fraction for HW dynamics.

The main results presented in this chapter focus on SU(2) internal dynamics. A comparison with Heisenberg–Weyl (HW) internal dynamics is included in Section 5.4 and Appendix B (Section B.1).

5.1.2 Detector-field interaction

In the Dirac picture, the Hamiltonian density capturing the interaction of the two detectors with the quantum field is

$$h_I(x) = \sum_{i\in\{a,b\}} \lambda_i \Lambda_i(x) O_i(t) \otimes \hat{\phi}(x), \tag{5.6}$$

where λ_i is the coupling constant between detector i and the field, $\Lambda_i(x)$ is a spacetime smearing function controlling where detector i interacts locally with the field, and $O_i(t) = e^{iH_{D,i}t} O_i e^{-iH_{D,i}t}$ is the detector observable in the interaction picture.

We take the detectors to be identical with $\lambda_a = \lambda_b =: \lambda$ and to be comoving with respect to the field quantization frame. Detector a is centered at the spatial origin, and detector b is separated by distance d along one spatial axis.

The spacetime smearing factorizes as $\Lambda_i(x) = \chi_i(t) F_i(\mathbf{x})$, where:

- The *switching function* $\chi_i(t) = \exp(-t^2/T^2)$ controls the temporal profile of the interaction, with T setting the effective interaction duration.
- The *spatial smearing* $F_i(\mathbf{x}) = \frac{3}{4\pi R^3}\Theta(R - |\mathbf{x} - \mathbf{x}_i|)$ represents a spherical detector of radius R centered at position $\mathbf{x}_i$, where Θ is the Heaviside step function.

Initializing the detectors in an uncorrelated state and the field in its vacuum state $|0\rangle$ at $t \to -\infty$, the final state is evaluated at $t \to +\infty$. The time evolution operator is

$$U = \mathcal{T}_t \exp\left[-i \int d^4x \, h_I(x)\right], \tag{5.7}$$

where $\mathcal{T}_t$ denotes time ordering with respect to t. For small coupling λ, we expand in a Dyson series:

$$U = \mathbb{1} + U^{(1)} + U^{(2)} + O(\lambda^3), \tag{5.8}$$

where $U^{(j)}$ is the j-th order correction in λ.

We initialize the detectors in the product ground state $\rho_d^{(0)} = |0\rangle\langle 0|_a \otimes |0\rangle\langle 0|_b$ and the field in the Minkowski vacuum. Since the vacuum is a Gaussian state, all odd-point correlation functions vanish, and the final detector state (after tracing out the field) is

$$\rho_d = \mathrm{tr}_\phi \left(U \rho^{(0)} U^\dagger \right) = \rho_d^{(0)} + \rho_d^{(2)} + O(\lambda^4). \tag{5.9}$$

To write the final state of the detectors, we define the following integrals:

$$L_{ij} = \lambda^2 \int d^4x\, d^4x'\, \Lambda_i(x) \Lambda_j(x') e^{-i\Omega(t-t')} W(x,x'), \tag{5.10}$$

$$Q_i = -\frac{\lambda^2}{2} \int d^4x\, d^4x'\, \Lambda_i(x) \Lambda_i(x') e^{i\Omega(t+t')} G_F(x,x'), \tag{5.11}$$

$$M_{ab} = -\lambda^2 \int d^4x\, d^4x'\, \Lambda_a(x) \Lambda_b(x') e^{i\Omega(t+t')} G_F(x,x'), \tag{5.12}$$

where

$$W(x,x') = \langle 0|\hat{\phi}(x)\hat{\phi}(x')|0\rangle, \tag{5.13}$$

$$G_F(x,x') = \Theta(t-t')W(x,x') + \Theta(t'-t)W(x',x), \tag{5.14}$$

are the Wightman function and the Feynman propagator, respectively. Given that we consider identical detectors, we write $L := L_{aa} = L_{bb}$ and $Q := Q_a = Q_b$.

For Heisenberg–Weyl (HW) internal dynamics, an additional integral appears:

$$V = -\lambda^2 \int d^4x\, d^4x'\, \Lambda_i(x) \Lambda_i(x') e^{i\Omega t'} \Theta(t-t') W(x,x'). \tag{5.15}$$

This term arises because HW dynamics permits direct $|0\rangle \leftrightarrow |1\rangle$ and $|0\rangle \leftrightarrow |2\rangle$ transitions (unlike SU(2), where only nearest-neighbor transitions occur). For identical detectors, $V := V_a = V_b$.

For SU(2) detectors, the final two-detector state at order $O(\lambda^2)$ only populates the ground sector and the sectors where at most one detector is excited, together with vacuum-induced coherences between $|00\rangle$ and states in which one detector has undergone the two-step transition to $|2\rangle$. In the ordered product basis $\{|00\rangle, |01\rangle, |02\rangle, |10\rangle, |11\rangle, |12\rangle, |20\rangle, |21\rangle, |22\rangle\}$,

we write

$$\rho_d = \begin{pmatrix} 1-2L & 0 & Q^* & 0 & M_{ab}^* & 0 & Q^* & 0 & 0 \\ 0 & L & 0 & L_{ab} & 0 & 0 & 0 & 0 & 0 \\ Q & 0 & 0 & 0 & 0 & 0 & 0 & 0 & 0 \\ 0 & L_{ab} & 0 & L & 0 & 0 & 0 & 0 & 0 \\ M_{ab} & 0 & 0 & 0 & 0 & 0 & 0 & 0 & 0 \\ 0 & 0 & 0 & 0 & 0 & 0 & 0 & 0 & 0 \\ Q & 0 & 0 & 0 & 0 & 0 & 0 & 0 & 0 \\ 0 & 0 & 0 & 0 & 0 & 0 & 0 & 0 & 0 \\ 0 & 0 & 0 & 0 & 0 & 0 & 0 & 0 & 0 \end{pmatrix} + O(\lambda^4), \tag{5.16}$$

where L_{ab} is real. We emphasize that this explicit matrix form depends on the chosen basis ordering; the physically relevant content is the identification of the leading-order nonzero matrix elements (L, L_{ab}, Q, and M_{ab}). The physical interpretation of these matrix elements is as follows:

- L is a *local noise/excitation* term: it controls the probability that a single detector is promoted out of $|0\rangle$.
- L_{ab} is the corresponding *nonlocal* excitation term generated by vacuum correlations across the two detector worldtubes.
- Q is a *local coherence* term that, in the reduced single-detector state, couples $|0\rangle$ and $|2\rangle$ at $O(\lambda^2)$ (a two-step process under SU(2) selection rules). It is this coherence that drives the Wigner-negativity conditions in Eqs. (5.26)–(5.28).
- M_{ab} is a *nonlocal coherence* term, responsible for the leading-order off-diagonal correlations between the detectors.

Although the Gaussian switching function is not compactly supported (the detectors are never strictly off), we can define an intuitive criterion for effective spacelike separation. The criterion relies on the observation that, for a Gaussian switching function centered at $t = 0$, most of its weight is concentrated in the interval $[-NT/(2\sqrt{2}), NT/(2\sqrt{2})]$, where $T/\sqrt{2}$ is the standard deviation of the Gaussian switching and $N \geq 2$.

This observation allows us to treat the interaction of each detector as having an effective finite duration of $NT/\sqrt{2}$, resulting in the criterion:

$$d \geq 2R + \frac{NT}{\sqrt{2}}. \tag{5.17}$$

For near-pointlike detectors, this criterion reduces to $d \geq NT/\sqrt{2}$, as more frequently seen in the literature. However, since we also explore large detector regimes where the radius is comparable to the interaction time, R must be taken into account.

The least stringent case used corresponds to $N = 5$, for which over 98% of the switching's weight lies within $\pm 5T/(2\sqrt{2})$ from its peak. Our numerical results also use $N = 7$ (as frequently used in the literature [102]), as well as $N = 10$ and $N = 14$ to explore increasingly stringent spacelike separation.

5.2 Contextuality and Wigner-Negativity Diagnostics

We evaluate the detector output in a fixed two-qutrit Heisenberg–Weyl measurement scenario and quantify contextuality using the contextual fraction (Chapter 2, Sections 2.2.2–2.3.1). In parallel, we track single-detector non-stabilizerness via the Gross discrete Wigner sum-negativity (Chapter 2, Section 2.4). The structural link between these diagnostics in odd local dimension is detailed in Chapter 6 (Theorem 6.2). Accordingly, we keep the present section purely as a record of the conventions and the concrete formulas used in the numerical pipeline.

5.2.1 Two-qutrit Heisenberg–Weyl measurement scenario

We use the two-qutrit Heisenberg–Weyl (Pauli) measurement scenario developed in Chapter 6 (Sections 6.2–6.3); the reader may refer there for the full construction. For convenience we summarize the notation used in this chapter.

For a single qutrit the clock and shift operators are [57]

$$Z = \sum_{j=0}^{2} \omega^j |j\rangle\langle j|, \qquad X = \sum_{j=0}^{2} |j+1 \bmod 3\rangle\langle j|, \tag{5.18}$$

where $\omega = e^{2\pi i/3}$. We label Heisenberg–Weyl operators by phase-space vectors $v = [p, q] \in \mathbb{Z}_3^2$ and use the Gross/Wootters phase convention

$$W(v) = W([p, q]) = \omega^{2^{-1}pq} X^p Z^q. \tag{5.19}$$

For two qutrits we write $v = [p_1, q_1, p_2, q_2] \in \mathbb{Z}_3^4$ and define

$$W(v) = W([p_1, q_1]) \otimes W([p_2, q_2]). \tag{5.20}$$

Although the Heisenberg–Weyl operators are non-Hermitian, we treat them as observables in the standard spectral sense: each unitary $W(v)$ is measured via its projection-valued measure (its eigenprojectors), with outcomes labelled by $k \in \mathbb{Z}_3$ corresponding to eigenvalues ω^k. Two operators commute iff their symplectic product vanishes (mod 3) [66]:

$$[v, v'] := p_1 q_1' - q_1 p_1' + p_2 q_2' - q_2 p_2' \equiv 0 \pmod 3. \tag{5.21}$$

A *context* is a maximal commuting set (equivalently, a Lagrangian subspace of $\mathbb{Z}_3^4$); see Chapter 6 for details. In the two-qutrit case there are 40 contexts, each containing 9 commuting operators (including the identity).

We quantify contextuality using the *contextual fraction* (CF) from Chapter 2 (Section 2.3), computed via the linear program in Eq. (2.19). In the present Heisenberg–Weyl scenario, the deterministic noncontextual assignments are restricted by the Weyl algebra: by Lemma 6.4 (see Chapter 6), any such assignment is linear,

$$\lambda(W(v)) = \lambda \cdot v \pmod 3 \tag{5.22}$$

for some $\lambda \in \mathbb{Z}_3^4$. Hence there are only $3^4 = 81$ deterministic assignments, keeping the LP tractable.

Given a detector state ρ_d, we form the empirical model by computing the joint outcome distributions for each context. For a context C and a joint outcome label r, the corresponding stabilizer projector can be written as

$$\Pi_C^r = \frac{1}{9} \sum_{W \in C} \omega^{-r(W)} W, \tag{5.23}$$

where $r \in \mathbb{Z}_3^9$ records the eigenvalue labels for the operators in C. The outcome probabilities are then

$$p_C(r) = \mathrm{Tr}[\Pi_C^r \rho_d]. \tag{5.24}$$

The contextual fraction $\mathrm{CF}(\rho_d)$ is obtained by solving Eq. (2.19) with these probabilities as input; in practice we use `scipy.optimize.linprog` [124].

In addition to $\mathrm{CF}(\rho_d)$, we compute the Wigner sum-negativity $\mathcal{N}(\rho_a)$ of the reduced single-detector state as a compact diagnostic of whether the interaction has produced a non-stabilizer output state. For the SU(2) detector dynamics considered in the main text, ρ_a depends only on the coefficients L and Q, so Wigner negativity reduces to a small set of explicit inequalities.

For the SU(2) detector model, tracing out detector b gives $\rho_a = \mathrm{Tr}_b[\rho_d]$. From Eq. (5.16) the reduced state is

$$\rho_a = \begin{pmatrix} 1-L & 0 & Q^* \\ 0 & L & 0 \\ Q & 0 & 0 \end{pmatrix}. \tag{5.25}$$

We quantify single-detector "magic" by the Wigner sum-negativity $\mathcal{N}(\rho_a)$ [122]. For odd prime local dimension (including the qutrit case $d = 3$), Wigner negativity is equivalent to lying outside the stabilizer polytope [59, 122]; accordingly, sum-negativity—which is monotonically related to the mana of Ref. [123]—serves as a magic monotone for odd-dimensional systems. For the Gross discrete Wigner function in $d = 3$, only three phase-space values can become negative for states of the form (5.25). Up to a factor of 1/3, the potentially negative expressions are

$$L + 2\mathrm{Re}[Q], \tag{5.26}$$

$$L - \mathrm{Re}[Q] + \sqrt{3}\,\mathrm{Im}[Q], \tag{5.27}$$

$$L - \mathrm{Re}[Q] - \sqrt{3}\,\mathrm{Im}[Q]. \tag{5.28}$$

In the parameter regimes explored in Section 5.3, only (5.26) and (5.28) become negative.

5.3 Results: Contextuality Induced by Vacuum Interactions

We now present the main numerical results demonstrating contextuality in the detector outputs induced by local vacuum interactions. Unless otherwise stated, simulations use SU(2) qutrit dynamics with coupling constant $\lambda = 10^{-3}$, safely within the perturbative regime where $\mathrm{CF}(\rho_d)/\lambda^2$ is constant. Results for Heisenberg–Weyl (HW) internal dynamics are summarized in Section 5.4 and presented in detail in Appendix B (Section B.1).

We report contextuality via the contextual fraction $\mathrm{CF}(\rho_d)$ in the two-qutrit Heisenberg–Weyl measurement scenario, and in parallel track single-detector non-stabilizerness via the Wigner sum-negativity $\mathcal{N}(\rho_a)$. In the qutrit setting these diagnostics are expected to switch on in the same parameter regimes (Theorem 6.2), and we use their agreement as a consistency check.

5.3.1 Energy-gap dependence

We first fix the switching duration T and study the dependence on the dimensionless detector gap ΩT. To separate genuinely bipartite effects from single-detector magic, we compare three families of states:

- The full two-detector state ρ_{ab} for separations satisfying the effective spacelike criterion (5.17), using $N \in \{5, 7, 10, 14\}$.
- The product of reduced single-detector states $\rho_a \otimes \rho_b$, which is the asymptotic limit at large separation.
- The single-detector baseline $\rho_a \otimes |0\rangle\langle 0|$, where only one detector interacts with the field.

Contextual fraction. Figures 5.1 and 5.2 show $\mathrm{CF}(\rho_d)/\lambda^2$ as a function of ΩT for two detector sizes: $R/T = 1$ (large detectors) and $R/T = 0.1$ (near the pointlike limit).

Across both detector sizes, we observe four robust trends:

(i) $\mathrm{CF}(\rho_d)$ is non-monotonic in ΩT, peaking at intermediate gap.

(ii) Smaller detectors yield substantially larger CF.

(iii) The two-detector protocol outperforms the single-detector baseline $\rho_a \otimes |0\rangle\langle 0|$.

(iv) Increasing separation reduces $\mathrm{CF}(\rho_d)$ toward the product-state value, with a more pronounced decay for large detectors.

Wigner negativity. Figures 5.3 and 5.4 show the reduced single-detector sum-negativity $\mathcal{N}(\rho_a)/\lambda^2$ for the same parameter choices.

The onset and decay of $\mathcal{N}(\rho_a)$ across ΩT closely matches the behavior of $\mathrm{CF}(\rho_d)$ in Figures 5.1–5.2, consistent with the contextuality–Wigner correspondence for Heisenberg–Weyl measurements in odd local dimension.

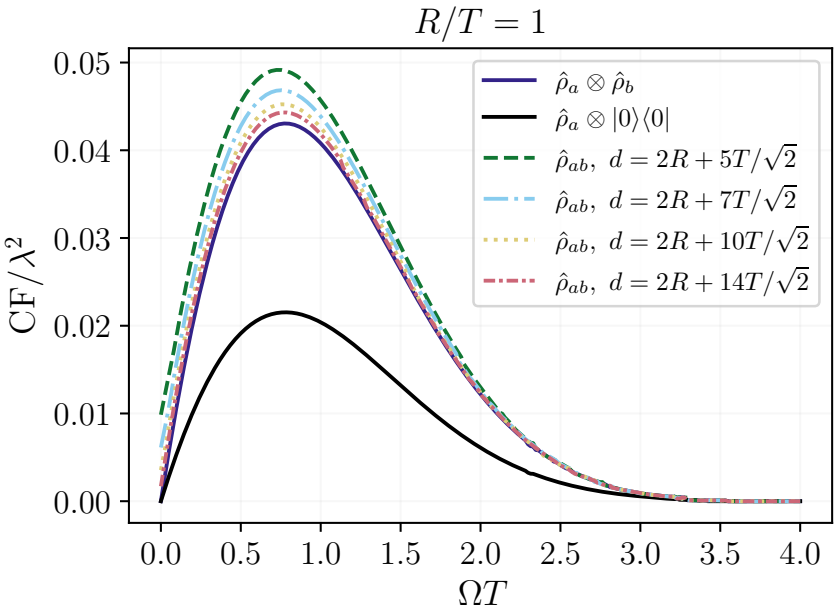


Figure 5.1: Contextual fraction normalized by λ^2 for large detectors ($R/T = 1$) as a function of ΩT. Different curves correspond to different detector separations satisfying the spacelike criterion.

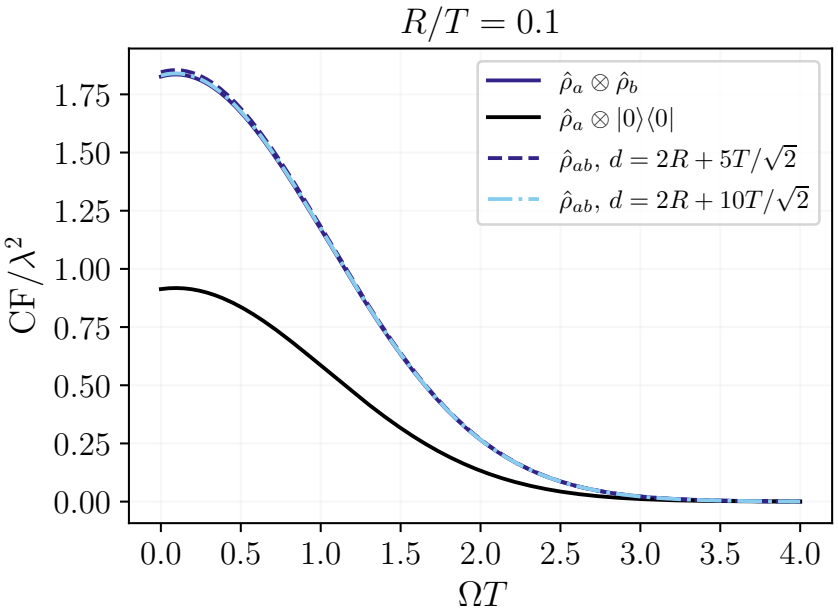


Figure 5.2: Contextual fraction normalized by λ^2 for small detectors ($R/T = 0.1$) approaching the pointlike limit.

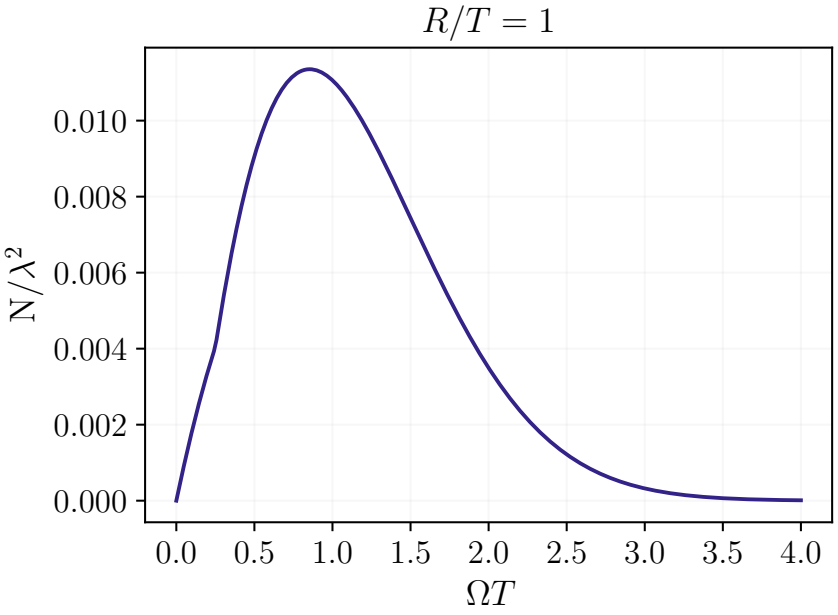


Figure 5.3: Wigner negativity (sum-negativity) normalized by λ^2 for large detectors ($R/T = 1$).

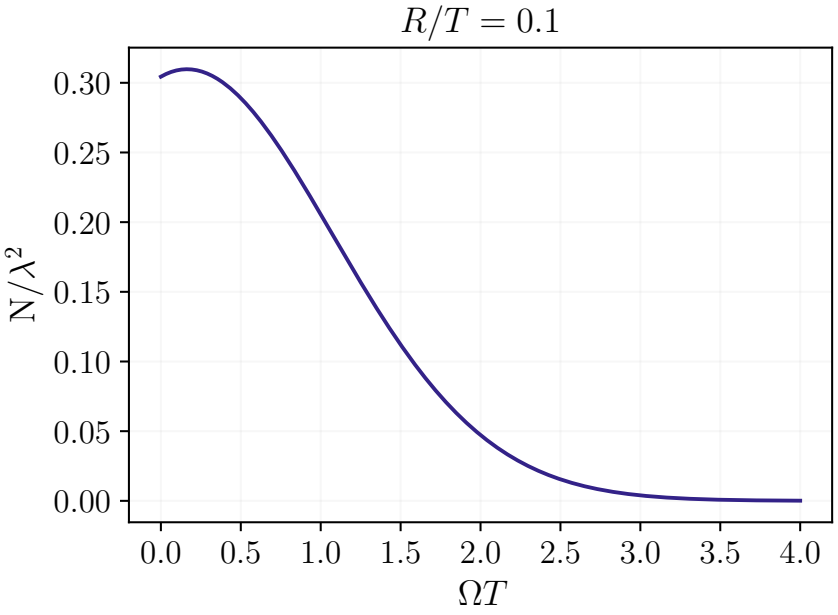


Figure 5.4: Wigner negativity (sum-negativity) normalized by λ^2 for small detectors ($R/T = 0.1$).

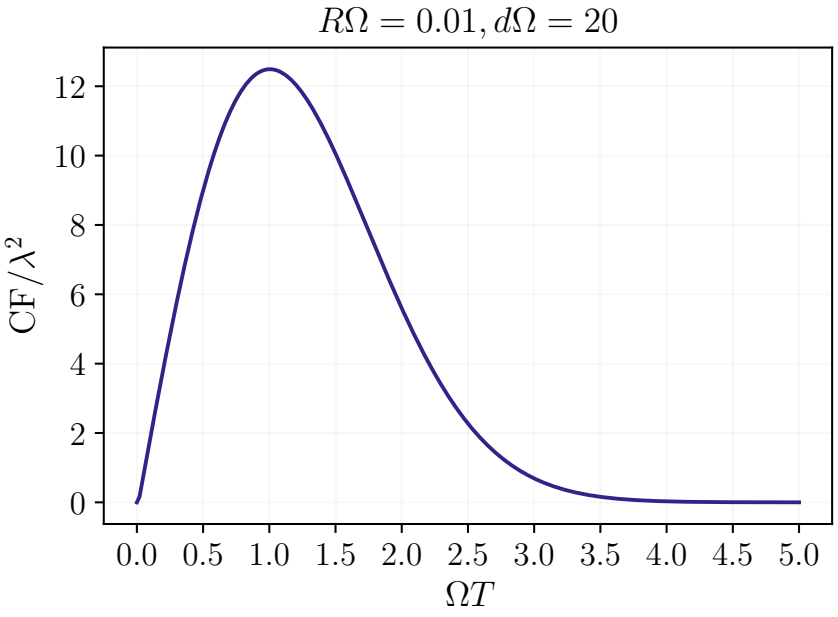


Figure 5.5: Contextual fraction normalized by λ^2 for small detectors ($R/T = 0.1$) as a function of ΩT obtained by varying the switching duration T (with other parameters fixed as in the corresponding numerical setup).

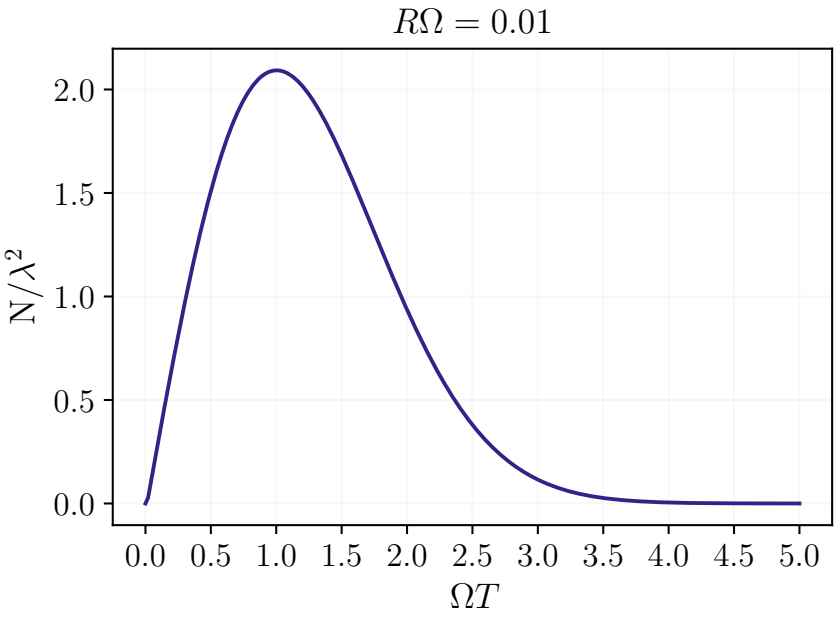


Figure 5.6: Wigner sum-negativity normalized by λ^2 for the reduced single-detector state for the same small-detector switching-variation setup as Figure 5.5.

5.3.2 Switching-duration dependence

The same tradeoff can be displayed by fixing the detector gap Ω and varying the switching duration T. Figures 5.5 and 5.6 show, for small detectors, $\mathrm{CF}(\rho_d)/\lambda^2$ and $\mathcal{N}(\rho_a)/\lambda^2$ as functions of ΩT obtained by varying T.

As in the gap scan, the contextual fraction and Wigner negativity switch on and off together across ΩT.

5.3.3 Scaling with coupling strength

The perturbative expansion predicts that all leading-order contributions to the detector state scale as λ^2, and thus that $\mathrm{CF}(\rho_d)$ and $\mathcal{N}(\rho_a)$ should be proportional to λ^2 throughout the regime where the truncation at $O(\lambda^2)$ is valid. Numerically, we checked this by evaluating $\mathrm{CF}(\rho_d)/\lambda^2$ for $\lambda \in [10^{-4}, 10^{-2}]$ and found no resolvable dependence on λ. For $\lambda \gtrsim 10^{-2}$, higher-order corrections become visible. For $\lambda \lesssim 10^{-4}$, floating-point precision limits dominate. Accordingly, we fix $\lambda = 10^{-3}$ in all plots.

5.4 Discussion: Mechanism and Parameter Dependence

Section 5.3 showed that local detector–field interactions can move the detectors across a noncontextuality boundary. In the two-qutrit Heisenberg–Weyl scenario, this transition has two equivalent signatures: contextuality in the bipartite measurement statistics and Wigner-function negativity in the single-detector marginals. This section distills the physical interpretation and recasts the observed parameter trends as consequences of how the vacuum imprints local excitation noise and coherence onto the detectors.

The quantum vacuum is not a featureless background: it is a structured state with correlations that can be accessed by localized probes. Entanglement-harvesting protocols make this operationally concrete for entanglement [105, 102], and recent "magic harvesting" protocols extend the same perspective to Wigner negativity [93]. The present results add contextuality to this picture. Because contextuality is defined relative to a measurement scenario, vacuum-induced contextuality is not merely "entanglement from the vacuum" under a different name; rather, it marks a transition in the classical simulability of the detectors' Heisenberg–Weyl measurement statistics. In practice this matters because a

single experimental measurement framework—joint Heisenberg–Weyl measurements on the two detectors—diagnoses both the appearance of contextuality in the bipartite statistics and, in the regimes studied here, the onset of Wigner negativity in the single-detector marginals.

The observed coincidence of these diagnostics is exactly what one expects from the structural results of Chapter 6: for odd local dimension, noncontextuality in the Heisenberg–Weyl scenario is equivalent to positivity of the Gross discrete Wigner function. The present chapter provides a dynamical illustration of that equivalence. Starting from an initially noncontextual product state (CF $= 0$ and $\mathcal{N} = 0$), the vacuum interaction generates coherences (notably the Q-type terms in Eq. (5.16)) that can drive the reduced single-detector Wigner function negative, and the contextual fraction of the induced two-detector empirical model switches on in the same parameter regions.

This behavior can be read directly from the perturbative structure of the reduced detector state. For SU(2) dynamics, each single-detector marginal is controlled (to leading order) by a local excitation/noise scale L and a single local coherence parameter Q (Eq. (5.25)). Wigner negativity appears precisely when coherence is sufficiently large compared to excitation/noise, i.e., when one of the inequalities in Eqs. (5.26)–(5.28) becomes negative. On the bipartite side, the nonlocal coefficients L_{ab} and M_{ab} encode how vacuum correlations link the two detector worldtubes and control deviations from the product limit $\rho_a \otimes \rho_b$. Accordingly, the numerical "sweet spots" in Section 5.3 are regimes in which the vacuum efficiently generates coherence (driving negativity and hence contextuality) without overwhelming it by local excitation noise.

The non-monotonic dependence on the dimensionless gap ΩT in Figures 5.1–5.4 is a direct expression of this coherence–noise balance. The behavior can be traced to the uncertainty principle. The integrals in Eqs. (5.10)–(5.12) involve Fourier transforms of the Gaussian switching functions with respect to time differences. A Gaussian of variance $\propto T$ in time becomes a Gaussian of variance $\propto 1/T$ in frequency. Consequently, very long interactions ($\Omega T \to \infty$) correspond to a narrow frequency window and suppress all $O(\lambda^2)$ transition amplitudes exponentially [24, 116, 108]. Very short interactions open a broad frequency window that increases excitation noise alongside coherence. The peak at intermediate ΩT occurs where the coherence-to-noise ratio is most favorable for violating the Wigner-positivity inequalities. Varying the switching duration T at fixed gap Ω (Figures 5.5 and 5.6) displays the same tradeoff from the complementary perspective of changing the effective spectral width of the interaction.

Detector size and separation affect the same balance through the field's short-distance structure. Decreasing R/T strengthens both CF and $\mathcal{N}$ because spatial smearing averages

over short-wavelength fluctuations and suppresses the high-frequency contributions that most efficiently generate the coherences responsible for Wigner negativity. Increasing the detector separation reduces the nonlocal coefficients L_{ab} and M_{ab}, pushing the output toward $\rho_a \otimes \rho_b$ and lowering the contextual fraction; the numerics show this decay with separation is more pronounced for large detectors, consistent with additional suppression from spatial averaging.

The scaling test in Section 5.3.3 supports the perturbative expectation that both diagnostics scale as λ^2 throughout the range where truncation at $O(\lambda^2)$ is valid. This justifies presenting results normalized by λ^2 and interpreting the remaining variation as genuine dependence on ΩT, R/T, and separation.

A potentially counterintuitive feature is that contextuality can persist in the gapless limit $\Omega = 0$, most prominently for small detectors. In this chapter we keep R/T fixed, so $\Omega T \to 0$ corresponds to sending $\Omega \to 0$ at finite interaction time. The coefficients controlling coherence and excitation (L, Q) approach nontrivial R/T-dependent limits, and the Wigner-positivity inequalities (5.26)–(5.28) can still be violated. By contrast, conventions that fix $R\Omega$ (so that $\Omega T \to 0$ implies $T \to 0$) correspond to switching the interaction off: all $O(\lambda^2)$ contributions vanish, and hence both CF and $\mathcal{N}$ vanish at $\Omega T = 0$. This difference in which ratios are held fixed accounts for apparent contrasts with other vacuum-harvesting settings, e.g., the absence of spacelike entanglement harvesting for inertial Gaussian-switched gapless detectors [101]. Entanglement and contextuality arise from different mechanisms: negativity (entanglement) depends on the competition between L and $|M_{ab}|$, whereas contextuality follows the Wigner inequalities in Eqs. (5.26)–(5.28).

The detector's internal dynamics determines which transition pathways couple to the field and, consequently, which coherences arise at leading order. For SU(2) dynamics, the selection rule forbidding direct $|0\rangle \leftrightarrow |2\rangle$ transitions forces the relevant coherence to arise through a two-step process, yielding the sparse reduced state in Eq. (5.25). For Heisenberg–Weyl (HW) dynamics, the coupling permits all pairwise transitions and the excited states are degenerate, so additional coherences appear already at $O(\lambda^2)$ and the reduced state takes the richer form in Eq. (B.3). Figure 5.7 compares the single-detector Wigner sum-negativity (normalized by λ^2) produced by SU(2) and HW qutrit detectors in a representative small-detector regime; HW dynamics typically produces larger negativity across the same range of ΩT, consistent with the fact that removing the SU(2) superselection rule and introducing degeneracy in the excited manifold increases the relative weight of coherence compared to local excitation noise.

Finally, to make the SU(2)–HW contrast explicit at the level of the reduced state, HW

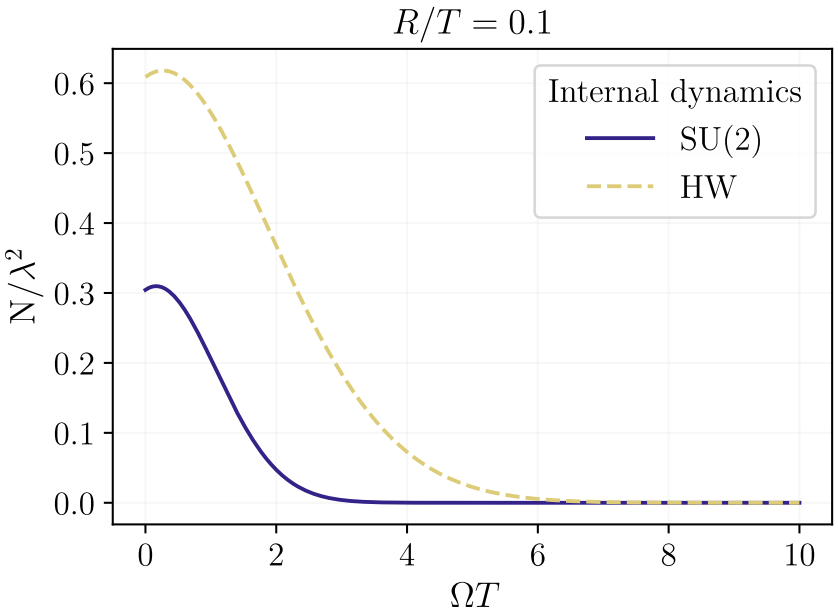


Figure 5.7: Comparison of Wigner sum-negativity (normalized by λ^2) produced by SU(2) and Heisenberg–Weyl internal detector dynamics, illustrating the enhanced coherence generation in the HW model.

dynamics yields

$$\rho_a = \begin{pmatrix} 1-2L & V^* & V^* \\ V & L & L \\ V & L & L \end{pmatrix}, \tag{5.29}$$

with V defined in Eq. (B.1). The larger set of coherences present already at leading order provides a compact explanation for the higher Wigner negativity (and hence higher contextuality) typically observed for HW detectors.

A natural foundational question, paralleling entanglement harvesting, is whether the contextuality observed in the detector outputs should be regarded as genuinely extracted from the field. For entanglement, effective spacelike separation rules out communication and supports attributing detector entanglement to the field state [119]: the detectors do not interact directly with each other and couple only locally to the field, so any entanglement shared between them must be field-mediated. For contextuality, an analogous implication about the field state is not currently available. Determining how strongly $\mathrm{CF}(\rho_d)$ depends on the field state, and whether field-independent local processing can increase contextuality in the scenarios considered here, would clarify the interpretation; we leave these questions for future work.

Chapter 6

Logical Bell Inequalities for Witnessing Marginal Wigner Negativity

6.1 Introduction and Motivation

This chapter links contextuality with the discrete Wigner representation. We build a family of multi-qudit inequalities that can be evaluated from single-qudit measurement statistics, but whose violation certifies that the reduced state of that qudit has a negative discrete Wigner value at a chosen phase-space point. Contextuality is the failure of any deterministic noncontextual value assignment: one cannot preassign an outcome to every observable so that (i) each observable has a value that is independent of the commuting observables measured alongside it, and (ii) whenever observables commute, the assigned values satisfy the same algebraic (functional) relations as the operators [73, 21]. See Section 2.2.1 and Section 2.2.2 for the general framework. The discrete Wigner function [130, 55] maps a qudit state to a real-valued quasiprobability distribution on a finite phase space; negativity shows that this function cannot be treated as an ordinary probability distribution. See Section 2.4 and Section 2.4.2 for definitions and conventions.

We work with qudits (d-level generalization of qubits) in odd prime local dimension d. This choice is made because odd-dimensional systems admit a particularly well-behaved version of the discrete Wigner formalism: stabilizer states have nonnegative Wigner functions, Clifford unitaries act as affine symplectic transformations of phase space, and for pure

states Wigner-nonnegativity exactly characterizes the stabilizer states [59]. In even dimensions one can still define quasiprobability representations, but the fully Clifford-covariant, stabilizer-positive picture is obstructed and the story is necessarily more subtle [136].

The relevance of Wigner nonnegativity is that it enables efficient classical simulation of stabilizer circuits [57, 1, 122]. If every intermediate state in a computation admits a nonnegative Wigner representation, the Wigner function behaves like an ordinary probability distribution over phase space: Clifford gates act by permutations (affine symplectic maps) and Weyl measurements correspond to coarse-grainings (line sums), yielding an efficient sampling-based simulation protocol [59, 122, 95]. Universal quantum computation requires resources beyond this simulable regime. In the magic-state model, one supplements Clifford operations with suitably chosen non-stabilizer ancillas to implement non-Clifford gates and achieve universality [27]; Wigner negativity is a quantitative measure for this extra resource, and simulation overheads can be bounded in terms of negativity measures such as the Wigner ℓ_1-norm (mana) [123, 95].

Contextuality provides a complementary, constraint-based way to certify the same boundary. Howard *et al.* identified contextuality as the key obstruction to simulating magic-state computation in odd dimensions [67]. For multi-qudit systems ($n \geq 2$) contextuality with respect to Weyl (generalized Pauli) measurements occurs exactly when the full n-qudit discrete Wigner function is negative somewhere [42]. We construct a family of logical Bell inequalities for two qudits in odd prime local dimension, following the framework of Abramsky and Hardy [5]. We show that the inequality is violated if and only if the reduced state of the first qudit has a negative discrete Wigner value at the chosen phase-space point.

The chapter proceeds as follows. Section 6.2 sets notation for the Heisenberg–Weyl (generalized Pauli) group. Section 6.3 characterises the two-qudit measurement contexts. Section 6.4 constructs the marginal logical Bell witness and states the equivalence with marginal Wigner negativity. Section 6.5 proves the main theorem. Section 6.6 connects the witness to the contextual fraction. Sections 6.7 and 6.8 discuss extensions and implications.

6.2 Heisenberg–Weyl Group

We establish notation for Weyl operators, following Refs. [130, 55, 59, 66].

In odd prime dimension d, the operator set generated by the shift and phase operators X and Z is also known as the Heisenberg–Weyl group or the generalized Pauli group.

When discussing measurement *observables* we always ignore physically irrelevant global phases, i.e., we work with the corresponding projective (phase-free) Weyl/Pauli operators.

Conventions: Let d be an odd prime. Arithmetic on indices and phase-space coordinates is performed modulo d unless otherwise noted. Measurement outcomes for Weyl observables are labeled by the exponent $a \in \mathbb{Z}_d$ of the eigenvalue ω^a, where $\omega = e^{2\pi i/d}$.

The Heisenberg–Weyl group is the odd-prime-dimensional generalization of the usual (qubit) Pauli group. We define the single-qudit generalized Pauli generators by their action on the computational basis $\{|j\rangle\}_{j\in\mathbb{Z}_d}$:

$$X|j\rangle = |j+1\rangle \quad \text{and} \quad Z|j\rangle = \omega^j|j\rangle, \tag{6.1}$$

where $\omega = e^{2\pi i/d}$ is the primitive d-th root of unity. X acts as a cyclic shift, and Z applies a phase ramp. They satisfy the fundamental commutation relation $ZX = \omega XZ$ [58, 66].

A symplectic vector $v = [p, q] \in \mathbb{Z}_d^2$ specifies an element of the single-qudit Heisenberg–Weyl group (up to global phase):

$$W(v) = W([p, q]) = \phi(v)X^pZ^q, \tag{6.2}$$

where $\phi(v)$ is a phase factor chosen to ensure good algebraic properties. We choose $\phi([p, q]) = \omega^{-2^{-1}pq}$, where 2^{-1} denotes the multiplicative inverse of 2 in $\mathbb{Z}_d$. With this convention, the composition law becomes:

$$W(v)W(v') = \omega^{[v,v']/2}W(v + v'), \tag{6.3}$$

where $[v, v'] = pq' - p'q$ is the symplectic inner product.

The symplectic inner product determines commutativity: $W(v)$ and $W(v')$ commute if and only if $[v, v'] = 0$. When two operators commute, the product simplifies to:

$$W(v)W(v') = W(v + v'). \tag{6.4}$$

This additivity for commuting elements imposes consistency constraints on value assignments. If a noncontextual value assignment λ assigns an outcome $\lambda(W(v))$ to observable $W(v)$, then the product relation requires $\lambda(W(v)) + \lambda(W(v')) = \lambda(W(v + v'))$ whenever $W(v)$ and $W(v')$ commute.

For a system of n qudits, an n-qudit Heisenberg–Weyl operator is specified by a symplectic vector $v = [p_1, q_1, p_2, q_2, \ldots, p_n, q_n] \in \mathbb{Z}_d^{2n}$. The operator is a tensor product of single-qudit operators:

$$W(v) = \phi(v)X^{p_1}Z^{q_1} \otimes \cdots \otimes X^{p_n}Z^{q_n}. \tag{6.5}$$

Two operators $W(v)$ and $W(v')$ commute if and only if their symplectic vectors are orthogonal under the symplectic form:

$$[v, v'] = \sum_{i=1}^{n} (p_i q'_i - p'_i q_i) = 0. \tag{6.6}$$

This condition defines the compatibility structure of the observables: two Weyl operators can be measured jointly (in the same context) if and only if they commute.

6.3 Measurement Contexts for Two Qudits

We specify which observables can be measured together. A context is a set of mutually commuting observables. Measuring a context entails choosing a common eigenbasis for all observables in the context and recording the joint eigenvalue tuple. A context is maximal if no additional commuting observable can be included.

We work with maximal commuting subsets of the two-qudit Heisenberg–Weyl group (ignoring overall phases). Let $\mathcal{C}$ denote the set of all such maximal contexts. The structure of $\mathcal{C}$ is determined by symplectic geometry: Weyl operators are labeled by vectors in $\mathbb{Z}_d^4$, and two operators commute exactly when their labels are orthogonal under the symplectic form (6.6). Maximal contexts correspond to maximal isotropic (Lagrangian) subspaces [55, 66].

Product contexts are formed by choosing one single-qudit setting on each qudit. Let $A, B \in M$ (the measurement settings defined below). The operators $A \otimes I$ and $I \otimes B$ commute because they act on different tensor factors, and together they generate the context

$$C_{AB} := \langle A \otimes I,\ I \otimes B \rangle. \tag{6.7}$$

Measuring C_{AB} implies measuring A on qudit 1 and B on qudit 2 in the same shot. The outcome is a pair $(a, b) \in \mathbb{Z}_d \times \mathbb{Z}_d$. Product contexts have product-state joint eigenbases and play a central role in our construction: the witness inequality is built from contexts C_{AB} with A ranging over M and B fixed.

Each maximal context for $n = 2$ qudits is generated by two independent commuting operators $W(v_1)$ and $W(v_2)$:

$$C = \langle W(v_1), W(v_2) \rangle = \{ W(pv_1 + qv_2) \mid p, q \in \mathbb{Z}_d \}, \tag{6.8}$$

where $[v_1, v_2] = 0$ (commutativity) and v_1, v_2 are linearly independent. Each context contains d^2 operators (including the identity) and forms an abelian subgroup isomorphic to $\mathbb{Z}_d \times \mathbb{Z}_d$. The joint eigenbasis defines a stabilizer state basis [57, 66].

The symplectic geometry of $\mathbb{Z}_d^4$ determines the total count:

$$|\mathcal{C}| = d^3 + d^2 + d + 1. \tag{6.9}$$

Of these, $(d+1)^2$ are separable product contexts of the form C_{AB}, while the remaining $d^3 - d$ are entangled contexts whose joint eigenbases are maximally entangled stabilizer states. For the logical Bell construction, we use only the existence of this maximal-context cover and the fact that it enforces Weyl product relations globally. Explicit enumeration is recorded in Appendix C.

6.3.1 Single-Qudit Measurement Settings M

Throughout this chapter we work with a distinguished family of $d+1$ single-qudit measurement settings drawn from the Weyl (generalized Pauli) observables. This choice is convenient because it is both operationally standard (it provides a complete set of stabilizer eigenbases) and geometrically structured (each setting corresponds to a direction in the discrete phase space $\mathbb{Z}_d^2$). We will repeatedly exploit these properties when translating between measurement-outcome statements and phase-space structure.

We therefore take the following $d+1$ single-qudit Weyl (generalized Pauli)/stabilizer measurement settings:

$$M = \{Z, X, XZ, XZ^2, \ldots, XZ^{d-1}\}. \tag{6.10}$$

Each element of M is a single-qudit Weyl observable (up to phase). Their eigenbases form a complete set of $d+1$ mutually unbiased bases (MUBs) for $\mathbb{C}^d$ [132, 18]. Geometrically, M corresponds to the $d+1$ directions (lines through the origin) in the single-qudit phase space $\mathbb{Z}_d^2$. For $d = 3$, this set is $M = \{Z, X, XZ, XZ^2\}$—four measurement settings, each with three possible outcomes in $\mathbb{Z}_3 = \{0, 1, 2\}$. For each $A \in M$, we specify a forbidden outcome and ask whether a noncontextual model can avoid all forbidden outcomes simultaneously.

6.4 Logical Bell Inequalities and the Marginal Witness

6.4.1 Framework and Construction

Logical Bell inequalities [5] turn logical inconsistency into experimentally testable probability bounds. The framework applies to any measurement scenario specified by a family of contexts (jointly measurable sets of observables).

Fix a set $\mathcal{C}$ of contexts. For each context $C \in \mathcal{C}$, choose a clause ϕ_C, i.e., a proposition about the outcomes observed when measuring C. Write $\Phi := \bigwedge_{C\in\mathcal{C}} \phi_C$ for the conjunction of all clauses. We say the clauses are *jointly unsatisfiable* if there is no deterministic noncontextual value assignment that makes all ϕ_C true at once.

In any noncontextual model, the observed statistics arise from a distribution over deterministic noncontextual value assignments. For each deterministic assignment, joint unsatisfiability means Φ is false, so in any such probabilistic mixture we still have

$$P(\Phi) = 0. \tag{6.11}$$

Therefore $P(\neg\Phi) = 1$. Using $\neg\Phi \equiv \bigvee_{C\in\mathcal{C}} \neg\phi_C$ and the union bound,

$$1 = P(\neg\Phi) = P\left(\bigvee_{C\in\mathcal{C}} \neg\phi_C\right) \leq \sum_{C\in\mathcal{C}} P(\neg\phi_C) = \sum_{C\in\mathcal{C}} \big(1 - P(\phi_C)\big). \tag{6.12}$$

Rearranging gives the logical Bell inequality

$$\sum_{C\in\mathcal{C}} P(\phi_C) \leq |\mathcal{C}| - 1, \tag{6.13}$$

where $|\mathcal{C}|$ is the number of contexts. Because this is a linear inequality in the probabilities, it suffices to prove joint unsatisfiability for deterministic noncontextual assignments; the bound then holds automatically for all noncontextual models obtained by mixing them. Conversely, if an empirical model violates (6.13), then it cannot be explained by any noncontextual model, so the violation witnesses contextuality.

We apply this framework to the two-qudit Heisenberg–Weyl measurement scenario. We choose clauses that are jointly inconsistent but arranged so that, after simplification, the resulting inequality depends only on probabilities for outcomes on the first qudit. The witness therefore certifies contextuality of the full two-qudit scenario while being evaluated from single-qudit statistics.

6.4.2 The Marginal Witness

We treat qudit 1 as the target system whose Wigner negativity we wish to detect. Fix an odd prime d and recall the single-qudit measurement settings $M = \{Z, X, XZ, \ldots, XZ^{d-1}\}$ from Eq. (6.10). Each setting $A \in M$ has d possible outcomes, labeled $0, 1, \ldots, d-1$.

The witness is indexed by a phase-space point $u = (p, q) \in \mathbb{Z}_d^2$. This point determines a *forbidden outcome* $r_A(u) \in \mathbb{Z}_d$ for each measurement setting $A \in M$. If $A = W([a, b])$ (so $A = X^a Z^b$ up to phase), the forbidden outcome is

$$r_A(u) := ap + bq \pmod{d}. \tag{6.14}$$

For the ordered list $M = (Z, X, XZ, \ldots, XZ^{d-1})$, this gives the outcome vector

$$r_{(p,q)} = [q,\ p,\ p+q,\ p+2q,\ \ldots,\ p+(d-1)q]. \tag{6.15}$$

Example 6.1 (Qutrit forbidden outcomes)**.** For $d = 3$, the measurement settings are $M = \{Z, X, XZ, XZ^2\}$. Consider the phase-space point $u = (1, 0)$. The forbidden outcomes are:

$$\begin{aligned} r_Z(u) &= 0 \cdot 1 + 1 \cdot 0 = 0, \\ r_X(u) &= 1 \cdot 1 + 0 \cdot 0 = 1, \\ r_{XZ}(u) &= 1 \cdot 1 + 1 \cdot 0 = 1, \\ r_{XZ^2}(u) &= 1 \cdot 1 + 2 \cdot 0 = 1. \end{aligned}$$

In words: we forbid outcome 0 for Z, outcome 1 for X, outcome 1 for XZ, and outcome 1 for XZ^2.

The forbidden outcome $r_A(u)$ has a geometric meaning. Each measurement setting $A \in M$ corresponds to a direction in the discrete phase space $\mathbb{Z}_d^2$. The eigenbasis of A partitions phase space into d parallel lines (called a striation), and the outcome value labels which line contains the point. The forbidden outcome $r_A(u)$ is the label of the line through u in the direction corresponding to A.

Measurement protocol: The witness is evaluated as follows.

1. Fix a probe setting $B \in M$ on qudit 2. (The choice does not affect the final witness value.)

2. For each $A \in M$, measure the product context $\langle A \otimes I,\ I \otimes B \rangle$. This means measuring A on qudit 1 and B on qudit 2 in the same shot.

3. Record only the first-qudit outcome, and repeat to estimate $\Pr(A = r_A(u))$ for each $A \in M$.

4. Compute the witness sum:
$$\sum_{A \in M} \Pr\big(A = r_A(u)\big). \tag{6.16}$$

6.4.3 Main Theorem

We now state the main result precisely. The theorem has two parts: an inequality that any noncontextual model must satisfy, and an identification of the witness operator with a phase-point operator.

Marginal logical Bell inequality. For any two-qudit state ρ and any phase-space point $u \in \mathbb{Z}_d^2$, every noncontextual model consistent with the Weyl product relations satisfies
$$\sum_{A \in M} \Pr\big(A = r_A(u)\big) \geq 1. \tag{6.17}$$
In terms of the reduced state $\rho_1 = \mathrm{Tr}_2(\rho)$ of qudit 1:
$$\sum_{A \in M} \mathrm{Tr}\big[\Pi_A^{r_A(u)} \rho_1\big] \geq 1, \tag{6.18}$$
where Π_A^r is the projector onto the eigenspace of A with eigenvalue ω^r.

Theorem 6.2 (Logical Bell violation $\Leftrightarrow$ marginal Wigner negativity)**.** *Let d be an odd prime and let $u \in \mathbb{Z}_d^2$. Define the witness operator*
$$A_{r(u)} := \left(\sum_{A \in M} \Pi_A^{r_A(u)} \right) - I. \tag{6.19}$$

Then:

1. ***(Inequality)*** *Any noncontextual model satisfies $\mathrm{Tr}[A_{r(u)}\, \rho_1] \geq 0$.*

2. ***(Identification)*** *$A_{r(u)} = A_u$, where A_u is the phase-point operator of the discrete Wigner representation (Section 2.4.2).*

3. ***(Equivalence)*** *Violation of the inequality occurs if and only if $W_{\rho_1}(u) < 0$.*

Proof roadmap. The proof proceeds in four steps. We describe the strategy here; the details follow in Section 6.5.

1. **Construct a logical formula for each context.** For each context, we write down a formula describing which measurement outcomes are "allowed." The general form of such a formula is a disjunction (logical OR) of events, where each event is a conjunction (logical AND) specifying a definite outcome for every observable in the context. Requiring all context formulae to be simultaneously satisfiable amounts to finding a *global value assignment*: a consistent choice of outcome for every observable. (Section 6.5.1.)

2. **Characterize global value assignments.** For Weyl observables, any global value assignment must respect the algebraic relations among commuting operators. This forces the assignment to be linear: for each qudit, the predicted outcomes correspond to a single phase-space point. (Section 6.5.2, Lemma 6.4.)

3. **Prove the formulae are jointly unsatisfiable.** The geometric structure of the discrete phase space ensures that every linear assignment predicts at least one forbidden outcome. This is because any two distinct points in $\mathbb{Z}_d^2$ lie on exactly one common line. (Section 6.5.3, Lemma 6.6.)

4. **Derive the inequality and identify the witness operator.** Since no assignment satisfies all formulae, the union bound gives a probability inequality. After simplification, this becomes the marginal inequality (6.17). The witness operator $A_{r(u)}$ equals the phase-point operator A_u by the finite-geometry structure of MUBs. (Section 6.5.4.)

6.5 Proof of the Main Result

We now prove Theorem 6.2. The proof has four parts, following the roadmap in Section 6.4.3.

6.5.1 Step 1: Constructing Logical Formulae for Contexts

We begin by explaining the general structure of logical formulae in the logical Bell framework. This structure is what connects "simultaneous satisfiability" to the existence of a global value assignment.

Events and propositions. We assign elementary logical propositions to measurement outcomes. The proposition $[A = a]$ asserts that "the measurement of observable A yields outcome a." These propositions combine using standard logical connectives:

- **Conjunction:** $[A = a] \wedge [B = b]$ means A yields a AND B yields b. This is meaningful only if A and B are jointly measurable (i.e., belong to the same context).
- **Disjunction:** $[A = a] \vee [A = a']$ means the outcome of A is either a or a'.
- **Exclusivity:** For $a \neq a'$, the proposition $[A = a] \wedge [A = a']$ is always false (a measurement yields a unique outcome).

An *event* on a context C is a complete specification of outcomes: a function $e : C \to \mathbb{Z}_d$ assigning an outcome to each observable in C. The proposition stating that event e occurs is the conjunction

$$\phi_e = \bigwedge_{A \in C} [A = e(A)]. \tag{6.20}$$

Formula for a context. For each context C, we choose a subset E_C of "allowed" events. The logical formula for context C is the disjunction over these allowed events:

$$\phi_C = \bigvee_{e \in E_C} \phi_e. \tag{6.21}$$

This formula says: "When we measure context C, the outcome is one of the allowed events in E_C."

Connection to global value assignments: A *global value assignment* is a function λ that assigns an outcome $\lambda(A) \in \mathbb{Z}_d$ to every observable A in our measurement scenario. Suppose we require all context formulae ϕ_C to be true simultaneously. For each context C, the formula ϕ_C being true means the outcomes must match some allowed event $e \in E_C$. If an observable A appears in two different contexts C_1 and C_2, the assigned outcome must be consistent: $\lambda(A)$ must be the same in both.

Therefore: *the formulae $\{\phi_C\}_{C \in \mathcal{C}}$ are simultaneously satisfiable if and only if there exists a global value assignment λ such that, for every context C, the restriction of λ to C is an allowed event in E_C.*

We now restrict to the two-qudit Weyl measurement scenario. Fix a probe setting $B \in M$ on qudit 2. Consider the $d+1$ product contexts

$$\mathcal{C}_B = \{C_A = \langle A \otimes I,\, I \otimes B \rangle \mid A \in M\}. \tag{6.22}$$

For each context $C_A \in \mathcal{C}_B$, we define the allowed events to be those where the first-qudit outcome is *not* the forbidden value $r_A(u)$. That is:

$$E_{C_A} = \{e : C_A \to \mathbb{Z}_d \mid e(A \otimes I) \neq r_A(u)\}. \tag{6.23}$$

The corresponding formula simplifies to:

$$\phi_{C_A} \equiv [A \otimes I \neq r_A(u)]. \tag{6.24}$$

For all other contexts $C' \in \mathcal{C} \setminus \mathcal{C}_B$, we allow all possible events: $E_{C'} = E(C')$. The formula becomes a tautology: $\phi_{C'} \equiv \text{True}$. These tautological formulae impose no constraint on their own, but they play a crucial role: they force any satisfying assignment to be globally consistent across the entire measurement scenario.

Example 6.3 (Qutrit formulae)**.** For $d = 3$ with target point $u = (1, 0)$, the forbidden outcomes are $(r_Z, r_X, r_{XZ}, r_{XZ^2}) = (0, 1, 1, 1)$. The four nontrivial formulae are:

$$\begin{aligned} \phi_{C_Z} &\equiv [Z \neq 0], \\ \phi_{C_X} &\equiv [X \neq 1], \\ \phi_{C_{XZ}} &\equiv [XZ \neq 1], \\ \phi_{C_{XZ^2}} &\equiv [XZ^2 \neq 1]. \end{aligned}$$

All other contexts have tautological formulae. The question is: can we find a global value assignment that makes all formulae true?

6.5.2 Step 2: Characterizing Global Value Assignments

We now show that global value assignments for Weyl observables have a special structure. A global value assignment λ must satisfy:

- **Contextual consistency:** If A belongs to two different contexts, $\lambda(A)$ is the same in both.

- **Product rule:** For commuting Weyl operators, $\lambda(W(v))+\lambda(W(v'))=\lambda(W(v+v'))$ mod d. This respects the algebraic relation (6.4).

These requirements force λ to be linear.

Lemma 6.4 (Structure of global assignments [42])**.** *A global value assignment λ for two-qudit Weyl observables, consistent with the product relations, must be linear:*

$$\lambda\big(W(v)\big) = \lambda \cdot v \tag{6.25}$$

for some vector $\lambda \in \mathbb{Z}_d^4$, where the dot denotes the standard inner product modulo d.

This lemma says that a global assignment is determined by four numbers $(\lambda_1, \lambda_2, \lambda_3, \lambda_4) \in \mathbb{Z}_d^4$. The first two coordinates (λ_1, λ_2) specify a phase-space point $x = (\lambda_1, \lambda_2) \in \mathbb{Z}_d^2$ for qudit 1. The last two coordinates specify a phase-space point for qudit 2.

The reduction is significant: instead of d^{2d^2} arbitrary outcome tables, there are only d^4 possible global assignments. Our task is to show that none of these d^4 assignments satisfies all our formulae.

Example 6.5. For $d = 3$, suppose a global assignment gives $\lambda(X\otimes I) = 2$ and $\lambda(Z\otimes I) = 1$. Linearity forces

$$\lambda(XZ^i \otimes I) = \lambda(X \otimes I) + i \cdot \lambda(Z \otimes I) = 2 + i \pmod 3.$$

So the assignment predicts: $Z \mapsto 1$, $X \mapsto 2$, $XZ \mapsto 0$, $XZ^2 \mapsto 1$. This is exactly the outcome pattern for phase-space point $x = (2, 1)$.

6.5.3 Step 3: Proving Joint Unsatisfiability

We now show that no global assignment can satisfy all formulae. The argument uses the geometry of the discrete phase space. The phase space $\mathbb{Z}_d^2$ is a finite plane with d^2 points. It has exactly $d+1$ directions (corresponding to our $d+1$ measurement settings). The key property is: *any two distinct points lie on exactly one common line.*

This means: if $x \neq u$, there is exactly one direction in which x and u lie on the same line. For that direction, both points predict the same outcome.

Lemma 6.6 (Unique matching setting)**.** *Fix $u = (p, q) \in \mathbb{Z}_d^2$ and let $r_A(u)$ be defined by Eq. (6.15). For any $x = (p', q') \neq u$, exactly one setting $A \in M$ satisfies $r_A(x) = r_A(u)$.*

Proof. We consider two cases.

Case 1: $q' = q$**.** Then $r_Z(x) = q' = q = r_Z(u)$, so Z matches. For any XZ^i, we have $r_{XZ^i}(x) - r_{XZ^i}(u) = (p' - p) \neq 0$ (since $x \neq u$ and $q' = q$ implies $p' \neq p$). So no XZ^i matches. The unique match is Z.

Case 2: $q' \neq q$**.** Then $r_Z(x) = q' \neq q = r_Z(u)$, so Z does not match. For XZ^i, the condition $r_{XZ^i}(x) = r_{XZ^i}(u)$ requires $(p' - p) + i(q' - q) = 0$, giving $i = (p - p')(q' - q)^{-1}$. Since d is prime and $q' - q \neq 0$, the inverse exists and there is exactly one such $i \in \mathbb{Z}_d$. □

Example 6.7 (Unique matching in the qutrit)**.** For $d = 3$ with target point $u = (1, 0)$ and forbidden outcomes $(0, 1, 1, 1)$:

Consider $x = (0, 0)$ (same row as u). The predicted outcomes are $(r_Z, r_X, r_{XZ}, r_{XZ^2}) = (0, 0, 0, 0)$. This matches the forbidden outcomes only for Z.

Consider $x = (2, 1)$ (different row from u). The predicted outcomes are $(1, 2, 0, 1)$. This matches the forbidden outcomes only for XZ^2.

Consider $x = (1, 1)$ (different row from u). The predicted outcomes are $(1, 1, 2, 0)$. This matches the forbidden outcomes only for X.

Every point $x \neq u$ matches exactly one forbidden outcome.

Claim 6.8 (Joint unsatisfiability)**.** *For any $u \in \mathbb{Z}_d^2$, no global value assignment satisfies all formulae $\{\phi_C\}_{C \in \mathcal{C}}$.*

Proof. Suppose a global assignment λ satisfies all formulae. By Lemma 6.4, λ is linear, so its restriction to qudit 1 corresponds to some phase-space point $x = (\lambda_1, \lambda_2)$. Satisfying ϕ_{C_A} requires $\lambda(A \otimes I) = r_A(x) \neq r_A(u)$ for all $A \in M$.

If $x = u$, then $r_A(x) = r_A(u)$ for all A—contradicting every ϕ_{C_A}.

If $x \neq u$, Lemma 6.6 gives a unique A^* with $r_{A^*}(x) = r_{A^*}(u)$—contradicting $\phi_{C_{A^*}}$.

Either way, at least one formula is false. □

6.5.4 Step 4: Deriving the Inequality and Identifying the Witness

Since the formulae are jointly unsatisfiable (Claim 6.8), the logical Bell framework gives a probability inequality.

Let $\Phi := \bigwedge_{C \in \mathcal{C}} \phi_C$ be the conjunction of all formulae. By Claim 6.8, Φ is unsatisfiable. In any noncontextual model, the probability of Φ is therefore zero: $P(\Phi) = 0$.

The negation $\neg\Phi = \bigvee_C \neg\phi_C$ has probability one. By the union bound:

$$1 = P(\neg\Phi) \leq \sum_{C \in \mathcal{C}} P(\neg\phi_C) = \sum_{C \in \mathcal{C}} \big(1 - P(\phi_C)\big).$$

Rearranging:

$$\sum_{C \in \mathcal{C}} P(\phi_C) \leq |\mathcal{C}| - 1. \tag{6.26}$$

The tautological formulae $\phi_{C'}$ for $C' \in \mathcal{C} \setminus \mathcal{C}_B$ satisfy $P(\phi_{C'}) = 1$. There are $|\mathcal{C}| - (d+1)$ such formulae, contributing $|\mathcal{C}| - (d+1)$ to the left-hand side of (6.26). After cancellation with the right-hand side:

$$\sum_{A \in M} P(\phi_{C_A}) \leq d.$$

Since $\phi_{C_A} \equiv [A \otimes I \neq r_A(u)]$, we have $P(\phi_{C_A}) = 1 - P(A = r_A(u))$. Substituting:

$$\sum_{A \in M} P(A = r_A(u)) \geq 1. \tag{6.27}$$

Since $P(A \otimes I = r_A(u)) = \mathrm{Tr}[\Pi_A^{r_A(u)} \rho_1]$ depends only on the reduced state $\rho_1 = \mathrm{Tr}_2(\rho)$, we obtain Eq. (6.18).

Example 6.9 (Qutrit inequality)**.** For $d = 3$ with target point $u = (1, 0)$:

$$\Pr(Z = 0) + \Pr(X = 1) + \Pr(XZ = 1) + \Pr(XZ^2 = 1) \geq 1.$$

The final step is to show that $A_{r(u)} = A_u$. In the discrete Wigner representation (Section 2.4.2), the Wigner function of a state σ at point u is $W_\sigma(u) = \frac{1}{d} \mathrm{Tr}(\sigma A_u)$. The phase-point operator A_u is constructed as follows: each phase-space point lies on exactly one line in each of the $d+1$ directions, and the projector onto the corresponding eigenspace of the associated measurement is $\Pi_A^{r_A(u)}$. Summing over all directions and subtracting the identity gives:

$$A_u = \left(\sum_{A \in M} \Pi_A^{r_A(u)} \right) - I = A_{r(u)}. \tag{6.28}$$

For a detailed derivation, see Wootters [130] or Gross [59].

From $A_{r(u)} = A_u$ and the definition $W_{\rho_1}(u) = \frac{1}{d}\operatorname{Tr}(\rho_1 A_u)$:

$$\operatorname{Tr}(A_{r(u)}\rho_1) = d \cdot W_{\rho_1}(u).$$

The inequality $\sum_A \operatorname{Tr}[\Pi_A^{r_A(u)}\rho_1] \geq 1$ is equivalent to $\operatorname{Tr}(A_{r(u)}\rho_1) \geq 0$, which is equivalent to $W_{\rho_1}(u) \geq 0$. Violation means $W_{\rho_1}(u) < 0$. This completes the proof of Theorem 6.2. □

Example 6.10 (Qutrit phase-point operator)**.** For $d = 3$ and $u = (1, 0)$:

$$A_u = A_{r(u)} = \Pi_Z^0 + \Pi_X^1 + \Pi_{XZ}^1 + \Pi_{XZ^2}^1 - I.$$

6.6 Quantitative Bound: Contextual Fraction

Theorem 6.2 provides a qualitative witness: violation certifies Wigner negativity. We turn to a quantitative question: given a violation, how much contextuality is present?

The contextual fraction (Section 2.3) provides an answer. It is a normalized measure $\mathrm{CF}(E) \in [0, 1]$ associated with an empirical model E [3], defined as the minimum weight of contextuality needed to reproduce the observed statistics. Howard et al. [67] identify contextuality as the key obstruction to classical simulation of stabilizer computation with magic states, so contextual fraction quantifies this obstruction. Given noncontextual bound b and algebraic maximum m for any noncontextuality inequality, the normalized violation $(I(E) - b)/(m - b)$ lower-bounds $\mathrm{CF}(E)$. For logical Bell inequalities, this bound takes a simple form.

Fix a probe setting $B \in M$ on the second qudit and a phase-space point $u = (p, q)$ on the first. For each $A \in M$, define the satisfaction probability $s_A := P(\phi_{C_A}) = 1 - \Pr(A \otimes I = r_A(u))$ and the clause sum $S := \sum_{A \in M} s_A$. The logical Bell inequality (6.17) is exactly the noncontextual bound $S \leq d$, while the algebraic bound is $S \leq d + 1$. By the general relationship between contextual fraction and normalized violations [3], we obtain

$$\mathrm{CF}(E) \geq \frac{\max\{0, S - d\}}{(d + 1) - d} = \max\{0, S - d\}. \tag{6.29}$$

This bound is straightforward to evaluate: S depends only on $(d + 1)$ first-qudit probabilities.

For a quantum realization by a two-qudit state ρ with marginal $\sigma = \operatorname{Tr}_2(\rho)$, the violation can be rewritten in phase-space terms. Using the definition of $A_{r(u)}$ from Eq. (6.19):

$$S = (d + 1) - \sum_{A \in M} \operatorname{Tr}(\Pi_A^{r_A(u)}\,\sigma) = d - \operatorname{Tr}(A_{r(u)}\,\sigma). \tag{6.30}$$

With the identification $A_{r(u)} = A_u$ from Eq. (6.28), Eq. (6.29) becomes:

$$\mathrm{CF}(E) \geq \max\{0, -\mathrm{Tr}(A_{r(u)}\,\sigma)\} = \max\{0, -d\,W_\sigma(u)\}. \tag{6.31}$$

Theorem 6.11 (Wigner negativity lower-bounds contextual fraction)**.** *For a two-qudit state ρ with marginal $\sigma = \mathrm{Tr}_2(\rho)$, marginal Wigner negativity lower-bounds the contextual fraction of the associated empirical model:*

$$\mathrm{CF}(E) \geq d \cdot \max_{u \in \mathbb{Z}_d^2} |W_\sigma(u)|^-, \tag{6.32}$$

where $|x|^- := \max\{0, -x\}$ denotes the negative part.

Marginal Wigner negativity therefore certifies contextuality and provides a state-dependent lower bound on its magnitude.

6.7 Generalizations

The two-qudit construction is the simplest instance of a more general pattern. The method extends to systems with more qudits and, in principle, witnesses Wigner negativity of multi-qudit marginals.

6.7.1 Witnessing Single-Qudit Wigner Negativity with n Qudits

The two-qudit logical Bell inequality generalizes to n-qudit systems while still witnessing a single-qudit marginal. The auxiliary qudits play two logically distinct roles:

1. They enforce that any deterministic noncontextual model extends to a global linear value assignment on Weyl observables (Lemma 6.4).
2. They supply enough context structure for this global assignment to be the relevant notion of noncontextuality.

Neither role requires a single auxiliary qudit; any number of auxiliary qudits $n - 1 \geq 1$ suffices.

Construction recipe: Fix $n \geq 2$ qudits in odd prime local dimension d, with qudit 1 as the target and qudits $2, \ldots, n$ as auxiliary.

1. **Choose probe settings:** For each auxiliary qudit $j = 2, \ldots, n$, choose an arbitrary probe observable $B_j \in M$. The choice does not affect the final witness value.

2. **Define the product contexts:** For each $A \in M$, define the n-qudit product context:
$$C_A := \langle A \otimes I^{\otimes(n-1)},\ I \otimes B_2 \otimes I^{\otimes(n-2)},\ \ldots,\ I^{\otimes(n-1)} \otimes B_n \rangle. \tag{6.33}$$

3. **Fix the target phase-space point:** Choose a phase-space point $u \in \mathbb{Z}_d^2$ on qudit 1. This determines forbidden outcomes $r_A(u)$ for each $A \in M$ via Eq. (6.15).

4. **Assign logical clauses:** For each context C_A, define the nontrivial clause:
$$\phi_{C_A} \equiv [A \otimes I^{\otimes(n-1)} \neq r_A(u)]. \tag{6.34}$$
All other maximal contexts in the n-qudit Weyl measurement scenario are assigned tautological clauses.

The inconsistency proof reduces to the same single-qudit geometric argument as in Section 6.5.3:

- The tautological contexts enforce global linear value assignments on all n-qudit Weyl observables [42].
- Restricting to first-qudit observables, any such assignment corresponds to a phase-space point $x \in \mathbb{Z}_d^2$.
- By Lemma 6.6: if $x = u$, all clauses fail; if $x \neq u$, exactly one clause fails.

Either way, the clauses are jointly unsatisfiable.

Applying the union bound yields the marginal inequality:
$$\sum_{A \in M} \mathrm{Tr}\big(\Pi_A^{r_A(u)}\, \rho_1\big) \geq 1, \tag{6.35}$$
where $\rho_1 = \mathrm{Tr}_{2\ldots n}(\rho)$ is the reduced state of qudit 1. This is identical to the two-qudit inequality (6.18). Violation occurs if and only if $W_{\rho_1}(u) < 0$.

6.7.2 Witnessing k-Qudit Marginal Wigner Negativity

Witnessing Wigner negativity of a k-qudit marginal (with $k \geq 2$), requires a generalization of the single-qudit measurement settings (from set M) to their k-qudit analogues.

The single-qudit construction relies on three geometric facts about $\mathbb{Z}_d^2$:

1. There are $d+1$ directions (lines through the origin), corresponding to the $d+1$ measurement settings in M.
2. Each point lies on exactly one line in each direction.
3. Any two distinct points share exactly one line.

For k qudits, the phase space is $\mathbb{Z}_d^{2k}$, and these facts generalize as follows:

1. The $d+1$ directions are replaced by d^k+1 maximal isotropic (Lagrangian) subspaces forming a *symplectic spread* [71, 43]. Each subspace corresponds to a maximal commuting stabilizer measurement on the k-qudit subsystem.
2. Each phase-space point $u \in \mathbb{Z}_d^{2k}$ lies in exactly one subspace from each "direction" in the spread, determining a forbidden outcome for each measurement.
3. The displacement argument generalizes: any two distinct points $x \neq u$ differ in all but one spread element.

Construction recipe: Fix $n \geq k+1$ qudits, with qudits $1, \ldots, k$ as the target subsystem and qudits $k+1, \ldots, n$ as auxiliary.

1. **Choose k-qudit measurement settings.** Let M_k be a complete set of d^k+1 maximal commuting stabilizer measurements on the k-qudit target subsystem, corresponding to a symplectic spread of $\mathbb{Z}_d^{2k}$.
2. **Choose probe settings on auxiliary qudits.** For each auxiliary qudit $j = k+1, \ldots, n$, choose an arbitrary probe observable $B_j \in M$.
3. **Define the product contexts.** For each $A \in M_k$, define the n-qudit product context generated by A on the target subsystem and the probe observables on the auxiliary qudits.

4. **Fix the target phase-space point.** Choose $u \in \mathbb{Z}_d^{2k}$. For each $A \in M_k$, this determines a forbidden outcome $r_A(u)$.

5. **Assign logical clauses.** For each context C_A, define the clause $\phi_{C_A} \equiv [A \neq r_A(u)]$. All other maximal contexts are assigned tautological clauses.

The global linear assignment structure and the symplectic geometry of spreads would ensure that no deterministic noncontextual assignment can avoid all forbidden outcomes. The union bound would then yield an inequality involving only the k-qudit marginal statistics.

With this general construction, the logical Bell inequality is of the form:

$$\sum_{A \in M_k} \mathrm{Tr}\big(\Pi_A^{r_A(u)} \rho_k\big) \geq 1, \tag{6.36}$$

where $\rho_k = \mathrm{Tr}_{k+1\ldots n}(\rho)$ is the reduced state of the k-qudit target subsystem. Violation is equivalent to $W_{\rho_k}(u) < 0$, i.e., Wigner negativity of the k-qudit marginal at the chosen phase-space point.

The detailed verification that symplectic spreads provide the required geometric structure, and the explicit construction of the corresponding phase-point operators, is left for future work.

6.8 Discussion

This chapter constructs a family of noncontextuality inequalities that can be evaluated from target-qudit Weyl measurement statistics and that witness marginal discrete Wigner negativity in odd prime dimension. For each phase-space point $u \in \mathbb{Z}_d^2$, the witness has a particularly simple form: it depends only on the $d+1$ probabilities $\Pr(A = r_A(u))$ for $A \in M$. We identify the corresponding witness operator with the Wigner phase-point operator (Theorem 6.2), and hence obtain an exact criterion: the inequality is violated if and only if the reduced state ρ_1 satisfies $W_{\rho_1}(u) < 0$. In addition, the same marginal data provide a state-dependent lower bound on the contextual fraction of the underlying two-qudit empirical model (Theorem 6.11).

Methodologically, the crucial step is to enlarge the compatibility structure without enlarging the required data. For a single qudit, the Weyl (generalized Pauli) settings do not furnish enough overlapping contexts to witness contextuality. By introducing a second

(auxiliary) qudit and working with product contexts, one enforces the global Weyl product constraints needed for the logical contradiction, while the resulting inequality collapses to a statement about the target marginal.

The "one designated outcome per setting" form is a reflection of the geometry underlying the discrete Wigner representation. Each setting $A \in M$ determines a striation of phase space, and the label $r_A(u)$ picks out the unique line in that striation containing the point u. Summing the corresponding projectors over all $d+1$ striations and subtracting the identity yields the phase-point operator. Theorem 6.2 therefore shows that the logical Bell witness is not merely correlated with Wigner negativity; it is the Wigner test at the operator level.

The marginal inequalities themselves were first presented by Howard *et al.* [67]. The present chapter recasts them in the logical Bell framework of Abramsky and Hardy [5], which is useful for two reasons. First, it makes the structure of the argument transparent: global consistency (linearity) is forced by the Weyl product relations, and the obstruction reduces to a finite-geometry incidence statement (Lemma 6.6). Second, it provides a general template for extensions. Once the proof is organized into "consistency from contexts" plus "geometric obstruction," one can vary the context structure (e.g., add spectator systems) or the geometry (e.g., replace single-qudit striations by symplectic-spread structure to target k-qudit marginals) while preserving the same logical-to-probabilistic derivation.

The contextual-fraction bound derived in Section 6.6 complements the qualitative "negativity or not" statement. For a given u, the quantity $-d\,W_{\rho_1}(u)$ is directly lower-bounded by the normalized logical Bell violation, and hence provides an operational certificate of a minimum amount of contextuality required to reproduce the observed statistics. This connects the phase-space picture to a convex-geometric measure on empirical models without requiring full tomography of the two-qudit distribution. In resource-theoretic terms, the witness simultaneously identifies a specific location of quasiprobability negativity and guarantees a nonzero contextual component in any noncontextual decomposition.

Chapter 7

Conclusion and Outlook

This thesis brings together several studies of operational witnesses of non-classicality, developed in different physical settings and motivated by distinct questions. A common methodological stance nevertheless runs through them: claims of "classical" versus "non-classical" are only meaningful relative to an explicitly specified preparation-and-measurement scenario. Accordingly, rather than proposing a single scalar measure of "quantumness," each study asks what can be certified against a clearly stated class of classical models (local hidden-variable models, noncontextual models for compatibility tests, or positivity in a discrete phase-space representation), and how that certification depends on both the state and the available measurements.

In the multipartite setting, it was shown that closed-form, measurement-optimized Svetlichny-type values can be obtained for two N-qubit state families, enabling an analytic comparison between a genuine multipartite entanglement indicator (the n-tangle, for even N) and a standard device-independent witness of genuine multipartite nonlocality [118, 40, 109, 129, 39, 117]. Within the generalized GHZ family (even $N > 2$), for any nonzero n-tangle, a Svetlichny violation is only possible once the n-tangle exceeds $1/2$, and this threshold is independent of N. For the maximal-slice family, the optimized Svetlichny value violates the hybrid-local bound for any nonzero n-tangle and the violation grows monotonically with it. The conversion of coherence into a Svetlichny-type violation depends on structural features of the state and on the measurement constraints built into the witness.

The spin-1 quantum kicked top was analyzed to assess whether contextuality in the evolving state can serve as a practical indicator of the regular-versus-chaotic structure of the associated classical map [62, 61, 36]. Contextuality was quantified via the measurement-

optimized KCBS violation as a state-dependent witness [72], and the numerical results show a clear global trend: as the kick strength increases, a larger fraction of randomly sampled spin-coherent initial states exhibit contextuality within the finite time window tested, with localized features near classical bifurcation points. At the same time, the analysis identified that unstable fixed points can generate large KCBS values even though the corresponding classical orbit is trivial. A heuristic hybrid diagnostic was introduced to address the unstable-fixed-point artefacts; within the tested ($j = 1$) window it yields phase-space contours that qualitatively match the regular-island/chaotic-sea structure. In this minimal ($j = 1$) setting, contextuality can function as a useful operational marker of state-space delocalization and exploration mechanisms that correlate with classical chaos.

The operational viewpoint was extended to a relativistic field setting by analyzing two qutrit Unruh–DeWitt detectors coupled locally to a massless scalar field in the Minkowski vacuum [120, 44, 105, 102]. Working perturbatively in the weak-coupling regime, the induced two-detector state was evaluated to leading nontrivial order ($O(\lambda^2)$) and used to construct a two-qutrit Heisenberg–Weyl empirical model. Across the parameter ranges explored (detector gap, interaction duration, smearing scale, and separation), numerical evidence shows regimes in which the contextual fraction becomes nonzero even for effectively spacelike-separated interactions, and suggests that this onset is correlated with the emergence of discrete Wigner-function negativity in the reduced single-detector state. The same data also exhibits a consistent tradeoff: contextuality/negativity is non-monotonic in the dimensionless gap parameter and is strongly suppressed by spatial smearing and by large separation, consistent with a balance between vacuum-induced coherence and local excitation noise at leading order.

Finally, in the contextuality and phase-space setting, it was shown that an explicit marginal witness of discrete Wigner-function negativity can be constructed using the framework of logical Bell inequalities [5, 130, 59]. For two qudits in odd prime local dimension and Heisenberg–Weyl measurement contexts, a family of inequalities indexed by a phase-space point was constructed and shown to be violated if and only if the reduced state of one qudit has a negative Gross discrete Wigner value at that point. Here the second qudit plays an enabling role by supplying a compatibility structure rich enough to force global (algebraically consistent) value assignments, while the resulting inequality can be evaluated using only first-qudit outcome statistics. In addition, the same normalized violation yields a state-dependent lower bound on the contextual fraction [3] of the corresponding empirical model. In the odd-prime Heisenberg–Weyl setting studied here, pointwise Wigner negativity of a single-qudit marginal is exactly equivalent to violating a noncontextuality inequality that can be evaluated from that qudit's statistics, complementing the established contextuality–negativity correspondences for multi-qudit Pauli measurements [67, 42].

Across all four settings, the main results are established under specific modeling choices (state families, measurement sets, perturbative truncation, and finite observation windows). A natural next step is therefore to quantify how the conclusions change when these assumptions are relaxed: include explicit noise and miscalibration models, restrict the allowed measurement families to those that are experimentally realistic, and treat the inequalities as finite-sample statistical tests with well-defined uncertainties. Such robustness questions are standard in device-independent and related certification approaches, and they would make the present benchmarks easier to compare against experimental data [29, 90].

For the multipartite study, the availability of analytic, measurement-optimized Svetlichny benchmarks makes it feasible to use these values as calibration targets and as inputs to robustness analyses, including comparisons across alternative GMN witnesses and across explicit noise models. It also invites a broader search for additional state families (and mixed-state models) for which similar optimizations can be obtained, so that analytic benchmarks can guide experimental design rather than only after-the-fact interpretation. For the phase-space study, the marginal logical-Bell inequalities suggest a lightweight alternative to full discrete-Wigner reconstruction: the immediate goal is to develop finite-sample versions of the tests, with explicit confidence guarantees and clear resource requirements, and to extend the construction beyond single-qudit marginals while keeping the evaluation based only on marginal statistics [122, 95, 3].

For the kicked-top study, extending beyond the minimal spin-1 model is essential to separate short recurrences from semiclassical trends and to compare contextuality-based signatures against standard quantum-chaos probes such as spectral statistics and fidelity decay [61, 25, 68, 10]. It is equally important to quantify robustness under realistic imperfections (dephasing, control noise, and limited measurement resolution), since these effects can wash out the fine structure that a state-dependent witness detects. For the detector–field study, the natural outlook is to move beyond leading-order weak coupling and to vary both field state and geometry in a controlled way, building on the wider literature on correlation and entanglement harvesting [105, 102, 28, 119]. This would clarify which features of the witnessed contextuality are driven by field correlations and which are artifacts of approximations or measurement assumptions, and it would help identify parameter regimes where contextuality provides a useful diagnostic alongside more familiar correlation measures.

References

[1] Scott Aaronson and Daniel Gottesman. Improved simulation of stabilizer circuits. *Physical Review A*, 70(5):052328, 2004.

[2] Alastair A. Abbott, Jonathan Wechs, Fabio Costa, and Cyrille Branciard. Genuinely multipartite noncausality. *Quantum*, 1:39, 2017.

[3] Samson Abramsky, Rui Soares Barbosa, and Shane Mansfield. Contextual fraction as a measure of contextuality. *Physical Review Letters*, 119(5):050504, 2017.

[4] Samson Abramsky and Adam Brandenburger. The sheaf-theoretic structure of non-locality and contextuality. *New Journal of Physics*, 13(11):113036, 2011.

[5] Samson Abramsky and Lucien Hardy. Logical bell inequalities. *Physical Review A*, 85(6):062114, 2012.

[6] Antonio Acín, Andrei Andrianov, Lluis Costa, Emilio Jané, Julio I. Latorre, and Rosario Tarrach. Generalized Schmidt decomposition and classification of three-quantum-bit states. *Physical Review Letters*, 85(7):1560–1563, 2000.

[7] Antonio Acín, Nicolas Brunner, Nicolas Gisin, Serge Massar, Stefano Pironio, and Valerio Scarani. Device-independent security of quantum cryptography against collective attacks. *Physical Review Letters*, 98(23):230501, 2007.

[8] Ashok Ajoy and Pranaw Rungta. Svetlichny's inequality and genuine tripartite nonlocality in three-qubit pure states. *Physical Review A*, 81(5):052334, 2010.

[9] José Raúl González Alonso, Nathan Shammah, Shahnawaz Ahmed, Franco Nori, and Justin Dressel. Diagnosing quantum chaos with out-of-time-ordered-correlator quasiprobability in the kicked-top model. *arXiv preprint*, 2022.

[10] Amit Anand, Jack Davis, and Shohini Ghose. Quantum recurrences in the kicked top. *Physical Review Research*, 6(2):023120, 2024.

[11] Amit Anand, Sanchit Srivastava, Sayan Gangopadhyay, and Shohini Ghose. Simulating quantum chaos on a quantum computer. *Scientific Reports*, 14(1):26890, 2024.

[12] F. T. Arecchi, E. Courtens, R. Gilmore, and H. Thomas. Atomic coherent states in quantum optics. *Physical Review A*, 6(6):2211–2237, 1972.

[13] Remigiusz Augusiak, Mateusz Demianowicz, Jordi Tura, and Antonio Acín. Entanglement and nonlocality are inequivalent for any number of parties. *Physical Review Letters*, 115(3):030404, 2015.

[14] Jean-Daniel Bancal, Cyril Branciard, Nicolas Gisin, and Stefano Pironio. Quantifying multipartite nonlocality. *Physical Review Letters*, 103(9):090503, 2009.

[15] Jean-Daniel Bancal, Nicolas Brunner, Nicolas Gisin, and Yeong-Cherng Liang. Detecting genuine multipartite quantum nonlocality: A simple approach and generalization to arbitrary dimensions. *Physical Review Letters*, 106(2):020405, 2011.

[16] Jean-Daniel Bancal, Nicolas Gisin, Yeong-Cherng Liang, and Stefano Pironio. Device-independent witnesses of genuine multipartite entanglement. *Physical Review Letters*, 106(25):250404, 2011.

[17] J. N. Bandyopadhyay and A. Lakshminarayan. Testing statistical bounds on entanglement using quantum chaos. *Physical Review Letters*, 89(6):060402, 2002.

[18] Somshubhro Bandyopadhyay, P. Oscar Boykin, Vwani Roychowdhury, and Farrokh Vatan. A new proof for the existence of mutually unbiased bases. *Algorithmica*, 34(4):512–528, 2002.

[19] Jordi Batle, C. H. Raymond Ooi, S. Abdalla, and A. Bagdasaryan. Computing the maximum violation of a Bell inequality is an NP-problem. *Quantum Information Processing*, 15(6):2649–2659, 2016.

[20] Ämin Baumeler, Aamir S. Gilani, and Junaid Rashid. Unlimited non-causal correlations and their relation to non-locality. *Quantum*, 6:673, 2022.

[21] J. S. Bell. On the problem of hidden variables in quantum mechanics. *Reviews of Modern Physics*, 38(3):447–452, 1966.

[22] John S. Bell. On the Einstein Podolsky Rosen paradox. *Physics Physique Fizika*, 1(3):195–200, 1964.

[23] Kishor Bharti, Mridul Ray, Zhen-Peng Xu, Masahito Hayashi, Leong-Chuan Kwek, and Adán Cabello. Graph-theoretic approach for self-testing in Bell scenarios. *PRX Quantum*, 3(3):030344, 2022.

[24] N. D. Birrell and P. C. W. Davies. *Quantum Fields in Curved Space*. Cambridge Monographs on Mathematical Physics. Cambridge University Press, Cambridge, 1982.

[25] O. Bohigas, M.-J. Giannoni, and C. Schmit. Characterization of chaotic quantum spectra and universality of level fluctuation laws. *Physical Review Letters*, 52(1):1–4, 1984.

[26] Adam Brandenburger. Quantum contextuality. In Lorenzo Magnani and Tommaso Bertolotti, editors, *Springer Handbook of Model-Based Science*, pages 1063–1081. Springer, Cham, 2017.

[27] Sergey Bravyi and Alexei Kitaev. Universal quantum computation with ideal Clifford gates and noisy ancillas. *Physical Review A*, 71(2):022316, 2005.

[28] Eric G. Brown. Thermal amplification of field-correlation harvesting. *Physical Review A*, 88(6):062336, 2013.

[29] Nicolas Brunner, Daniel Cavalcanti, Stefano Pironio, Valerio Scarani, and Stephanie Wehner. Bell nonlocality. *Reviews of Modern Physics*, 86(2):419–478, 2014.

[30] Nicolas Brunner, Jean Sharam, and Tamás Vértesi. Testing the structure of multipartite entanglement with Bell inequalities. *Physical Review Letters*, 108(11):110501, 2012.

[31] Costantino Budroni, Adán Cabello, Otfried G"uhne, Matthias Kleinmann, and Jan-Åke Larsson. Kochen-Specker contextuality. *Reviews of Modern Physics*, 94(4):045007, 2022.

[32] Adán Cabello, Matthias Kleinmann, and José R. Portillo. Quantum state-independent contextuality requires 13 rays. *Journal of Physics A: Mathematical and Theoretical*, 49(38):38LT01, 2016.

[33] Adán Cabello, Simone Severini, and Andreas Winter. Graph-theoretic approach to quantum correlations. *Physical Review Letters*, 112(4):040401, 2014.

[34] K. E. Cahill and R. J. Glauber. Density operators and quasiprobability distributions. *Physical Review*, 177(5):1882–1902, 1969.

[35] Hilary A. Carteret, Artur Higuchi, and Akimasa Sudbery. Multipartite generalization of the Schmidt decomposition. *Journal of Mathematical Physics*, 41(12):7932–7939, 2000.

[36] S. Chaudhury, A. Smith, B. E. Anderson, S. Ghose, and P. S. Jessen. Quantum signatures of chaos in a kicked top. *Nature*, 461:768–771, 2009.

[37] Boris S. Cirel'son. Quantum generalizations of Bell's inequality. *Letters in Mathematical Physics*, 4(2):93–100, 1980.

[38] John F. Clauser, Michael A. Horne, Abner Shimony, and Richard A. Holt. Proposed experiment to test local hidden-variable theories. *Physical Review Letters*, 23(15):880–884, 1969.

[39] Valerie Coffman, Joydip Kundu, and William K. Wootters. Distributed entanglement. *Physical Review A*, 61(5):052306, 2000.

[40] Daniel Collins, Nicolas Gisin, Sandu Popescu, David Roberts, and Valerio Scarani. Bell-type inequalities to detect true n-body nonseparability. *Physical Review Letters*, 88(17):170405, 2002.

[41] Flavien J. Curchod, Yeong-Cherng Liang, and Nicolas Gisin. Multipartite nonlocality as a resource and quantum correlations having indefinite causal order. *Journal of Physics A: Mathematical and Theoretical*, 47(42):424014, 2014.

[42] Nicolas Delfosse, Cihan Okay, Juan Bermejo-Vega, Dan E. Browne, and Robert Raussendorf. Equivalence between contextuality and negativity of the Wigner function for qudits. *New Journal of Physics*, 19(12):123024, 2017.

[43] Peter Dembowski. *Finite Geometries*. Springer-Verlag, Berlin, 1968.

[44] Bryce S. DeWitt. Quantum gravity: The new synthesis. In S. W. Hawking and W. Israel, editors, *General Relativity: An Einstein Centenary Survey*, pages 680–745. Cambridge University Press, 1980.

[45] Shruti Dogra, Kavita Dorai, and Arvind. Experimental demonstration of quantum contextuality on an NMR qutrit. *Physics Letters A*, 380(22-23):1941–1946, 2016.

[46] W. Dür, G. Vidal, and J. I. Cirac. Three qubits can be entangled in two inequivalent ways. *Physical Review A*, 62(6):062314, 2000.

[47] Albert Einstein, Boris Podolsky, and Nathan Rosen. Can quantum-mechanical description of physical reality be considered complete? *Physical Review*, 47(10):777–780, 1935.

[48] Avshalom C. Elitzur, Sandu Popescu, and Daniel Rohrlich. Quantum nonlocality for each pair in an ensemble. *Physics Letters A*, 162(1):25–28, 1992.

[49] Christopher Ferrie. Quasi-probability representations of quantum theory with applications to quantum information science. *Reports on Progress in Physics*, 74(11):116001, 2011.

[50] Christopher Ferrie and Joseph Emerson. Frame representations of quantum mechanics and the necessity of negativity in quasi-probability representations. *Journal of Physics A: Mathematical and Theoretical*, 41(35):352001, 2008.

[51] Christopher Ferrie and Joseph Emerson. Framed hilbert space: hanging the quasi-probability pictures of quantum theory. *New Journal of Physics*, 11(6):063040, 2009.

[52] Isabelle Frérot, Matteo Fadel, and Maciej Lewenstein. Probing quantum correlations in many-body systems: A review of scalable methods. *Reports on Progress in Physics*, 86(11):114001, 2023.

[53] Wen ge Wang and Baowen Li. Crossover of quantum Loschmidt echo from golden-rule decay to perturbation-independent decay. *Physical Review E*, 66(5):056208, 2002.

[54] Shohini Ghose, Niel Sinclair, S. Debnath, P. Rungta, and R. Stock. Tripartite entanglement versus tripartite nonlocality in three-qubit Greenberger-Horne-Zeilinger-class states. *Physical Review Letters*, 102(25):250404, 2009.

[55] K. S. Gibbons, M. J. Hoffman, and W. K. Wootters. Discrete phase space based on finite fields. *Physical Review A*, 70(6):062101, 2004.

[56] T. Gorin, T. Prosen, T. H. Seligman, and M. Žnidarič. Dynamics of loschmidt echoes and fidelity decay. *Physics Reports*, 435(2–5):33–156, 2006.

[57] Daniel Gottesman. *Stabilizer codes and quantum error correction*. PhD thesis, California Institute of Technology, 1997.

[58] Daniel Gottesman. Fault-tolerant quantum computation with higher-dimensional systems. *Chaos, Solitons & Fractals*, 10(10):1749–1758, 1999.

[59] David Gross. Hudson's theorem for finite-dimensional quantum systems. *Journal of Mathematical Physics*, 47(12):122107, 2006.

[60] Andrzej Grudka, Karol Horodecki, Michał Horodecki, Paweł Horodecki, Ryszard Horodecki, Paweł Joshi, Waldemar Kłobus, and Anna Wójcik. Quantifying contextuality. *Physical Review Letters*, 112(12):120401, 2014.

[61] Fritz Haake, Sven Gnutzmann, and Marek Kuś. *Quantum Signatures of Chaos*. Springer, Cham, fourth edition, 2018.

[62] Fritz Haake, Małgorzata Kuś, and Rainer Scharf. Classical and quantum chaos for a kicked top. *Zeitschrift für Physik B Condensed Matter*, 65(3):381–395, 1987.

[63] Q. Y. He and M. D. Reid. Genuine multipartite Einstein–Podolsky–Rosen steering. *Physical Review Letters*, 111(25):250403, 2013.

[64] Eric J. Heller. Bound-state eigenfunctions of classically chaotic hamiltonian systems: Scars of periodic orbits. *Physical Review Letters*, 53(16):1515–1518, 1984.

[65] Tobias Holz, Hermann Kampermann, and Dagmar Bruß. Genuine multipartite Bell inequality for device-independent conference key agreement. *Physical Review Research*, 2(2):023251, 2020.

[66] Erik Hostens, Jeroen Dehaene, and Bart De Moor. Stabilizer states and clifford operations for systems of arbitrary dimensions and modular arithmetic. *Physical Review A*, 71(4):042315, 2005.

[67] Mark Howard, Joel Wallman, Victor Veitch, and Joseph Emerson. Contextuality supplies the 'magic' for quantum computation. *Nature*, 510:351–355, 2014.

[68] Ph. Jacquod and C. Petitjean. Decoherence, entanglement and irreversibility in quantum dynamical systems with few degrees of freedom. *Advances in Physics*, 58(2):67–196, 2009.

[69] R. A. Jalabert and H. M. Pastawski. Environment-independent decoherence rate in classically chaotic systems. *Physical Review Letters*, 86(12):2490–2493, 2001.

[70] Markus Jerger, Yarema Reshitnyk, Markus Oppliger, Anton Potočnik, Mintu Mondal, Andreas Wallraff, Kenneth Goodenough, Stephanie Wehner, Kristinn Juliusson, Nathan K. Langford, and Arkady Fedorov. Contextuality without nonlocality in a superconducting quantum system. *Nature Communications*, 7(1):12930, 2016.

[71] William M. Kantor. Spreads, translation planes and kerdock sets. i. *SIAM Journal on Algebraic Discrete Methods*, 3(2):151–165, 1982.

[72] Alexander A. Klyachko, M. Ali Can, Sinem Binicioğlu, and Alexander S. Shumovsky. Simple test for hidden variables in spin-1 systems. *Physical Review Letters*, 101(2):020403, 2008.

[73] Simon Kochen and Ernst P. Specker. The problem of hidden variables in quantum mechanics. *Journal of Mathematics and Mechanics*, 17(1):59–87, 1967.

[74] Johannes Kofler and Časlav Brukner. Classical world arising out of quantum physics under the restriction of coarse-grained measurements. *Physical Review Letters*, 99(18):180403, 2007.

[75] M. Kumari and Shohini Ghose. Quantum-classical correspondence in the vicinity of periodic orbits. *Physical Review E*, 97(5):052209, 2018.

[76] Ravi Kunjwal and Robert W. Spekkens. From the Kochen-Specker theorem to noncontextuality inequalities without assuming determinism. *Physical Review Letters*, 115(11):110403, 2015.

[77] Yuri A. Kuznetsov. *Elements of Applied Bifurcation Theory*, volume 112 of *Applied Mathematical Sciences*. Springer, New York, NY, 3 edition, 2004.

[78] Radek Lapkiewicz, Peizhe Li, Christoph Schaeff, Nathan K. Langford, Sven Ramelow, Marcin Wieśniak, and Anton Zeilinger. Experimental non-classicality of an indivisible quantum system. *Nature*, 474(7352):490–493, 2011.

[79] A. I. Larkin and Yu. N. Ovchinnikov. Quasiclassical method in the theory of superconductivity. *Soviet Physics JETP*, 28(6):1200–1205, 1969.

[80] Philip A. LeMaitre. Harvesting contextuality from the vacuum. *Physical Review D*, 113(4):045001, 2026.

[81] Caroline Lima, Everett Patterson, Erickson Tjoa, and Robert B. Mann. Unruh phenomena and thermalization for qudit detectors. *Physical Review D*, 108(10):105020, 2023.

[82] Caroline Lima, María Rosa Preciado-Rivas, and Sanchit Srivastava. Contextuality from quantum field vacua using qutrit Unruh–DeWitt detectors. *Physical Review D*, 113(6):065025, 2026.

[83] Feng-Li Lin and Sayantani Mondal. Entanglement harvesting and quantum discord of alpha vacua in de Sitter space. *Journal of High Energy Physics*, 2024(8):159, 2024.

[84] Juan Maldacena, Stephen H. Shenker, and Douglas Stanford. A bound on chaos. *Journal of High Energy Physics*, 2016(8):106, 2016.

[85] Alexander Mari and Jens Eisert. Positive Wigner functions render classical simulation of quantum computation efficient. *Physical Review Letters*, 109(23):230503, 2012.

[86] N. David Mermin. Extreme quantum entanglement in a superposition of macroscopically distinct states. *Physical Review Letters*, 65(15):1838–1840, 1990.

[87] N. David Mermin. Hidden variables and the two theorems of John Bell. *Reviews of Modern Physics*, 65(3):803–815, 1993.

[88] Paul A. Miller and Sarben Sarkar. Signatures of chaos in the entanglement of two coupled quantum kicked tops. *Physical Review E*, 60(2):1542–1550, 1999.

[89] Márcio G. M. Moreno, Sérgio Brito, R. Vânias Nery, and Rafael Chaves. Device-independent secret sharing and a stronger form of Bell nonlocality. *Physical Review A*, 101(5):052339, 2020.

[90] Tobias Moroder, Jean-Daniel Bancal, Yeong-Cherng Liang, Martin Hofmann, and Otfried Gühne. Device-independent entanglement quantification and related applications. *Physical Review Letters*, 111(3):030501, 2013.

[91] Gilles Murta and Francesca Baccari. Self-testing with dishonest parties and device-independent entanglement certification in quantum communication networks. *Physical Review Letters*, 131(14):140201, 2023.

[92] Michael A Nielsen and Isaac L Chuang. *Quantum computation and quantum information*. Cambridge University Press, Cambridge, 10th anniversary edition, 2010.

[93] Ron Nyström, Nicola Pranzini, and Esko Keski-Vakkuri. Harvesting magic from the vacuum. *Physical Review Research*, 7(3):033085, 2025.

[94] Edward Ott. *Chaos in Dynamical Systems*. Cambridge University Press, Cambridge, 2 edition, 2002.

[95] Hrant Pashayan, Joel J. Wallman, and Stephen D. Bartlett. Estimating outcome probabilities of quantum circuits using quasiprobabilities. *Physical Review Letters*, 115(7):070501, 2015.

[96] A. Perelomov. *Generalized Coherent States and Their Applications*. Springer, Berlin, 1986.

[97] Asher Peres. Stability of quantum motion in chaotic and regular systems. *Physical Review A*, 30(4):1610–1615, 1984.

[98] Asher Peres. Two simple proofs of the kochen-specker theorem. *Journal of Physics A: Mathematical and General*, 24(4):L175–L178, 1991.

[99] Sreeram PG, Vaibhav Madhok, and Arul Lakshminarayan. Out-of-time-ordered correlators and the Loschmidt echo in the quantum kicked top: How low can we go? *Journal of Physics D: Applied Physics*, 54(27):274004, 2021.

[100] Stefano Pironio, Antonio Acín, Serge Massar, A. Boyer de la Giroday, D. N. Matsukevich, P. Maunz, S. Olmschenk, D. Hayes, L. Luo, T. A. Manning, and C. Monroe. Random numbers certified by Bell's theorem. *Nature*, 464(7291):1021–1024, 2010.

[101] Alejandro Pozas-Kerstjens, Jorma Louko, and Eduardo Martín-Martínez. Degenerate detectors are unable to harvest spacelike entanglement. *Physical Review D*, 95(10):105009, 2017.

[102] Alejandro Pozas-Kerstjens and Eduardo Martín-Martínez. Harvesting correlations from the quantum vacuum. *Physical Review D*, 92(6):064042, 2015.

[103] J. M. Radcliffe. Some properties of coherent spin states. *Journal of Physics A: General Physics*, 4(3):313–323, 1971.

[104] Robert Raussendorf, Dan E. Browne, Nicolas Delfosse, Cihan Okay, and Juan Bermejo-Vega. Contextuality and Wigner function negativity in qubit quantum computation. *Physical Review A*, 95(5):052334, 2017.

[105] Benni Reznik. Entanglement from the vacuum. *Foundations of Physics*, 33(1):167–176, 2003.

[106] Jérémy Ribeiro, Gilles Murta, and Stephanie Wehner. Fully device-independent conference key agreement. *Physical Review A*, 97(2):022307, 2018.

[107] E. B. Rozenbaum, S. Ganeshan, and V. Galitski. Lyapunov exponent and out-of-time-ordered correlator's growth rate in a chaotic system. *Physical Review Letters*, 118(8):086801, 2017.

[108] Alejandro Satz. Then again, how often does the Unruh–DeWitt detector click if we switch it carefully? *Classical and Quantum Gravity*, 24(7):1719–1731, 2007.

[109] Valerio Scarani and Nicolas Gisin. Quantum communication between N-partners and Bell's inequalities. *Physical Review Letters*, 87(11):117901, 2001.

[110] Maximilian Schlosshauer. Decoherence, the measurement problem, and interpretations of quantum mechanics. *Reviews of Modern Physics*, 76(4):1267–1305, 2004.

[111] Erwin Schrödinger. Die gegenwärtige situation in der quantenmechanik. *Naturwissenschaften*, 23(48):807–812, 1935.

[112] Michael Seevinck and George Svetlichny. Bell-type inequalities for partial separability in N-particle systems and quantum mechanical violations. *Physical Review Letters*, 89(6):060401, 2002.

[113] Lukas M. Sieberer, Tobias Olsacher, Andreas Elben, Markus Heyl, Philipp Hauke, Fritz Haake, and Peter Zoller. Digital quantum simulation, trotter errors, and quantum chaos of the kicked top. *npj Quantum Information*, 5(1):78, 2019.

[114] Robert W. Spekkens. Contextuality for preparations, transformations, and unsharp measurements. *Physical Review A*, 71(5):052108, 2005.

[115] Robert W. Spekkens. Negativity and contextuality are equivalent notions of nonclassicality. *Physical Review Letters*, 101(2):020401, 2008.

[116] L. Sriramkumar and T. Padmanabhan. Finite-time response of inertial and uniformly accelerated Unruh–DeWitt detectors. *Classical and Quantum Gravity*, 13(8):2061–2079, 1996.

[117] Sanchit Srivastava and Shohini Ghose. Multipartite entanglement versus nonlocality for two families of N-qubit states. *Physical Review Research*, 7:033289, 2025.

[118] George Svetlichny. Distinguishing three-body from two-body nonseparability by a bell-type inequality. *Physical Review D*, 35(10):3066–3069, 1987.

[119] Erickson Tjoa and Eduardo Martín-Martínez. When entanglement harvesting is not really harvesting. *Physical Review D*, 104(12):125005, 2021.

[120] W. G. Unruh. Notes on black-hole evaporation. *Physical Review D*, 14(4):870–892, 1976.

[121] Antony Valentini. Non-local correlations in quantum electrodynamics. *Physics Letters A*, 153(6–7):321–325, 1991.

[122] Victor Veitch, Christopher Ferrie, David Gross, and Joseph Emerson. Negative quasi-probability as a resource for quantum computation. *New Journal of Physics*, 14:113011, 2012.

[123] Victor Veitch, S. A. Hamed Mousavian, Daniel Gottesman, and Joseph Emerson. The resource theory of stabilizer quantum computation. *New Journal of Physics*, 16:013009, 2014.

[124] Pauli Virtanen et al. SciPy 1.0: fundamental algorithms for scientific computing in Python. *Nature Methods*, 17:261–272, 2020.

[125] John von Neumann. *Mathematical Foundations of Quantum Mechanics*. Princeton University Press, Princeton, 1955. Translated by Robert T. Beyer.

[126] Rui-Di Wang, Shu-Min Wu, and Xiao-Li Huang. Nonlocal coherence harvesting from quantum vacuum. *Communications in Theoretical Physics*, 76(7):075103, 2024.

[127] Reinhard F. Werner. Quantum states with Einstein–Podolsky–Rosen correlations admitting a hidden-variable model. *Physical Review A*, 40(8):4277–4281, 1989.

[128] Eugene Wigner. On the quantum correction for thermodynamic equilibrium. *Physical Review*, 40(5):749–759, 1932.

[129] Alexander Wong and Nathaniel Christensen. Potential multiparticle entanglement measure. *Physical Review A*, 63(4):044301, 2001.

[130] William K. Wootters. A wigner-function formulation of finite-state quantum mechanics. *Annals of Physics*, 176(1):1–21, 1987.

[131] William K. Wootters. Entanglement of formation of an arbitrary state of two qubits. *Physical Review Letters*, 80(10):2245–2248, 1998.

[132] William K. Wootters and Brian D. Fields. Optimal state-determination by mutually unbiased measurements. *Annals of Physics*, 191(2):363–381, 1989.

[133] Shu-Min Wu, Rui-Di Wang, Xiao-Li Huang, and Zejun Wang. Harvesting asymmetric steering via non-identical detectors. *European Physical Journal C*, 85:708, 2025.

[134] Youwang Xiao, Zong Wang, Wen-Na Zhao, and Ming Li. Tight upper bound for the maximal expectation value of the N-partite generalized Svetlichny operator. *Advanced Quantum Technologies*, 7(6):2400101, 2024.

[135] Sixia Yu and C. H. Oh. State-independent proof of Kochen-Specker theorem with 13 rays. *Physical Review Letters*, 108(3):030402, 2012.

[136] Huangjun Zhu. Permutation symmetry determines the discrete wigner function. *Physical Review Letters*, 116(4):040501, 2016.

[137] Michał Żukowski, Časlav Brukner, Wiesław Laskowski, and Marek Wiśniak. Do all pure entangled states violate Bell's inequalities for correlation functions? *Physical Review Letters*, 88(21):210402, 2002.

[138] Wojciech H. Zurek. Decoherence, einselection, and the quantum origins of the classical. *Reviews of Modern Physics*, 75(3):715–775, 2003.

APPENDICES

Appendix A

Supplementary Material: Derivations for Chapter 3

This appendix provides self-contained derivations of the measurement-optimized Svetlichny values quoted in Eqs. (3.14) and (3.16). The material closely follows our published analysis [117], but is reproduced here so the thesis is self-contained.

Throughout, each local projective observable is written as

$$A = \mathbf{v} \cdot \boldsymbol{\sigma} = \sin\theta\cos\phi\,\sigma_x + \sin\theta\sin\phi\,\sigma_y + \cos\theta\,\sigma_z, \tag{A.1}$$

with a unit Bloch vector $\mathbf{v}$ and Pauli vector $\boldsymbol{\sigma} = (\sigma_x, \sigma_y, \sigma_z)$. We will repeatedly use the computational-basis matrix elements

$$\langle 0|A|0\rangle = \cos\theta, \qquad \langle 1|A|1\rangle = -\cos\theta, \tag{A.2}$$

$$\langle 0|A|1\rangle = \sin\theta\, e^{-i\phi}, \qquad \langle 1|A|0\rangle = \sin\theta\, e^{+i\phi}. \tag{A.3}$$

For N parties and a bit string $\mathbf{x} = (x_1, \ldots, x_N)$, we use the shorthand

$$A(\mathbf{x}) := A_1^{x_1} \otimes \cdots \otimes A_N^{x_N}, \qquad w(\mathbf{x}) := \sum_{i=1}^{N} x_i, \tag{A.4}$$

and the Svetlichny coefficients $\nu^{\pm}(\mathbf{x})$ as defined in Eq. (3.7).

A.1 Derivation for GGHZ states

We now reproduce the derivation of the measurement-optimized Svetlichny value for the generalized GHZ (GGHZ) family.

A.1.1 Bloch parametrization and the F/G decomposition

Each local observable is written as $A_i^{x_i} = \mathbf{v}_i^{x_i} \cdot \boldsymbol{\sigma}$ with Bloch-sphere angles

$$\mathbf{v}_i^{x_i} = (\sin\theta_i^{x_i}\cos\phi_i^{x_i}, \sin\theta_i^{x_i}\sin\phi_i^{x_i}, \cos\theta_i^{x_i}). \tag{A.5}$$

For the GGHZ state

$$|\psi_g(\alpha)\rangle = \cos\alpha\,|0\rangle^{\otimes N} + \sin\alpha\,|1\rangle^{\otimes N}, \tag{A.6}$$

we first evaluate the N-body correlator $\langle A(\mathbf{x})\rangle_{\psi_g}$. Using Eqs. (A.2)–(A.3) and the product structure of $A(\mathbf{x})$, we obtain

$$\langle 0^{\otimes N}|A(\mathbf{x})|0^{\otimes N}\rangle = \prod_{i=1}^{N}\cos\theta_i^{x_i}, \tag{A.7}$$

$$\langle 1^{\otimes N}|A(\mathbf{x})|1^{\otimes N}\rangle = \prod_{i=1}^{N}(-\cos\theta_i^{x_i}) = (-1)^N\prod_{i=1}^{N}\cos\theta_i^{x_i}, \tag{A.8}$$

$$\langle 0^{\otimes N}|A(\mathbf{x})|1^{\otimes N}\rangle = \prod_{i=1}^{N}\sin\theta_i^{x_i}e^{-i\phi_i^{x_i}} = e^{-i\sum_i\phi_i^{x_i}}\prod_{i=1}^{N}\sin\theta_i^{x_i}, \tag{A.9}$$

$$\langle 1^{\otimes N}|A(\mathbf{x})|0^{\otimes N}\rangle = e^{+i\sum_i\phi_i^{x_i}}\prod_{i=1}^{N}\sin\theta_i^{x_i}. \tag{A.10}$$

Therefore,

$$\begin{aligned}\langle A(\mathbf{x})\rangle_{\psi_g} &= \cos^2\alpha\,\langle 0^{\otimes N}|A(\mathbf{x})|0^{\otimes N}\rangle + \sin^2\alpha\,\langle 1^{\otimes N}|A(\mathbf{x})|1^{\otimes N}\rangle \\ &\quad + \sin\alpha\cos\alpha\left(\langle 0^{\otimes N}|A(\mathbf{x})|1^{\otimes N}\rangle + \langle 1^{\otimes N}|A(\mathbf{x})|0^{\otimes N}\rangle\right) \\ &= \left(\cos^2\alpha + (-1)^N\sin^2\alpha\right)\prod_{i=1}^{N}\cos\theta_i^{x_i} + \sin(2\alpha)\cos\Big(\sum_{i=1}^{N}\phi_i^{x_i}\Big)\prod_{i=1}^{N}\sin\theta_i^{x_i}.\end{aligned} \tag{A.11}$$

Plugging Eq. (A.11) into the Svetlichny sum in Eq. (3.6) yields

$$\left|\langle S_N^{\pm}\rangle\right| = \left|c_1F_N^{\pm} + c_2G_N^{\pm}\right|, \tag{A.12}$$

where

$$c_1 = \cos^2\alpha + (-1)^N\sin^2\alpha, \tag{A.13}$$

$$c_2 = \sin(2\alpha), \tag{A.14}$$

and

$$F_N^{\pm} = \sum_{\mathbf{x}\in\{0,1\}^N} \nu^{\pm}(\mathbf{x}) \prod_{i=1}^{N} \cos\theta_i^{x_i}, \tag{A.15}$$

$$G_N^{\pm} = \sum_{\mathbf{x}\in\{0,1\}^N} \nu^{\pm}(\mathbf{x}) \cos\Big(\sum_{i=1}^{N} \phi_i^{x_i}\Big) \prod_{i=1}^{N} \sin\theta_i^{x_i}. \tag{A.16}$$

A.1.2 Maximizing the "classical" branch $|F_N^{\pm}|$

When $\alpha \in \{0, \pi/2\}$, one has $c_2 = 0$ and the state becomes a product state. Then $\left|\langle S_N^{\pm}\rangle\right| = |F_N^{\pm}|$. Choosing all measurements along the Z axis (all $\theta_i^{x_i} \in \{0, \pi\}$) implies $\sin\theta_i^{x_i} = 0$ and hence $G_N^{\pm} = 0$. Moreover, by choosing $\theta_i^{x_i} = 0$ for all i, x_i we have $\cos\theta_i^{x_i} = 1$ so that

$$F_N^{\pm} = \sum_{\mathbf{x}} \nu^{\pm}(\mathbf{x}) = \sum_{k=0}^{N} \binom{N}{k} (-1)^{k(k\pm1)/2}. \tag{A.17}$$

To evaluate the sum, use the trigonometric representation (valid because $\nu^{\pm}(\mathbf{x}) \in \{\pm1\}$)

$$\nu^{\pm}(\mathbf{x}) = \sqrt{2}\,\cos\left(\pm\frac{\pi}{4} + w(\mathbf{x})\frac{\pi}{2}\right). \tag{A.18}$$

Inserting Eq. (A.18) and grouping by weight $k = w(\mathbf{x})$ gives

$$\begin{aligned}\sum_{\mathbf{x}} \nu^{\pm}(\mathbf{x}) &= \sqrt{2}\sum_{k=0}^{N} \binom{N}{k} \cos\left(\pm\frac{\pi}{4} + k\frac{\pi}{2}\right) \\ &= \sqrt{2}\,\Re\left[e^{\pm i\pi/4}\sum_{k=0}^{N}\binom{N}{k} e^{ik\pi/2}\right] = \sqrt{2}\,\Re\left[e^{\pm i\pi/4}(1+i)^N\right].\end{aligned} \tag{A.19}$$

Since $(1+i)^N = 2^{N/2}e^{iN\pi/4}$, Eq. (A.19) becomes

$$\sum_{\mathbf{x}} \nu^{\pm}(\mathbf{x}) = \sqrt{2}\,2^{N/2}\cos\left(\frac{(N\pm1)\pi}{4}\right), \tag{A.20}$$

whose magnitude is $2^{(N+1)/2}$ for odd N and $2^{N/2}$ for even N. Hence

$$|F_N^{\pm}|_{\max} = \left|\sum_{k=0}^{N}(-1)^{k(k\pm1)/2}\binom{N}{k}\right| = \begin{cases} 2^{\frac{N+1}{2}}, & N \text{ odd}, \\ 2^{\frac{N}{2}}, & N \text{ even}. \end{cases} \tag{A.21}$$

This value is achieved by Z-axis measurements (and is also the best value attainable by local-hidden-variable models).

A.1.3 Maximizing the "GHZ interference" branch $|G_N^{\pm}|$

When $\alpha = \pi/4$, the state is the maximally entangled GHZ state. In this case the optimum can be achieved with equatorial measurements (all $\theta_i^{x_i} = \pi/2$) so that $\cos\theta_i^{x_i} = 0$ and hence $F_N^{\pm} = 0$, while $\sin\theta_i^{x_i} = 1$. Then

$$G_N^{\pm} = \sum_{\mathbf{x}} \nu^{\pm}(\mathbf{x}) \cos\Big(\sum_i \phi_i^{x_i}\Big). \tag{A.22}$$

Using Eq. (A.18), we choose azimuthal angles so that for every bit string $\mathbf{x}$,

$$\sum_{i=1}^{N} \phi_i^{x_i} = \pm\frac{\pi}{4} + w(\mathbf{x})\frac{\pi}{2} \pmod{2\pi}. \tag{A.23}$$

One explicit choice is

$$\phi_1^0 = \phi_1^1 = \pm\frac{\pi}{4}, \qquad \phi_i^0 = 0,\ \phi_i^1 = \frac{\pi}{2} \text{ for } i = 2, \ldots, N. \tag{A.24}$$

With this assignment, $\sum_i \phi_i^{x_i} = \pm\pi/4 + w(\mathbf{x})\pi/2$ and hence

$$\cos\Big(\sum_i \phi_i^{x_i}\Big) = \frac{\nu^{\pm}(\mathbf{x})}{\sqrt{2}}. \tag{A.25}$$

Therefore each summand equals $\nu^{\pm}(\mathbf{x}) \cdot \nu^{\pm}(\mathbf{x})/\sqrt{2} = 1/\sqrt{2}$, and summing over 2^N strings gives

$$|G_N^{\pm}|_{\max} = \sqrt{2}\, 2^{N-1}. \tag{A.26}$$

A.1.4 Global maximum over all measurements for general α

For general α, the goal is to maximize $|c_1 F_N^{\pm} + c_2 G_N^{\pm}|$ over all local angles. The two measurement strategies from the previous subsections provide two candidate extrema:

1. Z-axis strategies maximize $|F_N^{\pm}|$ and set $G_N^{\pm} = 0$.
2. Equatorial strategies maximize $|G_N^{\pm}|$ and set $F_N^{\pm} = 0$.

We now show (following the constructive argument in [117]) that for $N > 2$ no other choice of measurements can exceed the larger of these two extrema.

Isolating the last two parties

Without loss of generality, isolate parties $N-1$ and N and group the Svetlichny sum so that the remaining $N-2$ parties appear only through F_{N-2}-type and G_{N-2}-type expressions. One can write

$$\begin{aligned}\left|\langle S_N^{\pm}\rangle\right| = \big| & f_1^{\pm}\cos\theta_{N-1}^0\cos\theta_N^0 + g_1^{\pm}\sin\theta_{N-1}^0\sin\theta_N^0 \\ & + f_2^{\pm}\cos\theta_{N-1}^0\cos\theta_N^1 + g_2^{\pm}\sin\theta_{N-1}^0\sin\theta_N^1 \\ & + f_3^{\pm}\cos\theta_{N-1}^1\cos\theta_N^0 + g_3^{\pm}\sin\theta_{N-1}^1\sin\theta_N^0 \\ & + f_4^{\pm}\cos\theta_{N-1}^1\cos\theta_N^1 + g_4^{\pm}\sin\theta_{N-1}^1\sin\theta_N^1\big|,\end{aligned} \tag{A.27}$$

where the coefficients depend only on the first $N-2$ parties and on azimuthal phases. Concretely, defining c_1, c_2 as in Eqs. (A.13)–(A.14), one can take

$$\begin{aligned} f_1^{\pm} &= c_1 F_{N-2}^{\pm}, & g_1^{\pm} &= c_2\,\tilde{G}_{00,N-2}^{\pm}, \\ f_2^{\pm} &= \pm c_1 F_{N-2}^{\mp}, & g_2^{\pm} &= \pm c_2\,\tilde{G}_{01,N-2}^{\mp}, \\ f_3^{\pm} &= \pm c_1 F_{N-2}^{\mp}, & g_3^{\pm} &= \pm c_2\,\tilde{G}_{10,N-2}^{\mp}, \\ f_4^{\pm} &= -c_1 F_{N-2}^{\pm}, & g_4^{\pm} &= -c_2\,\tilde{G}_{11,N-2}^{\pm}. \end{aligned} \tag{A.28}$$

Here $\tilde{G}_{ij,N-2}^{\pm}$ has the same form as $G_{N-2}^{\pm}$ in Eq. (A.16), but with $\phi_{N-1}^i + \phi_N^j$ added to the cosine argument. (Equivalently, it is the G-type expression for $N-2$ parties with a shifted global phase.)

Bounding the dependence on θ_N^0, θ_N^1

Apply the elementary inequality

$$x\cos\vartheta + y\sin\vartheta \le \sqrt{x^2+y^2} \tag{A.29}$$

to the pairs of terms involving θ_N^0 and θ_N^1 in Eq. (A.27). This yields

$$\begin{aligned}|\langle S_N^{\pm}\rangle| \le & \sqrt{(f_1^{\pm})^2\cos^2\theta_{N-1}^0 + (g_1^{\pm})^2\sin^2\theta_{N-1}^0} + \sqrt{(f_2^{\pm})^2\cos^2\theta_{N-1}^0 + (g_2^{\pm})^2\sin^2\theta_{N-1}^0} \\ & + \sqrt{(f_3^{\pm})^2\cos^2\theta_{N-1}^1 + (g_3^{\pm})^2\sin^2\theta_{N-1}^1} + \sqrt{(f_4^{\pm})^2\cos^2\theta_{N-1}^1 + (g_4^{\pm})^2\sin^2\theta_{N-1}^1}.\end{aligned} \tag{A.30}$$

The bound is tight: Eq. (A.29) is an equality when $\tan\vartheta = y/x$. Enforcing equality simultaneously for the four applications of Eq. (A.29) imposes the (paper's) consistency equations

$$\begin{aligned} \tan\theta_N^0 &= \tan\theta_{N-1}^0 \frac{g_1^\pm}{f_1^\pm}, \quad \tan\theta_N^0 = \tan\theta_{N-1}^1 \frac{g_2^\pm}{f_2^\pm}, \\ \tan\theta_N^1 &= \tan\theta_{N-1}^0 \frac{g_3^\pm}{f_3^\pm}, \quad \tan\theta_N^1 = \tan\theta_{N-1}^1 \frac{g_4^\pm}{f_4^\pm}. \end{aligned} \tag{A.31}$$

We will choose angles so that Eq. (A.31) is satisfied, ensuring that the inequality steps do not introduce looseness.

Maximizing over θ_{N-1}^0 and θ_{N-1}^1

Define the partial sums

$$H_N^\pm(\theta_{N-1}^0) := \sqrt{(f_1^\pm)^2\cos^2\theta_{N-1}^0 + (g_1^\pm)^2\sin^2\theta_{N-1}^0} + \sqrt{(f_2^\pm)^2\cos^2\theta_{N-1}^0 + (g_2^\pm)^2\sin^2\theta_{N-1}^0}, \tag{A.32}$$

$$K_N^\pm(\theta_{N-1}^1) := \sqrt{(f_3^\pm)^2\cos^2\theta_{N-1}^1 + (g_3^\pm)^2\sin^2\theta_{N-1}^1} + \sqrt{(f_4^\pm)^2\cos^2\theta_{N-1}^1 + (g_4^\pm)^2\sin^2\theta_{N-1}^1}. \tag{A.33}$$

Then Eq. (A.30) becomes

$$|\langle S_N^\pm\rangle| \le H_N^\pm(\theta_{N-1}^0) + K_N^\pm(\theta_{N-1}^1). \tag{A.34}$$

By direct differentiation, $H_N^\pm(\theta)$ attains its maxima at $\theta \in \{0, \pi/2\}$, yielding

$$\max_{\theta_{N-1}^0} H_N^\pm = \max\big\{|f_1^\pm| + |f_2^\pm|,\ |g_1^\pm| + |g_2^\pm|\big\}. \tag{A.35}$$

The same holds for $K_N^\pm$. Moreover, by symmetry of the Svetlichny coefficients under exchanging the last two parties, the two maxima coincide:

$$\max H_N^\pm = \max K_N^\pm. \tag{A.36}$$

Consequently,

$$|\langle S_N^\pm\rangle| \le 2\max H_N^\pm. \tag{A.37}$$

It remains to evaluate $\max H_N^\pm$.

Evaluating the two competing branches

Using Eq. (A.28), the "f-branch" in Eq. (A.35) can be bounded as

$$|f_1^{\pm}| + |f_2^{\pm}| = |c_1|\left(|F_{N-2}^{\pm}| + |F_{N-2}^{\mp}|\right) \le 2|c_1|\,|F_{N-2}^{\pm}|_{\max}. \tag{A.38}$$

One can in fact choose measurements on the first $N-2$ parties so that this reaches $|c_1|\,|F_N^{\pm}|_{\max}$, reproducing Eq. (A.21) with N parties. Thus the best achievable f-branch contribution is

$$f_{\max} := \max(|f_1^{\pm}| + |f_2^{\pm}|) = |c_1|\,|F_N^{\pm}|_{\max}. \tag{A.39}$$

Similarly, by choosing azimuthal phases so that the shifted expressions $\tilde{G}_{00,N-2}^{\pm}$ and $\tilde{G}_{01,N-2}^{\mp}$ are maximized with the same sign, one obtains

$$g_{\max} := \max(|g_1^{\pm}| + |g_2^{\pm}|) = |c_2|\,|G_N^{\pm}|_{\max}. \tag{A.40}$$

Therefore

$$\max H_N^{\pm} = \max\{f_{\max}, g_{\max}\} = \max\left\{|c_1|\,|F_N^{\pm}|_{\max},\ |c_2|\,|G_N^{\pm}|_{\max}\right\}. \tag{A.41}$$

Substituting this into Eq. (A.37) shows that

$$\left|\langle S_N^{\pm}\rangle\right|_{\max} = \max\left\{|c_1|\,|F_N^{\pm}|_{\max},\ |c_2|\,|G_N^{\pm}|_{\max}\right\}. \tag{A.42}$$

Finally, inserting Eqs. (A.21) and (A.26) and simplifying gives the closed forms quoted in the chapter. For completeness, we record them here.

For odd $N > 2$ (where $|c_1| = |\cos(2\alpha)|$),

$$S_{N,\max}^{\pm}(\psi_g) = \begin{cases} 2^{\frac{N+1}{2}}\,|\cos(2\alpha)|, & |\tan(2\alpha)| \le 2^{1-\frac{N}{2}}, \\ \sqrt{2}\,2^{N-1}\,|\sin(2\alpha)|, & |\tan(2\alpha)| \ge 2^{1-\frac{N}{2}}. \end{cases} \tag{A.43}$$

For even $N > 2$ (where $|c_1| = 1$),

$$S_{N,\max}^{\pm}(\psi_g) = \begin{cases} 2^{\frac{N}{2}}, & |\sin(2\alpha)| \le 2^{\frac{1-N}{2}}, \\ \sqrt{2}\,2^{N-1}\,|\sin(2\alpha)|, & |\sin(2\alpha)| \ge 2^{\frac{1-N}{2}}. \end{cases} \tag{A.44}$$

Using $\tau_n(\psi_g) = \sin^2(2\alpha)$ for even N yields Eq. (3.14) in the main text.

For even N, $|c_1| = 1$ and $|c_2| = |\sin(2\alpha)|$. Substituting Eqs. (A.21) and (A.26) yields

$$S_{N,\max}^{\pm}(\psi_g) = \begin{cases} 2^{\frac{N}{2}}, & |\sin(2\alpha)| \le 2^{\frac{1-N}{2}}, \\ \sqrt{2}\,2^{N-1}|\sin(2\alpha)|, & |\sin(2\alpha)| \ge 2^{\frac{1-N}{2}}. \end{cases} \tag{A.45}$$

Finally, using $\tau_n(\psi_g) = \sin^2(2\alpha)$ gives Eq. (3.14).

A.2 Derivation for maximal slice states

We now reproduce the derivation of the maximum Svetlichny value for maximal slice states. The goal is to show that the measurement optimization can be carried out analytically and yields the closed form in Eq. (3.16).

A.2.1 Rewriting $S_N^{\pm}$ by isolating the last two parties

Let $\tilde{\mathbf{x}} \in \{0,1\}^{N-2}$ denote a bit string for the first $N-2$ parties. Define

$$A(\tilde{\mathbf{x}}) := \bigotimes_{i=1}^{N-2} A_i^{\tilde{x}_i}. \tag{A.46}$$

Then $S_N^{\pm}$ can be rearranged into two sums (the same algebraic grouping as in our paper):

$$\begin{aligned} S_N^{\pm} = &\sum_{\tilde{\mathbf{x}}} \nu^{\pm}(\tilde{\mathbf{x}})\, A(\tilde{\mathbf{x}}) \left(A_{N-1}^0 + (-1)^{w(\tilde{\mathbf{x}})} A_{N-1}^1\right) A_N^0 \\ &+ \sum_{\tilde{\mathbf{x}}} \nu^{\pm}(\tilde{\mathbf{x}})\, A(\tilde{\mathbf{x}}) \left((-1)^{w(\tilde{\mathbf{x}})} A_{N-1}^0 - A_{N-1}^1\right) A_N^1. \end{aligned} \tag{A.47}$$

A.2.2 Orthogonal directions for party $N-1$

Write $A_{N-1}^x = \mathbf{v}_{N-1}^x \cdot \boldsymbol{\sigma}$. Introduce two unit vectors $\mathbf{b}_0, \mathbf{b}_1$ and an angle θ such that

$$\mathbf{v}_{N-1}^0 + \mathbf{v}_{N-1}^1 = 2\cos\theta\, \mathbf{b}_0, \qquad \mathbf{v}_{N-1}^0 - \mathbf{v}_{N-1}^1 = 2\sin\theta\, \mathbf{b}_1, \tag{A.48}$$

which implies the orthogonality constraint $\mathbf{b}_0 \cdot \mathbf{b}_1 = 0$. Define the associated observables $B_k := \mathbf{b}_k \cdot \boldsymbol{\sigma}$ for $k \in \{0,1\}$.

A.2.3 Reducing to a sum of square roots

Using Eq. (A.47) and Eq. (A.48), the expectation value can be bounded by repeated application of

$$x\cos\theta + y\sin\theta \le \sqrt{x^2+y^2}. \tag{A.49}$$

A convenient way to write the result is to split $\tilde{\mathbf{x}}$ by parity of the Hamming weight. Let $\tilde{\mathbf{x}}_e$ range over even weight and $\tilde{\mathbf{x}}_o$ over odd weight. Then one obtains

$$\langle S_N^{\pm}\rangle \leq 2\sum_{\tilde{\mathbf{x}}_e}\sqrt{\langle A(\tilde{\mathbf{x}}_e)B_0A_N^0\rangle^2+\langle A(\tilde{\mathbf{x}}_e)B_1A_N^1\rangle^2}+2\sum_{\tilde{\mathbf{x}}_o}\sqrt{\langle A(\tilde{\mathbf{x}}_o)B_1A_N^0\rangle^2+\langle A(\tilde{\mathbf{x}}_o)B_0A_N^1\rangle^2}, \tag{A.50}$$

where all expectation values are taken with respect to $|\psi_s(\alpha)\rangle$.

A.2.4 Bounding the correlators on the maximal slice state

Write the maximal slice state as

$$|\psi_s(\alpha)\rangle = \frac{1}{\sqrt{2}}\Big(|0\rangle^{\otimes N}+|1\rangle^{\otimes(N-1)}(\cos\alpha\,|0\rangle+\sin\alpha\,|1\rangle)\Big). \tag{A.51}$$

For the correlators in Eq. (A.50), define the accumulated azimuthal phase from the first $N-2$ parties

$$\Phi(\tilde{\mathbf{x}}) := \sum_{i=1}^{N-2}\phi_i^{\tilde{x}_i}. \tag{A.52}$$

Using the basis-element identities in Eqs. (A.2)–(A.3), one can evaluate

$$\langle\psi_s|A(\tilde{\mathbf{x}})B_kA_N^l|\psi_s\rangle \tag{A.53}$$

as a sum of diagonal terms (from $|0^{\otimes N}\rangle$ and $|1^{\otimes N}\rangle$ components) and interference terms. Carrying out this expansion and then applying Eq. (A.49) twice (once to eliminate the dependence on the polar angle of B_k and once for the polar angle of A_N^l) yields the bound (as in [117])

$$\langle\psi_s|A(\tilde{\mathbf{x}})B_kA_N^l|\psi_s\rangle \leq \Big(\cos^2\alpha\,\cos^2\big(\Phi(\tilde{\mathbf{x}})+\phi_{b,k}\big)+\sin^2\alpha\,\cos^2\big(\Phi(\tilde{\mathbf{x}})+\phi_{b,k}+\phi_{N,l}\big)\Big)^{1/2}, \tag{A.54}$$

where $\phi_{b,k}$ is the azimuthal angle of $\mathbf{b}_k$ and $\phi_{N,l}$ is the azimuthal angle of the lth measurement setting on party N. The right-hand side of Eq. (A.54) is maximized by taking all measurements of parties $1,\ldots,N-2$ in the equatorial plane, i.e.

$$\theta_i^{\tilde{x}_i} = \frac{\pi}{2} \qquad (i=1,\ldots,N-2), \tag{A.55}$$

so that all factors $\sin\theta_i^{\tilde{x}_i}=1$ that appear in the interference contributions are maximal.

A.2.5 Phase choices, saturation, and the final maximum

The bound in Eq. (A.50) is tight. Choose azimuthal angles so that $\cos^2\big(\Phi(\tilde{\mathbf{x}})+\phi_{b,k}+\phi_{N,l}\big) = 1$ for all $\tilde{\mathbf{x}}$, k, and l, while maintaining $\mathbf{b}_0 \cdot \mathbf{b}_1 = 0$ (equivalently, an azimuthal separation of $\pi/2$ between $\mathbf{b}_0$ and $\mathbf{b}_1$). Concretely, one may choose $\phi_{b,1} = \phi_{b,0} + \pi/2$ and then pick the phases $\{\phi_i^{x_i}\}$ and $\{\phi_{N,l}\}$ so that

$$\Phi(\tilde{\mathbf{x}}) + \phi_{b,k} + \phi_{N,l} \equiv 0 \pmod{\pi} \tag{A.56}$$

for each of the four combinations $(k,l) \in \{0,1\} \times \{0,1\}$ appearing in Eq. (A.50). With these phase choices, Eq. (A.54) implies that each correlator entering the square roots takes the same extremal value, and each square root in Eq. (A.50) becomes the same constant,

$$\sqrt{\cos^2\alpha + \sin^2\alpha \cdot 2} = \sqrt{1+\sin^2\alpha}, \tag{A.57}$$

and there are 2^{N-2} bit strings $\tilde{\mathbf{x}}$. Hence

$$S^{\pm}_{N,\max}(\psi_s) = 2^{N-1}\sqrt{1+\sin^2\alpha}. \tag{A.58}$$

The derivation above does not depend on the parity of N, so the same closed form holds for both even and odd $N > 2$. Finally, for even N we rewrite the result in terms of the n-tangle $\tau_n(\psi_s) = \sin^2\alpha$ to obtain

$$S^{\pm}_{N,\max}(\psi_s) = 2^{N-1}\sqrt{1+\tau_n(\psi_s)}, \tag{A.59}$$

which is Eq. (3.16).

Appendix B

Supplementary Material for Chapter 5

B.1 Heisenberg–Weyl internal dynamics

This appendix collects the perturbative density-matrix expressions specific to Heisenberg–Weyl (HW) internal detector dynamics, following Ref. [82] (Appendix A). Unlike the SU(2) qutrit, the HW detector has a degenerate excited manifold and no superselection rules, so additional coherences appear already at $O(\lambda^2)$.

B.1.1 Additional local coherence integral

In addition to the integrals L, L_{ab}, Q, and M_{ab} defined in Eqs. (5.10)–(5.12), HW dynamics introduces an additional local coherence coefficient V. Following Ref. [82] (Appendix A), it can be written as

$$V = -\lambda^2 \int d^4x\, d^4x'\, \Lambda_a(x)\Lambda_a(x')\, e^{i\Omega t'}\, \Theta(t-t')\, W(x,x'), \tag{B.1}$$

where $W(x,x')$ is the Wightman function. For the Gaussian switching and spherical smearing used in this chapter, V reduces to the one-dimensional integral in Eq. (B.10).

B.1.2 Two-detector state for HW dynamics

At $O(\lambda^2)$, the final two-detector state (in the ordered product basis of Eq. (5.16)) has the same nonlocal single-excitation structure controlled by L and L_{ab} as in Eq. (5.16), but a richer set of local coherences. For completeness, we record the explicit matrix form (Ref. [82], Appendix A),

$$\rho_d = \begin{pmatrix} 1-4L & V^* & V^* & V^* & M_{ab}^* & M_{ab}^* & V^* & M_{ab}^* & M_{ab}^* \\ V & L & L & L_{ab} & 0 & 0 & L_{ab} & 0 & 0 \\ V & L & L & L_{ab} & 0 & 0 & L_{ab} & 0 & 0 \\ V & L_{ab} & L_{ab} & L & 0 & 0 & L & 0 & 0 \\ M_{ab} & 0 & 0 & 0 & 0 & 0 & 0 & 0 & 0 \\ M_{ab} & 0 & 0 & 0 & 0 & 0 & 0 & 0 & 0 \\ V & L_{ab} & L_{ab} & L & 0 & 0 & L & 0 & 0 \\ M_{ab} & 0 & 0 & 0 & 0 & 0 & 0 & 0 & 0 \\ M_{ab} & 0 & 0 & 0 & 0 & 0 & 0 & 0 & 0 \end{pmatrix} + O(\lambda^4), \tag{B.2}$$

The key qualitative change relative to SU(2) is that V generates coherence between the ground and both excited levels already at leading order, due to the absence of superselection rules and the degenerate excited manifold.

B.1.3 Reduced single-detector state for HW dynamics

Tracing out detector b yields the reduced state

$$\rho_a = \begin{pmatrix} 1-2L & V^* & V^* \\ V & L & L \\ V & L & L \end{pmatrix}, \tag{B.3}$$

which should be compared with the SU(2) reduced state in Eq. (5.25). In HW dynamics, both excited states are populated equally at this order (diagonal entries L) and are mutually coherent (entry L), reflecting the degenerate excited manifold.

B.1.4 Wigner-negativity conditions

In the $d = 3$ discrete Wigner representation, Wigner negativity is again controlled by the balance of excitation scale and coherence. For HW dynamics one obtains inequalities analogous to Eqs. (5.26)–(5.28), with the SU(2) coherence parameter Q replaced by its HW analogue V. This replacement rule is the practical reason V is the key additional coefficient for comparing contextuality-generation efficiency across internal dynamics.

B.2 Closed-form integrals for the detector state

This appendix records the closed-form one-dimensional integral expressions used to evaluate the perturbative matrix elements defining the final detector state (following Ref. [82], Appendix B). For compactness we introduce the dimensionless parameters

$$\widetilde{R} = \frac{R}{T}, \qquad \widetilde{d} = \frac{d}{T}, \qquad \omega = \Omega T, \qquad \alpha = \frac{9\lambda^2}{4\pi \widetilde{R}^2}. \tag{B.4}$$

Let $j_\ell(z)$ denote the spherical Bessel functions ($j_0(z) = \sin z/z$ and $j_1(z) = \sin z/z^2 - \cos z/z$). Let $w(z)$ denote the Faddeeva function, which can be defined by

$$w(z) = e^{-z^2}\ \mathrm{erfc}(-iz). \tag{B.5}$$

With these conventions, the integral expressions used in the numerical evaluation are (matching the matrix elements L, L_{ab}, Q, M_{ab}, and V used throughout the main text via $L = \mathcal{L}$, $L_{ab} = \mathcal{L}_{ab}$, $Q = \mathcal{Q}$, $M_{ab} = \mathcal{M}_{ab}$, and $V = \mathcal{V}$).

$$\mathcal{L} = \alpha \int_0^\infty \frac{\mathrm{d}k}{k}\ j_1^2(k\widetilde{R})\ e^{-\frac{1}{2}(k+\omega)^2}, \tag{B.6}$$

$$\mathcal{L}_{ab} = \alpha \int_0^\infty \frac{\mathrm{d}k}{k}\ j_1^2(k\widetilde{R})\ e^{-\frac{1}{2}(k+\omega)^2}\ j_0(k\widetilde{d}), \tag{B.7}$$

$$\mathcal{Q} = -\frac{\alpha}{2} e^{-\frac{1}{2}\omega^2} \int_0^\infty \frac{\mathrm{d}k}{k}\ j_1^2(k\widetilde{R})\ w\!\left(-\frac{k}{\sqrt{2}}\right), \tag{B.8}$$

$$\mathcal{M}_{ab} = -\alpha e^{-\frac{1}{2}\omega^2} \int_0^\infty \frac{\mathrm{d}k}{k}\ j_1^2(k\widetilde{R})\ w\!\left(-\frac{k}{\sqrt{2}}\right)\ j_0(k\widetilde{d}), \tag{B.9}$$

$$\mathcal{V} = \frac{\alpha}{2} e^{-\frac{1}{8}\omega^2} \int_0^\infty \frac{\mathrm{d}k}{k}\ j_1^2(k\widetilde{R})\ w\!\left[\frac{1}{\sqrt{2}}\left(\frac{\omega}{2} - k\right)\right]. \tag{B.10}$$

Appendix C

Supplementary Material for Chapter 6

This appendix records geometric statements associated with the logical Bell inequalities of Chapter 6. These results support the main narrative but are not needed for the marginal LBI–Wigner-negativity equivalence.

C.1 Two-Qudit Contexts: Explicit Enumeration (Optional)

Chapter 6 uses the standard measurement cover by *all* maximal commuting subsets (maximal contexts) of the phase-free two-qudit Heisenberg–Weyl group. This section records an explicit way to enumerate these contexts and to count them. It is included mainly for completeness; the main chapter only needs that such a cover exists, and that it supports the usual "product rule" constraints for commuting Weyl operators.

Throughout, d is an odd prime. For a single qudit, recall the $d+1$ distinguished stabilizer settings

$$M = \{Z, X, XZ, XZ^2, \ldots, XZ^{d-1}\}, \tag{C.1}$$

whose eigenbases form a complete set of mutually unbiased bases.

C.1.1 Separable (product) contexts

For $A, B \in M$, the two commuting operators $A \otimes I$ and $I \otimes B$ generate a maximal abelian subgroup. We write

$$C_{AB} := \langle A \otimes I,\ I \otimes B \rangle. \tag{C.2}$$

These are the separable contexts. There are $(d+1)^2$ such contexts, one for each ordered pair (A, B).

C.1.2 Entangled contexts

The remaining maximal contexts stabilize entangled two-qudit stabilizer bases. One convenient parametrization is the following. Consider observables of the form

$$A \otimes X^p \quad \text{and} \quad B \otimes Z^q, \tag{C.3}$$

where $A, B \in M$ and $p, q \in \mathbb{Z}_d^*$ are nonzero. These operators commute exactly when the phase acquired on qudit 1 cancels the phase acquired on qudit 2. Equivalently, in symplectic-label language, their symplectic inner product vanishes. Because X^p and Z^q do not commute for $p, q \neq 0$, the first-qudit observables must fail to commute (so $A \neq B$) and the commutation condition fixes the ratio q/p. Counting choices gives

$$(d+1) \cdot (d-1) \cdot d = d^3 - d \tag{C.4}$$

entangled contexts.

C.1.3 Total number of maximal contexts

Adding both classes gives

$$(d+1)^2 + (d^3 - d) = d^3 + d^2 + d + 1, \tag{C.5}$$

which matches the standard symplectic-Grassmannian count of Lagrangian subspaces in $\mathbb{Z}_d^4$.

C.2 Coordinate Form of the Inconsistency Argument

Chapter 6 proves the contradiction in Claim 6.8 conceptually using the phase-space statement in Lemma 6.6. This section records the equivalent coordinate calculation (the original "bijection in i" argument).

Assume that a deterministic noncontextual assignment λ satisfies all clauses. By Lemma 6.4, its restriction to the first qudit is determined by $\lambda_1 := \lambda(X \otimes I)$ and $\lambda_2 := \lambda(Z \otimes I)$. Satisfying the $d+1$ nontrivial clauses $\phi_{C_A} \equiv [A \otimes I \neq r_A]$ means

$$\lambda(Z \otimes I) \neq r_Z \quad \text{and} \quad \lambda(XZ^i \otimes I) \neq r_{XZ^i} \quad \forall i \in \mathbb{Z}_d. \tag{C.6}$$

By linearity, these constraints are

$$\lambda_2 \neq r_Z \quad \text{and} \quad \lambda_1 + i\lambda_2 \neq r_{XZ^i} \quad \forall i \in \mathbb{Z}_d. \tag{C.7}$$

Under the hypothesis of Claim 6.8, the target vector r comes from a phase-space line, so writing r_X and r_Z for its X and Z components one has

$$r_{XZ^i} = r_X + ir_Z. \tag{C.8}$$

Substituting Eq. (C.8) into Eq. (C.7) and rearranging gives

$$\lambda_1 \neq r_X + i(r_Z - \lambda_2) \quad \forall i \in \mathbb{Z}_d. \tag{C.9}$$

But Eq. (C.7) implies $r_Z - \lambda_2 \neq 0$. Since d is prime, the map $i \mapsto r_X + i(r_Z - \lambda_2)$ is a bijection of $\mathbb{Z}_d$, so the right-hand side of Eq. (C.9) ranges over all values in $\mathbb{Z}_d$. No choice of λ_1 can avoid all of them, so Eq. (C.9) is impossible. This contradiction is precisely the coordinate form of Lemma 6.6.